Influence of Stratigraphy and Heterogeneity on Simulated Microwave Brightness Temperatures of Shallow Snowpacks

T P Watts

PhD

2015

Influence of Stratigraphy and Heterogeneity on Simulated Microwave Brightness Temperatures of Shallow Snowpacks

Thomas Peter Watts

A thesis submitted in partial fulfilment of the requirements of the University of Northumbria at Newcastle for the degree of Doctor of Philosophy

This research was undertaken in the Faculty of Engineering and Environment

November 2015

Abstract

Snow accumulation has potential climatological, hydrological and ecological impacts at a global scale. Satellite passive microwave radiometers have the potential to provide snow accumulation data with a historical record of over 30 years, however, current data products contain unknown uncertainty and error. Snowpack stratigraphy is the spatial variation in snowpack properties caused by the layered nature of the snowpack. Snowpack stratigraphy influences the accuracy and increases uncertainty in simulations of microwave emission from snow which in turn increases uncertainty in satellite derived estimates of snow water equivalent using microwave radiometers.

Two methods were developed to help better quantify snowpack stratigraphy. An improved technique for characterising snowpack stratigraphy within a snow trench was developed. Secondly a new method was developed to quantify the density of ice layers that form in snowpacks with known error and uncertainty.

Snowpack stratigraphy was characterised using the improved technique across the Trail Valley Creek watershed in the Canadian Northwest Territories. Two 50 m trenches and eleven 5 m trenches were dug across the range of landcover types found in the watershed. This dataset allowed layer boundary roughness to be characterised and the properties of snow layers to be mapped with an unprecedented level of accuracy.

Ice lens density was measured 60 times at three locations in the Arctic and mid-latitudes at locations with coincident ground based radiometer measurements. The impact that accurate parameterisation of density has on modelled estimates of brightness temperature was quantified.

Simulations of microwave brightness temperatures were conducted using snow emission models at all locations. The output of these simulations, and comparison to ground based observations where available, allowed for the characterisation of variability in brightness temperature simulations caused by stratigraphic heterogeneity. The findings presented in this thesis will inform research aiming to better characterise the satellite error budget. Improvements in this area helps improve global snow mass and snow accumulation estimates.

Contents

Abstract **i**

Contents **ii**

List of Figures **vi**

List of Tables **ix**

Acknowledgements **x**

Declaration of Authorship **xii**

1 Introduction **1**
1.1 Snow at a global scale 1
1.2 Measuring Snow Water Equivalent 5
1.3 Snowpack variability and stratigraphy 9
1.4 Quantifying variation in snowpack stratigraphy 11
1.5 Aims 11
1.6 Thesis structure 14

2 Origins of microwave signatures in tundra snowpacks **15**
2.1 In situ quantification methods of natural snow cover 15
2.1.1 Snow pit measurements 16
2.1.2 Measuring spatial variability 17
2.1.3 Emerging Methods 17
2.1.4 NIR Photography 18
2.2 General Principles of Passive microwave remote sensing 20
2.3 Snow emission modelling 22
2.4 Passive microwave remote sensing of snow 24

2.4.1 Principle 24
2.4.2 Retrieval Algorithms 25
2.4.2.1 Empirical 26
2.4.2.2 Modified Empirical 27
2.4.2.3 Model based 30
2.5 Challenges in the application of retrieval algorithms 31
2.5.1 Layering 32
2.5.2 Variability in Stratigraphy 33
2.5.3 Depth Hoar 35
2.5.4 Wind re-distribution 36
2.5.5 Melt and rain-on-snow events 36

3 Digitising Snowpack Stratigraphy with Improved Accuracy 39
3.1 Research aims and objectives 39
3.2 Development of stratigraphy digitisation method 42
3.2.1 Preparing the NIR images 43
3.2.2 Extracting snow stratigraphy information from NIR snow trench photography 44
3.2.3 Calculating positions in digital images in cm 46
3.2.4 Accounting for artefacts in digitised snow stratigraphy information 50
3.2.4.1 Applying smoothing 55
3.2.4.2 Smoothing Optimisation 55
3.2.5 Assigning snowpack properties to digitised stratigraphy 58
3.3 Field Methods 60
3.3.1 Field Site 60
3.4 Results 61
3.4.1 Variation in snowpack properties and characteristics 62
3.4.2 Variation in n-HUT model Tb 72
3.5 Discussion 78

4 Improved measurement of ice layer densities and application in snow microwave emission models 81
4.1 Aims 81
4.2 Measurements of ice layer density 82
4.2.1 Development of ice density measurement method 82
4.2.2 Methodological error 85
4.2.3 Field Measurements 87
4.2.3.1 Ice layer measurements 87

4.2.3.2 Brightness Temperature observations 89
4.3 Results: Ice layer measurements 89
4.3.1 Ice layer bubble size and thickness 89
4.3.2 Ice layer density 90
4.3.3 Error in measured density 91
4.4 Simulation of brightness temperatures using measured ice density 96
4.4.1 Model Initialisation 96
4.4.1.1 DMRT-ML 96
4.4.1.2 MEMLS 98
4.5 Results: Brightness temperature simulations 99
4.5.1 Model Sensitivity to ice layer properties 100
4.5.1.1 MEMLS 100
4.5.1.2 DMRT-ML 101
4.5.2 Model optimisation using ice layer density 103
4.5.3 Effect of ice layer density on polarisation and gradient ratios 105
4.6 Discussion and Conclusions 108

5 Snow Trenches in Inuvik 110
5.1 Introduction 110
5.2 Aims and Objectives 111
5.3 Field Methods 112
5.3.1 Field Site 112
5.3.2 Field Measurements 115
5.3.2.1 Application of NIR trenches to distances >50 m . 115
5.3.2.2 Trench measurements 116
5.4 Results and Analysis 119
5.4.1 Snowpack characteristics and variability 119
5.4.1.1 Snowpack variation over 50 m 119
5.4.2 Boundary Roughness Variability 123
5.4.3 Variation in simulated brightness temperatures 126
5.4.4 Sample size to accurately simulate brightness temperature 128
5.4.4.1 Differences between sites 133
5.5 Discussion 135
5.6 Summary 137
5.6.1 Quantify layer thickness and boundary roughness variability 138
5.6.2 Quantifying the impact of spatial variability of stratigraphy on Snow Microwave Emission Models 138
5.6.3 Determine what the minimum subset size is 139

6 Synopsis 140
6.1 Summary 140

6.1.1 Snowpack stratigraphy 141
6.1.2 Ice layer Density 144
6.2 Future Work 147

References **148**

List of Figures

1.1 Feedbacks in the Arctic 3
1.2 World population dependent on snow melt 4
1.3 Extreme runoff events in the Northern Hemisphere 4
1.4 Example SWE retrieval assimilation scheme 8

2.1 Plank's law 21
2.2 Effect of Grain Size on 37 GHz (V-pol) brightness temperature . . 27
2.3 Variation in penetration depth between different frequencies . . . 29

3.1 An example of NIR snow trench photography 43
3.2 NIR images stitched together to show stratigraphy across trench 44
3.3 Position of digitalized snow layers in pixels 45
3.4 Applying the canny edge detection algorithm to a measuring staff 47
3.5 Test layer translated using the per pixel translation 51
3.6 Un-smoothed snow layers quantified from NIR photography of snow trench wall, Red box indicates area displayed in Figure 3.7 52
3.7 Random roughness over the section highlighted in Figure 3.6, layers numbered in descending order according to height 53
3.8 Histogram of the random roughness metric for a sample snow layer 54
3.9 Random roughness over the section highlighted in Figure 3.6 after smoothing has been applied 56
3.10 Impact of smoothing on whole trench 57
3.11 Locations of density measurements placed automatically on snowpack stratigraphy 59
3.12 Locations where trench sampling took place 61
3.13 Difference in range of total snowpack SWE and Depth measurements across entire trench 63
3.14 Variation in snow properties within and between layers in each trench. 64
3.15 Snow microstructure and grain type symbols used in this thesis (classification/symbols from Fierz et al. (2009)) 65
3.16 Stratigraphy and snowpack properties of Trench 1, ice crusts are marked in red on the top image 66

3.17 Stratigraphy and snowpack properties of Trench 2, ice crusts are marked in red on the top image 67
3.18 Stratigraphy and snowpack properties of Trench 3, ice crusts are marked in red on the top image 68
3.19 Stratigraphy and snowpack properties of Trench 4, ice crusts are marked in red on the top image 69
3.20 Stratigraphy from trenches 1 and 2, showing how they relate to each other in three dimensions. 70
3.21 Boxplots for random roughness. 71
3.22 Histograms showing the distribution of Brightness Temperatures simulations for Trench 1 74
3.23 Histograms showing the distribution of Brightness Temperatures simulations for Trench 2 75
3.24 Histograms showing the distribution of Brightness Temperatures simulations for Trench 3 76
3.25 Histograms showing the distribution of Brightness Temperatures simulations for Trench 4 77

4.1 Ice layer density measurement flow chart 83
4.2 Ice volume measurement photographs 84
4.3 Ice layer density histogram 91
4.4 Schematic of ice layer layer porosity model 93
4.5 3d plot showing the influence of ice layer density 94
4.6 Observed and modelled snowpack at North Bay, explanation of snow symbols in figure 3.15 98
4.7 Sensitivity of MEMLS to ice layer properties 101
4.8 Sensitivity of DMRT-ML to ice layer properties 102
4.9 Difference between modelled and observed brightness temperatures with changing density for MEMLS 104
4.10 Difference between modelled and observed brightness temperatures with changing density for DMRT-ML 105
4.11 Effect of density on gradient ratio 107
4.12 Effect of density on polarisation ratio 107

5.1 Map of location of Trail Valley Creek 113
5.2 Meteorological data from the winter of 2012-2013 from the main tundra met site in Trail Valley Creek 114
5.3 Photo showing collection of snowpack data from Trench 4 in Trail Valley creek 116
5.4 Map of trench locations in Trail Valley Creek 118
5.5 Example of a spherical model fitted to the semivariogram data points 122
5.6 Semivariogram of snow layer thickness within trenches excavated in Trail Valley Creek 122

5.7 Layer boundary roughness compared to proportional layer boundary height 124
5.8 Layer boundary roughness compared to proportional layer boundary height with generalised fit 125
5.9 Comparison of trench data and distributed pit data 127
5.10 Semi-variograms of modelled brightness temperatures 128
5.11 Histograms of Brightness Temperature simulations of Trench 4 . . 129
5.12 Increasing the sample size and comparing the sample mean to the population mean for trench 4 132
5.13 Mean brightness temperatures at different sites around Trail Valley Creek 134

6.1 Flow chart of the key areas used in data assimilation schemes which are improved or addressed by the work in this thesis 141
6.2 Conceptual diagram of the areas improved by this research 145
6.3 Comparison of a typical brightness temperature distribution for 19 GHz H-pol when ice layers are a) absent and b) present 145

List of Tables

2.1 Passive Microwave satellite radiometer missions suitable for snow remote sensing . . . 22

3.1 Simulated brightness temperatures from using bulk snowpack properties . . . 72
3.2 Simulated brightness temperatures from using averaged snowpack based on trench data . . . 73
3.3 Mean and standard deviations of simulated brightness temperatures from trenches . . . 73
3.4 Differences in simulated brightness temperatures between pairs of orthogonal trenches . . . 74

4.1 Ice layer thicknesses and bubble sizes . . . 90
4.2 Ice layer density measurements, (all values have been corrected to account for the measured $-0.19cm^3$ bias in volume) . . . 90
4.3 Summary of range of input and initialisation parameters across all model runs . . . 97
4.4 Observed brightness temperatures . . . 103

5.1 Table of all measurements made at trenches their lengths and reference to locations in Figure 5.4 . . . 119
5.2 Range (cm) at sill for top middle and bottom layer thicknesses in each trench . . . 123
5.3 Coefficients for fitted boundary roughness relationships . . . 125
5.4 Range (lag distance) at sill of semivariograms . . . 127
5.5 Minimum sample size to achieve population mean for trench based brightness temperature simulations . . . 131
5.6 Comparison between the simulated brightness temperatures and required minimum sample size between different groups of sites . . . 134

Acknowledgements

Writing this thesis has proved to be a significant personal challenge, however, it would not have been possible without the support of a great many people. Thank you to all those who helped make my PhD a positive, exciting, interesting, at times even fun, experience. In particular I'd like to acknowledge:

The help and guidance of Nick Rutter and Melody Sandells, for their insight, encouragement and enthusiasm, whether things were going well or poorly. For sharing your ideas, helping me come up with my own and leading me to ask new questions when I was running out of steam.

Everyone I worked with at Environment Canada, Chris Derksen for seeing through the noise and knowing what matters...and then encouraging me to do that stuff! Thank you for your family's incredible hospitality, I will not forget the brisket in a hurry. Pete, Buffy (and Sheriff), thank you for letting me turn your empty apartment and basement into, (only marginally) less empty homes, and for your friendship and hospitality. Arvids, thanks for sorting everything out, and for passing on a tiny fraction of your field expertise... I know I've forgotten something!

The constructive criticism, feedback and helpful comments from my examiner Juha Lemmetyinen whose input has vastly improved the quality of this thesis. Also Ben Brock for his input during my viva and John Woodward for proof reading early versions of chapters of this thesis and for ongoing input and advice throughout my PhD.

The support of Richard Essery, Dave Thomas, Dave Halpin and everyone from Sherbrooke, Waterloo and Boise Universities who helped collect data and pass the time in the hut at trail valley creek.

My friends in Newcastle, for their endless distractions, - in many ways surfing is the perfect PhD sport. And from Chippenham and Sheffield, for providing excellent excuses to get out of the North East when things got a bit too Northern.

Finally, the support of my family, firstly the Stephensons for being my home in the North East. Edd and Jodie, thank you for always being there for me when disaster struck or when it didn't and for being the best brother and sister anyone could ask for. But most of all my parents for the lifelong support and for encouraging me to follow my passions, (despite the comparative lack of financial compensation). For your interest in my work and happiness and for motivating me to do more when times were good, and to 'just do something' when times were bad. Without any of you in my lives I would never have made it this far.

This work was supported by a Northumbria University RDF studentship and the Canadian Natural Science and Engineering Research Council; field activities were funded by Environment Canada.

Declaration of Authorship

I declare that the work contained in this thesis has not been submitted for any other award and that it is all my own work. I also confirm that this work fully acknowledges opinions, ideas and contributions from the work of others.

I declare that the Word Count of this Thesis is 31,374 words

Signed: 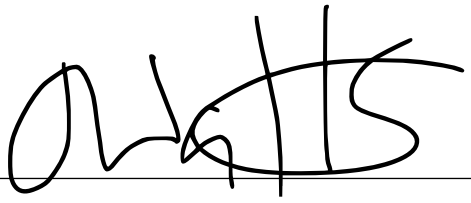

Date: 02.12.2015

Chapter 1

Introduction

1.1 Snow at a global scale

A warming climate affects, either directly or indirectly, all aspects of the earth's land surface (Turner and Overland, 2009). Positive ice and snow related feedbacks, such as the surface temperature feedback (as the surface warms, less energy is radiated back into space in the Arctic compared to low latitudes (Pithan and Mauritsen, 2014; Holland and Bitz, 2003)), and the snow/ice albedo feedback (warming causes less ice and snow cover which increases albedo and leads to further warming (Screen and Simmonds, 2010; Holland and Bitz, 2003)), change the local radiation balance at the poles. Ecological systems are also affected by changes in snow cover as part of a network of complex feedback loops, as shown in Figure 1.1 (Chapin et al., 2005). These feedbacks cause less outgoing radiation

from the earth (Moritz et al., 2002) and lead to a net increase in radiation which amplifies the effects of global warming at the poles (Crook et al., 2011). The effect this has on certain aspects of arctic environment is well established (Jeffries et al., 2014); sea ice shows a steady decline in extent (Serreze et al., 2007), permafrost extent is shrinking (Zhang, 2005), land based glaciers are retreating (Marzeion et al., 2014), the Greenland ice sheet is experiencing unprecedented melt (Nghiem et al., 2012) and spring snow extent is decreasing (Derksen and Brown, 2012). However, one crucial aspect is not well quantified; the impact that climate warming has had and will continue to have on the snow water equivalent (SWE) and the spatial distribution of seasonal snow (Robinson et al., 1993; Foster et al., 2005; Chang et al., 1997).

Seasonal snow is of particular importance to the $\frac{1}{6}$ of the worlds population who rely on snow melt for drinking water, agriculture, industry, manufacturing and recreation, as shown in Figure 1.2 (Barnett et al., 2005). Reliable estimates of snow water equivalent are required so we can better understand snow's role in the global earth surface system (Hancock et al., 2013), and improve inputs to hydrological models used to inform local authorities and resource management industries enabling them to plan usage and storage of water supplies (Stewart, 2009). The increased frequency in unpredicted droughts and extreme runoff events as shown in Figure 1.3 (Diffenbaugh et al., 2013) demonstrates the importance of being able to predict such events. Snow depth also plays an important role in global climatic feedbacks. Decreased snow depth causes less shrubs to be buried

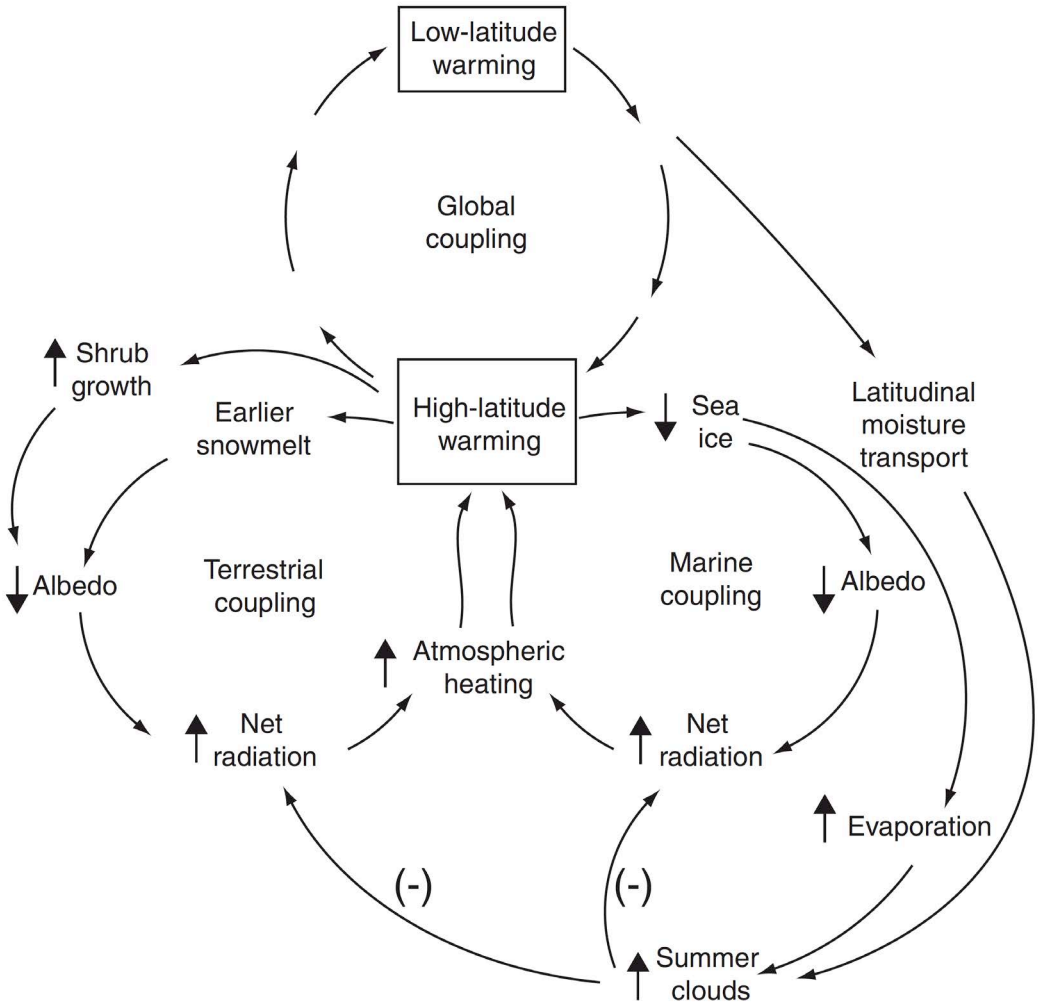

FIGURE 1.1: Diagram of feedback loops that couple climatic processes in arctic Alaska. Arrows linking processes indicate a positive effect of one process on another unless otherwise indicated (by minus signs) (Taken from Chapin et al. (2005)).

in the winter leading to decreased albedo and further warming, a process termed arctic greening (Loranty et al., 2014; Tape et al., 2006; Sturm et al., 2005; Jia et al., 2006).

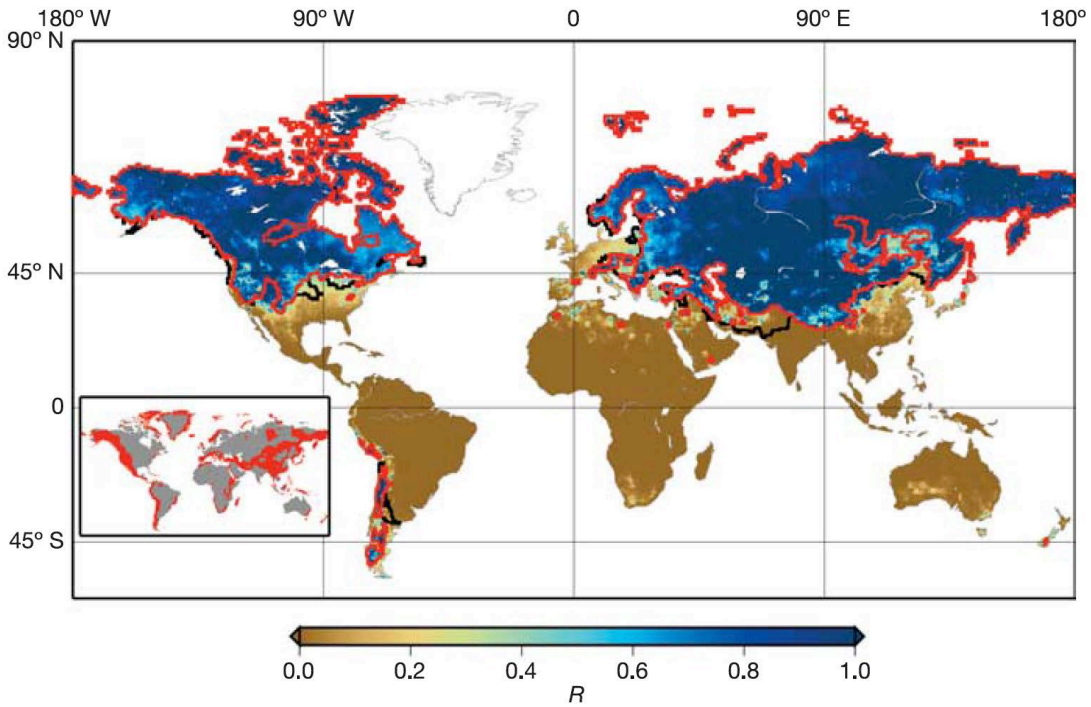

FIGURE 1.2: Accumulated annual snowfall divided by annual runoff over the global land regions. The value of this dimensionless ratio lies between 0 and 1 and is given by the colour scale, R. The red lines indicate the regions where streamflow is snowmelt-dominated, and where there is not adequate reservoir storage capacity to buffer shifts in the seasonal hydrograph. The black lines indicate additional areas where water availability is predominantly influenced by snowmelt generated upstream (but runoff generated within these areas is not snowmelt-dominated) (Taken from Barnett et al. (2005)).

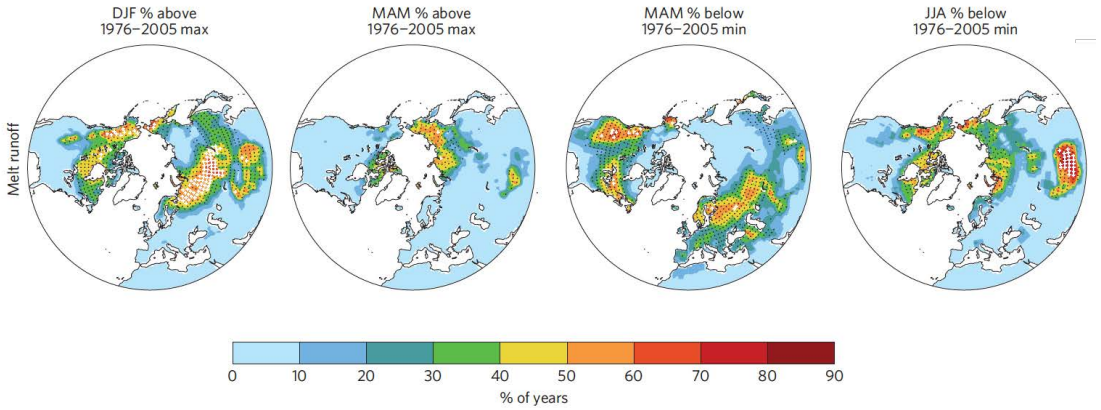

FIGURE 1.3: Occurrence of extreme runoff events in the Northern Hemisphere (adapted from Diffenbaugh et al. (2013)), for December, January, February (DJF), March, April May (MAM) and June, July August (JJA)

1.2 Measuring Snow Water Equivalent

Snow water equivalent is a function of snow depth and density (Gray and Male, 1981). In situ point measurements of SWE are usually taken using a snow tube. A snow tube extracts a vertical column of snow from the snowpack which is then weighed to calculate the SWE of the the snowpack at the given location. The snow tube allows the key information of depth and density to be recorded more quickly and in a less destructive manner than a snowpit (Church, 1933; Goodison et al., 1987; Woo, 1997) and when used as part of a transect provides information on the spatial variability of SWE.

While a global network of snow weather stations reporting snow depth exists, station locations are heavily weighted towards populated urban areas (Rees et al., 2013) and, as a result, are sparse in high latitudes (Brown et al., 2007). The large size, sparse population and inaccessibility of the Arctic means that alternative methods need to be used in this region. Model derived hemispheric estimates of SWE have made significant progress by using reanalysis data to drive snow and hydrological models and to determine snow accumulation (Troy et al., 2012; Liston and Hiemstra, 2011). Satellite remote sensing is the most practical mechanism with which to measure SWE on a hemispheric scale (Vander Jagt et al., 2013). Near infrared (NIR) and other visible band sensors can be employed to determine snow extent and other snowpack parameters such a grain size (Painter et al., 2009). However, visible band measurements have significant drawbacks as

they are not able to determine SWE directly and suffer from weaknesses such as requiring cloud free days and solar illumination, both of which are limitations to use in the Arctic. Passive microwave remote sensing (Staelin et al., 1977) which, although it has a course resolution of approximately 25 km (Kelly et al., 2003), does not require solar illumination, penetrates cloud cover and has a historical record of > 30 years (Dupont et al., 2012). The 19 - 37 GHz section of the spectrum is of particular interest for snow remote sensing. At these wavelengths a snowpack acts to attenuate the microwave emission upwelling from the ground and the level of attenuation is related to the depth and properties of the snowpack (Boyarskii and Tikhonov, 2000). The brightness temperature observed by the satellite radiometer is related to the emission from the earth (which is largely dependent on its physical temperature) and the attenuation of this emission by the snowpack (Ulaby et al., 1981).

Extensive work has been carried out to establish theoretical (Grody, 2008; Tse et al., 2007; Stogryn, 1986) and empirical (Chang et al., 1982; Foster, 1997; Kelly and Chang, 2003) links between attenuation in the snowpack, observed microwave brightness temperature and SWE. The classic, empirical approach (Chang et al., 1982) uses the simple retrieval algorithm

$$SD = 1.59 \times (T_{18H} - T_{37H})cm \tag{1.1}$$

to derive snow depth from brightness temperature, although this has proved to be unreliable over the Arctic and produced SWE products with large degrees of uncertainty (Koenig and Forster, 2004; Clifford, 2010).

The majority of the error and uncertainty in SWE products was attributed to factors such as the forest or lake fraction of the footprint, which are known to cause variation at the satellite scale (Derksen et al., 2003; Green et al., 2012). Work focused on quantifying the effect of these factors to improve SWE products, however, while forest and lake fraction can be observed relatively easily using existing satellite data products (Derksen, 2008), even when accounting for these factors uncertainty and error exists in the SWE data products (Foster et al., 2005). It has been hypothesised (Mätzler, 1994; Boyarskii and Tikhonov, 2000; Durand et al., 2008; Derksen et al., 2012a) that variation in the properties of the snowpack and/or our inability to correctly parameterise the variation in snowpack properties that occur within a satellite footprint using a simple retrieval algorithm, are the causes of the uncertainty. This has led to an increased interest in both, the physical properties of the snowpack, and how these properties physically attenuate the earth's microwave emission. Sophisticated data assimilation algorithms have been developed and implemented. Data assimilation organises the useful and less useful observations into physically consistent estimates of SWE. Ultimately data assimilation aims to produce the optimal combination of the measurements where the output (in this case SWE) lies within the error bars of all estimates, the assimilation estimates will be closer to the more accurate estimates. An

example of such an assimilation scheme which uses satellite observations, a land surface model and a radiative transfer model is shown in Figure 1.4 (Durand and Margulis, 2007). The approach of Takala et al. (2011) uses in situ measurements of snow depth in addition to satellite data and an iterative approach to estimate grain size using a snow emission model to produce a hemispheric product for SWE. Another approach which has demonstrated improvements in SWE retrievals is to use a snow model to estimate density and grain size in a coupled snow emission model (Langlois et al., 2012).

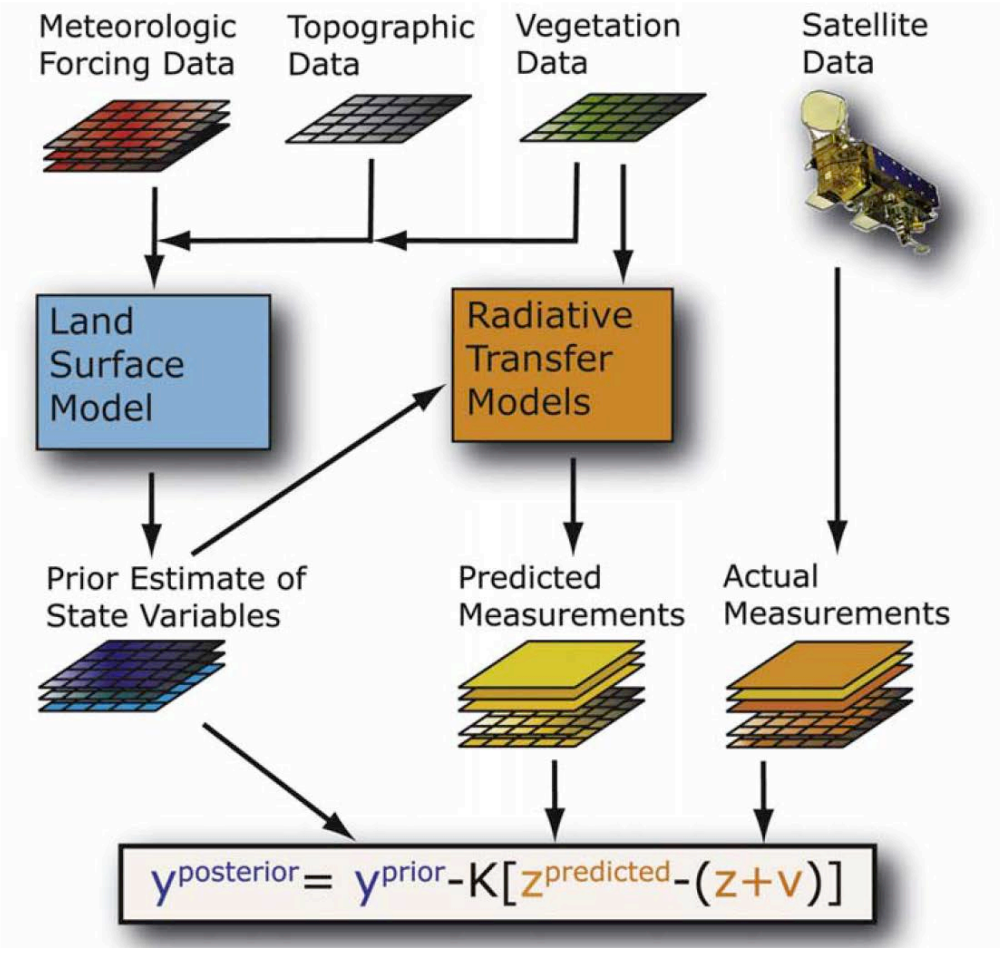

FIGURE 1.4: This schematic illustrates how the prior information, models, and synthetic measurements are merged using a data assimilation scheme as described in Durand and Margulis (2007)

1.3 Snowpack variability and stratigraphy

Snowpack stratigraphy describes the layered or stratified nature of snowpacks. Each layer in a snowpack is composed of snow with different properties to the layers above and below. The variation between snow layers is caused by the successive build up of a snowpack by depositional events, and the subsequent impact of in situ snow metamorphosis, melt, rain-on-snow events or wind compaction (Colbeck, 1991). Understanding variation in snowpack stratigraphy is crucial for understanding the microwave emission and radiative transfer properties of snow (Durand et al., 2008). Snowpack stratigraphy is highly variable at small spatial scales, although at large spatial scales major stratigraphic units are continuous (Sturm and Benson, 2004).

Changes in the properties of the snowpack are a key factor in the reflection and transmission of radiation in the snowpack (Ulaby et al., 1981). Variation in snowpack stratigraphy is one of the key drivers of variation in modelled and observed microwave brightness temperatures (Derksen et al., 2012a; Durand et al., 2008), at scales ranging from the footprint of a ground based radiometer (plot scale) (Rutter et al., 2014) to the resolution of a satellite derived data product (Derksen et al., 2012a). Current passive microwave derived SWE products do not account for spatial variations in snowpack stratigraphy as the ability of the products to account for snowpack stratigraphy is limited by a lack of field

observations. Existing studies that have tried to characterise sub-footprint variability have focused on either, snow pits taken at a variety of locations within a satellite footprint (Derksen and Brown, 2012; Elder et al., 2009), or long transects (Sturm and Benson, 2004). Despite the fact that it is known that variation in stratigraphy at the sub-footprint to 1 km scale introduces error into estimates of SWE from brightness temperature measurements (Rutter et al., 2014; Derksen et al., 2014), it is known that this error does not completely mask the signal relating brightness temperature to SWE (Vander Jagt et al., 2013; Li et al., 2012; Derksen et al., 2014). By focusing on the impact of simplifying the stratigraphy of a given snowpack, it has been found that, at a point, simplification from five to one layers reduces computational requirements and does not increase error in simulated brightness temperatures (Huang et al., 2012). However when applied to field variability, results are more mixed (Rutter et al., 2014; Derksen et al., 2012a). In addition to this, relatively little has been published looking at small scale variation in stratigraphy (Rutter et al., 2014; Tape et al., 2010; Derksen, 2008; Pielmeier and Schneebeli, 2003; Sturm and Benson, 2004) and ultimately the question of whether the variation exhibited at the plot scale can influence brightness temperatures at the satellite scale is as yet unanswered.

1.4 Quantifying variation in snowpack stratigraphy

Quantifying vertical variation in stratigraphy in a snow pit gives the observer one profile for that snowpack. Past work has focused on distributing multiple snow pits around different snow cover types to try to quantify lateral variability within a satellite footprint (Derksen and Brown, 2012; Derksen et al., 2014). Other work has utilised a snow trench to quantify stratigraphic variation at cm resolution over short distances of around 5 m (Rutter et al., 2014; Tape et al., 2010). The technological development that has enabled this scale of work to be conducted in situ in a timely manner, is the availability of compact or SLR cameras adapted to take photos in the near infra-red (NIR) (850 nm) part of the electromagnetic spectrum. At this wavelength the camera is sensitive to changes in the microstructure of the snow, and it is possible to use the images to quantify variability in snowpack stratigraphy over the distance of an excavated snow trench (Tape et al., 2010; Rutter et al., 2014).

1.5 Aims

The overall goal of this thesis is to improve knowledge of how snowpack stratigraphy influences the precision and accuracy of snow microwave emission models in Arctic tundra environments. This will be achieved by addressing two key

weaknesses in our current implementation and parameterisation of snowpack stratigraphy in snow emission models:

1. The presence of ice lenses and layers in a snowpack substantially increases bias in horizontally polarised simulated brightness temperatures (Rees et al., 2010; Durand et al., 2008; Derksen et al., 2012a).

2. The influence of spatial variation of snowpack stratigraphy on brightness temperature signatures is not well characterised(Derksen et al., 2014).

To help address these weaknesses three aims and associated objectives have been created

Aim 1: To develop a method that will enable accurate quantification of spatial variability in snowpack stratigraphy over increased spatial scales on tundra landcover. To achieve this aim three objectives were identified:

(a) To increase efficiency with which NIR photography of snowpack stratigraphy can be collected in the field, and optimise the post-processing digitisation

(b) to improve accuracy of digitised snow stratigraphy to a consistent 1 cm accuracy across a 5 m snow trench for use in all environments

(c) To Quantify internal snow layer boundary roughness

Aim 2: To improve the parameterisation of ice layers in snow emission models by measuring and analysing the influence of their structural properties (such as density and bubble size) on the accuracy of simulated brightness temperatures

(a) To develop a new field method for measuring the density of ice layers

(b) To compare simulated and observed brightness temperatures using measured ice layer densities to test the sensitivity of the Microwave Emission Model for Layered Snowpacks (MEMLS) and Multi-layer Dense Media Radiative Transfer (DMRT-ML) snow emission models to changes in ice layer parameterisation

(c) To examine the impact that any sensitivity could have on ice layer detection algorithms

Aim 3: To quantify the variation in stratigraphy within an Arctic watershed, fully capturing variation in the position of layers and the layer properties.

(a) To quantify layer thickness and boundary roughness variability

(b) To quantify the impact of spatial variability of stratigraphy on Snow Microwave Emission Models

(c) To determine the minimum subset size in each trench location required to achieve the mean brightness temperature for that trench

1.6 Thesis structure

This thesis will be structured in six chapters, this, the first chapter, serves as the main introduction, to outline the main motivations, and questions addressed in this thesis. The second chapter will provide the background to the thesis in more detail, and provide the context on where this work sits in the current state of science.

Following these there are three main results and method chapters:

- Chapter 3 introduces the main method of quantifying snowpack stratigraphy using NIR photography. This method is then used to investigate plot scale, layer boundary roughness, and intra-layer heterogeneity for two sites in the sub arctic.
- Chapter 4 will address the parameterisation of ice layers, and introduce a specific method which was implemented to carry out this work.
- Chapter 5 will use the methods outlined in chapter 3, but on a larger scale, to investigate variation in snowpack stratigraphy and simulations from emission models over different landcover types in an Arctic drainage basin.

The final chapter, chapter 6, acts as a synopsis to summarise and discuss the overall findings of the thesis and outline future work.

Chapter 2

Origins of microwave signatures in tundra snowpacks

2.1 In situ quantification methods of natural snow cover

Snow pack stratigraphy provides important information about the properties, processes and dynamics of a snowpack, it has numerous uses in snow hydrology, avalanche prediction and, as explored in more detail in this Chapter, snow remote sensing. In situ measurements of snowpack stratigraphy are typically made by opening up a snow pit face and recording information as a profile down the wall of the pit, although as will be discussed in section 2.1.3 some newer technologies provide alternatives.

2.1.1 Snow pit measurements

The first measurement made in a snow pit is the overall depth of the snowpack and then its layered structure, typically a vertical resolution of 1 cm is used to achieve this. Textural information about the snowpack is recorded, including its hardness. This one dimensional method of recording snow pack stratigraphy makes the assumption of discrete boundaries between layers, and that snow layers are parallel (Pielmeier and Schneebeli, 2003). Snow temperature is typically recorded at set intervals through the snowpack.

Snow density is the bulk snow mass per unit volume. Classically it is measured by weighing a snow sample of known volume. A snow sample of known volume is extracted from the snow pit face using a wedge or square snow density cutter. Measurements are made either as a continuous profile down the pit face, at set intervals or using one sample per identified layer. It is also possible to measure density using the snow's dielectric properties (Mätzler, 1996).

Snow grain type changes as the snow is metamorphosed on the ground. Grain shape is classified in Fierz et al. (2009). The type (or types) of crystals in a layer are identified in the field using a magnifying glass or field microscope and a crystal card. Grain size is measured in the same manner, grain size is the most common metric used to quantify snow microstructure although newer less subjective methods are emerging, as discussed in Section 2.1.3.

2.1.2 Measuring spatial variability

Snow variability has historically been recorded using a snow course (Gray and Male, 1981). A snow course consists of a well defined path or track that is routinely sampled along over a period of time. The snow course aims to cover as many different land cover and topography types as possible within the practical limitations of a single survey. Snow pits and dug, and bulk density measurements and snow depth measurements are taken along the snow course. Snow courses allow spatial (and with repeat sampling, temporal) snowpack variability to be measured although they do not provide continuous snow stratigraphy information as some emerging technologies can (Section 2.1.3).

2.1.3 Emerging Methods

Emerging methods and technologies are providing new methods with which to measure snow pack stratigraphy at a single profile, these improve methods of measuring the specific surface area (SSA) of snow. SSA is physically important as it directly relates the the way in which snow interacts with optical radiation and is therefore a good way to quantify snow microstructure. Several methods exist for measuring SSA including using the reflectance from a 1310 nm laser (Gallet et al., 2009) and near infra-red photography (described in more detail in section 2.1.4). Additionally it is also possible to measure the microstructure of snow directly by utilising a microCT scanner (Heggli et al., 2009).

2.1.4 NIR Photography

The NIR part of the spectrum is sensitive to changes in the SSA of snow (Matzl and Schneebeli, 2006). Using this physical property NIR photography has been utilised to capture the structure of a snowpack in the field. Tape et al. (2010) developed a method to identify and quantify snowpack stratigraphy using near infra-red (NIR) photography. A Fuji S9100 digital camera was adapted to be sensitive to light with mid-point wavelength of 850nm and by photographing the side of a snow trench at 50cm horizontal intervals, the stratigraphy of the snowpack became more apparent and could be quantified digitally from the photographs (Matzl and Schneebeli, 2006). It is possible to use the images to quantify variability in snowpack stratigraphy over the length of the trench (Rutter et al., 2014).

Using NIR photography along a trench provides considerable advantages and speed increases over recording stratigraphy with manual inspection in the field (Tape et al., 2010). However, there are two major weaknesses with this technique. Firstly, the processing time required to extract digitised stratigraphy from the images can be extensive. Using previous methodologies and protocols one 5 m trench could take up to a day. Secondly, variation in the focal length of the camera causes changes in scale along the trench which introduces error. In Tape et al. (2010) trenches were excavated on a frozen lake, this helped minimise uncertainty in this area allowing for the method to be developed in a somewhat

idealised environment with very little topographic variation. When the method is applied to environments with more varied subnivean topography the uncertainty between the digitised snow layers and geo-referenced trench position increases, and a more rigorous method for translating a point location is required. This makes assigning measurements taken in the field to a specific snow layer difficult. Past work has approached the problem by utilising a strict protocol to, while not eliminate, hopefully constrain uncertainty (Rutter et al., 2014). In this work, overall average values were applied to each layer in the snowpack, so any variation in snow properties that occurred within a layer, in the scale of the trench, was not accounted for, characterised or quantified.

NIR photography of a snow trench provides high resolution surface and layer boundary roughness (the roughness between the snow layers within a snowpack) information. Surface roughness is a control on the transfer of wind energy, and affects snow transport, redistribution and latent and sensible heat exchanges (Fassnacht et al., 2009b). Information at a resolution high enough to constrain layer boundary roughness cannot be obtained from in situ field measurements alone, as the time required is too great. In the past, surface roughness has been characterised over small distances and over larger scales (Fassnacht et al., 2009a) although roughness between snow layers has never to my knowledge been measured or characterised. Theoretically layer boundary roughness has a large impact on radar backscatter (Marshall and Koh, 2008), although it has never been quantified at the plot scale.

2.2 General Principles of Passive microwave remote sensing

Kirchhoff's law of thermal radiation (1860) states that when an object is at thermal equilibrium (neither warming nor cooling) then the power radiated by the object must be equal to the power absorbed. An object that absorbs and reradiates 100% of the radiation incident upon it is described as a blackbody, an object that absorbs (and therefore reradiates) less than 100% is described as a grey body. The spectral radiance of a blackbody (B) at a particular frequency (v) is dependent only on the blackbody's physical temperature, and can be calculated using the Plank Radiation Law as shown in Equation 2.1 and Figure 2.1 where k_B is the Boltzmann constant, h is the Plank constant, and c is the speed of light.

$$B(v,T) = \frac{2hv^3}{c^2}\frac{1}{e^{\frac{hv}{k_BT}} - 1} \tag{2.1}$$

Emissivity, ϵ, is a measure of the efficiency with which a surface emits thermal energy. It is the brightness of a grey body relative to a black body of the same temperature (for a blackbody $\epsilon = 1$) (Ulaby et al., 1981). Brightness temperature is the quantity measured by a radiometer and describes the intensity of radiation emitted by an object or area under observation. Brightness temperature depends

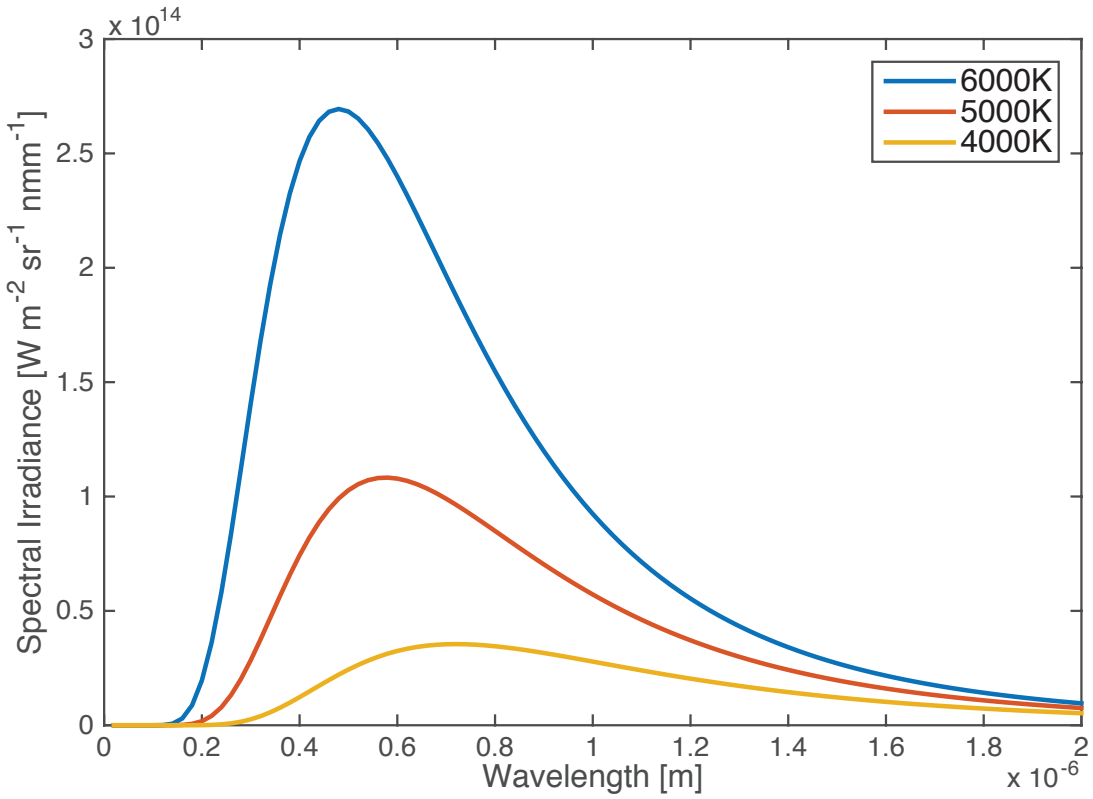

FIGURE 2.1: Plank's law describes how spectral reflectance varies with physical temperature and frequency

on the temperature and emissivity of the object (Ulaby et al., 1981), it is related to emissivity using

$$\epsilon = \frac{Tb}{T}. \tag{2.2}$$

Radiometers can be mounted onto satellites to measure the brightness temperature of the earth's surface and atmosphere, and they are most commonly used for meteorological or oceanographic remote-sensing. Radiometers that operate

at frequencies suitable for snow remote sensing and are currently in orbit (both working and non-working) are listed in Table 2.1.

Table 2.1: Passive Microwave satellite radiometer missions suitable for snow remote sensing

Instrument	Mission	Availability
SMMR	Nimbus	1978-1987
SSM/I	DMSP	1987-
SSMIS	DMSP	2003-
AMSR	ADEOS-II	2002-
AMSR-E	EOS Aqua	2002-2011
AMSR2	GCOM-W	2012-
PRIRODA	MIR	1996-2001

2.3 Snow emission modelling

The ability to simulate snow microwave emission is useful both for use in data assimilation and SWE retrieval schemes, and to better enable us to understand the radiative properties and processes of snow and ice. The simulation of microwave brightness temperatures of a snowpack is approached in two parts. Firstly the electromagetic properties (effective dielectric constant, scattering and absorption coefficients) that characterise the interaction between the wave and snow are calculated from the microstructural properties of the snow. Secondly the emission and propagation through the snowpack are calculated by accounting for the interactions within the snow as well as the refraction, reflection and transmission that occur at interfaces between snow layers or between the snow and the air/ground.

Several models exist to solve these problems. In this thesis, n-HUT (Lemmetyinen et al., 2010), MEMLS (Wiesmann and Mätzler, 1999) and DMRT-ML (Picard et al., 2013) are used. Tedesco and Kim (2006) compared simulations from a large number of snowtypes and demonstrated that no particular model systematically reproduces all of the experimental data. They were unable to attribute their discrepancies to any root cause, so it is not known if problems are attributable to the fundamental electromagnetic theory, specific details of the models, or if there was uncertainty in the evaluation data, and the methods used to represent snow grain size. Snow emission models are currently not able to accurately and consistently reproduce observed Tb values without using additional scaling factors and coefficients to tune model output (Derksen et al., 2012a; Langlois et al., 2012; Rutter et al., 2014). Three areas have been identified as the primary source of bias in simulations: the quantification and parameterisation of observed snow microstructure in model input (Langlois et al., 2010); uncertainty in the simulation of emission from the ground and soil under the snowpack (Roy et al., 2013); and the inability of models to take full account of snowpack stratigraphy including the presence of ice layers (Durand et al., 2011).

2.4 Passive microwave remote sensing of snow

2.4.1 Principle

For a snow covered land surface, the brightness temperature observed by a space borne radiometer is affected by:

1. Soil
    - Physical temperature
    - Soil dielectric profile
    - Surface roughness
    - Textural composition
    - Volume scattering within the soil
2. Vegetation
    - Absorption and emission determined by physical temperature, moisture and physical characteristics of the plants
    - Volume scattering within the vegetation, and surface scattering at vegetation interfaces, determined by physical structure of plants
3. Atmosphere
    - Weather conditions effect the scattering and absorption in the atmosphere

- Cosmic microwave background emission

4. Snowcover

    - Scattering properties of snow cover, determined by snow microstructure
    - Absorption and emission of snow, determined by snow density, temperature and wetness of the snowpack
    - Total mass of snow in the propagation path of microwaves, given by the snow water equivalent

There is a theoretical relationship between the SWE of a snowpack and its observed brightness temperature. Defining this relationship is complicated by the fact that the emission from and attenuation by the snowpack depend on many factors in addition to SWE

2.4.2 Retrieval Algorithms

Passive microwave data is of particular use for the creation of global snow products as it has a large spatial extent, frequent revisit times (up to twice daily) and relatively long term temporal continually (Tait, 1998). For this reason, a great deal of research has focused on developing and improving methods of retrieving SWE from passive microwave brightness temperatures (Chang et al., 1981; Foster et al., 1980; Goodison and Walker, 1995; Pulliainen and Hallikainen, 2001; Tait,

1998; Hallikainen and Jolma, 1992; Grody and Basist, 1996). The following sections will describe the different types of algorithm and approach that have been taken to solve this problem, starting from simple empirical algorithms, to modified, landscape-specific empirical algorithms, and then finally model based approaches.

2.4.2.1 Empirical

The classic approach for the calculating SWE using passive microwave brightness temperature compares the brightness temperature of a frequency expected to be readily scattered and absorbed by the snow cover and the brightness temperature of a frequency that will not experience so much scattering. An empirical relationship can be established between the differences in brightness temperature of the two frequencies and the SWE of the snowpack. Foster et al. (1980) identified 37 GHz as a frequency which is sensitive to the snowpack and 19 GHz as having a wavelength long enough to not be affected by the snow cover but rather the underlying soil. Figure 2.2 shows the effect of grain size on 37 GHz (vertically polarised) brightness temperature. As grain size approaches the wavelength of a specific frequency, scattering at that frequency will increase. Brightness temperatures for 37 GHz are therefore affected by snow microstructure and grainsize in addition to snow water equivalent.

The first hemispheric algorithm to describe such a relationship was the Chang algorithm (Chang et al., 1987), shown in Equation 2.3 where SD is snow depth.

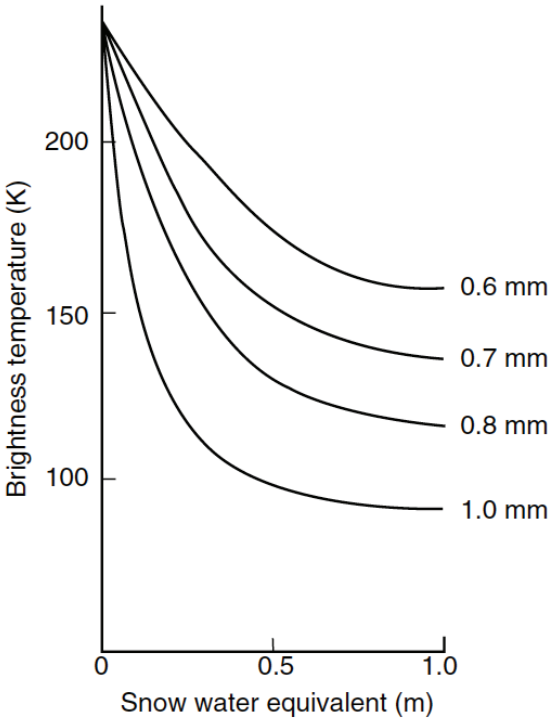

FIGURE 2.2: Effect of Grain Size on 37 GHz, vertical polarisation brightness temperature (Adapted from Rees (2006) redrawn from data presented in Armstrong et al. (1993) and Chang et al. (1981)

By assuming a snow density of 300 kg m^{-3} this algorithm was used to calculate SWE at a hemispheric scale.

$$SD = 1.59 \times (T_{18H} - T_{37H})cm \tag{2.3}$$

2.4.2.2 Modified Empirical

At a global scale problems arise where, within one satellite footprint, multiple landcover types need to be integrated across in order to provide continuous and standardised spatial coverage. In order to address these problems, successive

retrieval algorithms have worked to subset landcover types and incorporate additional parameters specific to them. The Meteorological Service of Canada (MSC) (now part of Environment Canada (EC)) developed algorithms for a wide range of Canadian landcover types, all based around the form

$$SD = a - b \times (T_{37V} - T_{18V}) \tag{2.4}$$

where SWE is snow water equivalent in mm and a and b are empirical parameters. For example Walker and Silis (2002) assign $a = -20.7, b = 2.59$ for use in the lake scattered tundra of the Mackenzie River basin. These and other similar algorithms have been used operationally since 1988 and have been shown to be accurate to $\pm 10 - 20$ mm SWE (Derksen et al., 2002; Goodison and Walker, 1995). A similar approach has been used on SMMR data which has allowed for a longer time series to be created (Derksen et al., 2003).

When a snowpack reaches a certain depth, the saturation of microwave radiation occurs (Sturm et al., 1993), this is when all of the emission from the earth is absorbed by the snowpack (Kelly et al., 2003). The depth of snow where saturation occurs is different for every frequency (Durand and Margulis, 2006). The depth that radiation is able to penetrate into the snowpack is called the penetration depth. The penetration depth changes with frequency and grainsize as is shown in Figure 2.3. The shorter penetration depth of higher frequencies

has the potential to be useful as it allows information to be gained about specific parts of the snowpack, for instance, 37 GHz has a penetration of around 35 cm, this provides a penetration depth similar to the depth of a tundra snowpack and so, changes in shallow snowpacks are particularly detectable at 37 GHz. For a frequency around 89 GHz only the surface of the snow at the snow-air interface impacts the signal, so changes in this part are of particular importance to brightness temperature changes at this frequency.

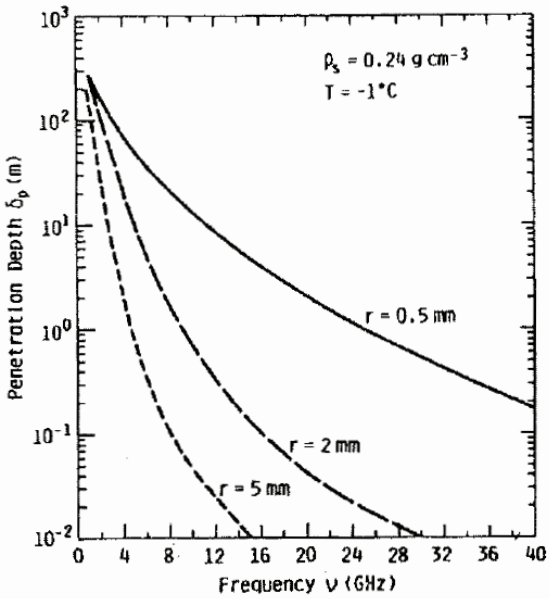

FIGURE 2.3: Variation in penetration depth between different frequencies (Adapted from Ulaby et al. (1986))

in addition to the MSC, Tait (1998) produced a SWE product by dividing the northern hemisphere into different vegetation and open landcover types, however, confidence in the results were low, with depth hoar development (discussed more in 2.5.3), high wind distribution (discussed in section 2.5.4) and boreal forest proved problematic for the algorithms.

2.4.2.3 Model based

While using different algorithms for different land cover types goes some way towards addressing the issue of spatial heterogeneity between landcover types, it does not begin to address issue of to how the snowpack changes temporally. More recently work has looked to develop algorithms based on those of Chang et al. (1987) that also account for seasonal evolution (Kelly and Chang, 2003), snow metamorphism (see also section 2.5.3) (Josberger and Mognard, 2002) and topography (Kelly et al., 2003).

The HUT model inversion method used by Pulliainen and Hallikainen (2001) iterates the HUT snow microwave emission model to minimise the difference between modelled and observed brightness temperatures. This is achieved by optimising the values for SWE and grain size. The algorithm also accounts for forest fraction in a satellite footprint.

As there are inherent weaknesses with all remote sensing, modelled and observed SWE data products, current work is highly focused on using a combination of multiple methods for deriving SWE in a data assimilation scheme (Takala et al., 2011; Durand et al., 2011). A data assimilation algorithm takes the estimated values from several sources, and by combining them, and accounting for their errors (assuming error and uncertainty are known) a more accurate value can be calculated. There are many different methods which can be utilised within the field of data assimilation involving the implementation of a variety of different cost

functions and algorithms. Generally a mixture of remote sensing and modelled data is used in order to provide the full scope of possible values (Reichle, 2008). For SWE data assimilation schemes snow emission models are a key component, as they provide a modelled value for remotely sensing brightness temperatures and can be iterated in certain schemes to calculate parameters which are required in other models or data products.

2.5 Challenges in the application of retrieval algorithms

Despite the wide range of research which has been carried out into the use of conventional retrieval algorithms to derive SWE, it is widely accepted that no consistently accurate SWE or snow depth product has resulted. In tundra snowpacks, conventional retrieval algorithms result in a consistent underestimation of SWE compared to in situ ground measurements (Grippa et al., 2004; Armstrong and Brodzik, 2002). The reason for the uncertainty can be attributed to an inability of these algorithms to account for heterogeneity in the snowpack and snowpack properties within a satellite footprint (Derksen et al., 2012a). This section will now review the causes of the heterogeneity and the impact that has been attributed to each aspect.

2.5.1 Layering

In the Arctic, seasonal snow layers form within the snowpack. Sturm et al. (1995) stated that a typical tundra snowpack consists of 6 layers, the least of any snow cover class with the exception of very thin ephemeral and prairie snow cover. A typical Arctic or sub-arctic snowpack is composed of a depth hoar layer at the base of the snowpack. Over that are several high density wind slab layers and then a top layer of freshly deposited (either by wind or precipitation) snow (Derksen et al., 2014). The structure of the snowpack has been identified as an important component in determining the brightness temperature of a snowpack. Snowpack structure has been recognised as being particularly difficult to interpret and quantify in the spectral signature of snow cover (Bernier, 1987).

When characterising stratigraphy a tundra snowpack can generally be simplified into three main snow types (Sturm et al., 1993). The bottom of the snowpack is composed of large grained depth hoar, the volume of depth hoar is of particular importance for passive microwave remote sensing (Foster et al., 1999; Foster et al., 2000). The second type is composed of higher density smaller grain size wind slab layers. These layers, formed by the successive wind re-distribution and overlaying of precipitated snow (Derksen et al., 2014) can also include indurated depth hoar (Sturm et al., 1993), where depth hoar faceting has developed within the wind slab. The hardnesses will vary between layers, however, due to the similar wind based method of compaction the grain diameter is often similar and small.

The top layer is composed of fresh, recently precipitated snow and generally comparatively thin compared to the other two layers. This layer is thin because of the wind redistribution of snow in tundra environments, in forest or shrub dominated landscapes, where wind speed is lower, this top layer is likely to be thicker.

2.5.2 Variability in Stratigraphy

Our ability to quantify variability in snowpack stratigraphy is limited by a lack of field measurement. The reasoning for this is that measuring and recording snowpack stratigraphy information requires specific skills and can be laborious and time consuming (Sturm and Benson, 2004). A snow pit provides only one snow profile at one location and so generating statistically significant distributions of snowpack variability is challenging. The majority of existing studies focus on either snow pits taken at a variety of locations within a satellite footprint (Derksen and Brown, 2012; Elder et al., 2009) or along transects at scales ranging from hundreds of metres to thousands of km (Sturm and Benson, 2004) in order to try to capture the variability within one, or multiple landcover types. Despite the fact that variation in snowpack stratigraphy at the plot scale introduces error into estimates of SWE from brightness temperature measurements (Rutter et al., 2014), at larger scales there is still a significant relationship between brightness temperature to SWE and (Vander Jagt et al., 2013; Li et al., 2012). Work has focused on the impact of simplifying the stratigraphy of a given snowpack, and

has found that some simplification reduces computational requirements and does not increase error in simulated brightness temperatures (Huang et al., 2012). However, these studies have only been based on a small number of profiles of snowpack stratigraphy distributed over a surface. While they exhibit a large and concerted effort to cover different land cover and terrain types, there are still questions over whether a network of snow pits can capture the range of snowpack stratigraphy, and there is a gap in the literature examining whether a single snowpack profile obtained from a snow pit can characterise the snowcover for one landcover type.

Snow layers vary in thickness at different scales (Sturm and Benson, 2004) but additionally, smaller scale roughness between the boundaries of the snow layers can be characterised using roughness metrics (Fassnacht et al., 2009b; Anttila et al., 2014), although these have previously only been applied to snow surface and ground roughness. Currently, snow emission models simulate brightness temperature in one dimension. However, as the science progresses so that two dimensions are used, a roughness will need to be applied to the layer boundaries. Currently, the internal roughness of layer boundaries is not known. An additional use of this layer boundary roughness information is its application in nadir FMCW sensors, where the layer boundary roughness contributes greatly to the attenuation of the snowpack (Marshall and Koh, 2008).

2.5.3 Depth Hoar

Volume scattering within the snowpack is directly influenced by the grain size of the snow crystals in the snowpack. It is therefore an extremely important and sensitive parameter in passive microwave snow remote sensing (Hall et al., 1986). When depth hoar is present in the snowpack the grain size can approach or exceed the wavelength being measured, this causes the lower than expected brightness temperature values(Hall et al., 1986). The effect of this increased scattering is so pronounced that, once a depth of just 30cm of depth hoar is reached, all of the radiation emitted by the earth at 37 GHz is scattered and the brightness temperature is composed of the emission from the mass of the snowpack alone (Sturm et al., 1993). In addition to the grain size, the shape of the crystals also has an impact (Foster et al., 2000; Foster et al., 1999). As the depth hoar grows in the snowpack brightness temperatures will drop due to increased scatter. However, SWE may well remain the same. Accounting for this is a key consideration in the use of retrieval algorithms for tundra snow. However, work by Koenig and Forster (2004) showed that it is possible to achieve consistently accurate SWE estimates in depth hoar dominated snow as long as the data is temporally and spatially averaged over multiple footprints.

2.5.4 Wind re-distribution

Snow cover is precipitated and then redistributed by the action of wind transport. Large scale wind transport does occur and is controlled mainly by large climatic and geographic features such as lake effects, mountain ranges etc. (Pomeroy and Gray, 1995). While this is important for global and hemispheric modelling applications it is not necessary to account for this in passive microwave remote sensing as it occurs at a much larger scale than the spatial resolution of the satellite sensors.

The aspect of wind distribution which is most important when addressing weaknesses in passive microwave remote sensing is the redistribution effects that occur at a spatial scale within one land cover - specifically within one satellite pixel (< 25 km). It is not currently known exactly what impact small scale changes in snowpack stratigraphy (the most immediate impact of wind re-distributed snow) has on satellite scale brightness temperatures. This question can be considered a sub-question of the larger pressing question of the impact of snowpack heterogeneity within a satellite footprint, one which is starting to be addressed (Derksen et al., 2012a).

2.5.5 Melt and rain-on-snow events

Ice structures form in snowpacks during melt or rain-on-snow events (Colbeck, 1991), when rain either freezes on contact with the surface of the snowpack or

water refreezes within the snowpack to form ice layers, ice columns, or basal ice layers (Gray and Male, 1981). Strong intercrystalline bonds, created from refreezing of liquid water, lead to the formation of cohesive ice structures (Fierz et al., 2009). The presence of ice layers changes the thermal and vapour transport properties of the snowpack (Putkonen and Roe, 2003). Permeability of ice layers to liquid water and gas is vastly reduced compared to snow(Albert and Perron Jr, 2000; Colbeck and Anderson, 1982; Keegan et al., 2014). Impermeable layers are identifiable because pores do not connect within the ice formation and the granular snowpack structure is missing (Fierz et al., 2009). Ice layers differ from ice crusts and lenses; ice crusts are always permeable and have a coarse grained granular snow-like structure (Colbeck and Anderson, 1982). Ice lenses are similar to ice layers in that they can be impermeable and do not have a granular structure, but ice lenses are discontinuous ice bodies that cover much smaller spatial scales than ice layers (Fierz et al., 2009).

Ice layers (the focus of Chapter 4) introduce uncertainty into the performance of microwave snow emission models when simulating horizontal polarisations (Rees et al., 2010). Snow emission models are an important component of satellite derived snow water equivalent (SWE) retrieval algorithms, and existing algorithms favour using vertically polarised brightness temperatures over horizontal primarily to avoid the issues with ice layers (Takala et al., 2011). The radiometric influence of thin ice layers poses a significant challenge for physical and semi-empirical emission models, which have either focused on modelling ice crusts as

coarse grained snow (Matzler and Wiesmann, 1999) or as planar (flat, smooth and solid) ice layers (Lemmetyinen et al., 2010). The structure and properties of ice layers remain poorly quantified with field observations (Montpetit et al., 2012), which further hinders model development and evaluation. Improving snow emission models to include more realistic simulations of ice layers by accounting for ice layer density should improve model estimates of brightness temperatures (Durand et al., 2008; Montpetit et al., 2012; Rutter et al., 2014).

Field measurements of ice lens, crust and layer densities exist, however, they vary drastically and a quantitative assessment of the error in measurement techniques is absent. Ice crust density measurements taken in the Canadian Arctic by submerging pieces of ice crust into oil resulted in a range of densities from 630 to 950 kg m^{-3} (Marsh, 1984) and ice layer densities of 400 to 800 kg m^{-3} were measured in seasonal snow on the Greenland ice sheet (Pfeffer and Humphrey, 1996). Durand et al. (2008) carried out sensitivity studies and simulations of mountain snowpack brightness temperature with MEMLS (Wiesmann and Mätzler, 1999). The uncertainties attributed to not knowing the density of ice layers were 32.2 K and 15.3 K, for horizontally polarised (H-pol) 18.7 GHz and 36.5 GHz frequencies respectively. This was a greater uncertainty than any other parameter investigated (Durand et al., 2008). An increase in the number of mid-season melt and rain-on-snow events in a warming climate is likely to increase the occurrence of ice layers and the importance of accurate ice layer representation in snow emission models (Derksen et al., 2012a).

Chapter 3

Digitising Snowpack Stratigraphy with Improved Accuracy

3.1 Research aims and objectives

Based on the gaps in the literature described in Chapter 1, four problems have been identified. The problems will be solved by achieving their associated research aim and objectives as outlined below:

- **Problem 1:**

  Using NIR photography to digitise stratigraphy is too time consuming to be useful at a large spatial or temporal scale

- Aim:

  To increase efficiency with which NIR photography can be collected in the field and optimise post-processing digitisation procedure

  - Objective 1: To find alternatives to, or negate the need for, the more time consuming aspects of field methods
  - Objective 2: To automate aspects of the post processing procedure to reduce time required for digitisation

- **Problem 2:**

  It is not possible to assign in situ snowpack measurements to digitised layer positions on uneven terrain without subjective human input

- Aim:

  To improve accuracy of digitised snow stratigraphy across a 5 m snow trench for use in all environments

  - Objective 1: To adapt existing field method to better record information of scale
  - Objective 2: To account for the variation in scale within the trench in post processing
  - Objective 3: To develop an automated approach for assigning snow properties to snow layers based on the location of the measurement in the trench, and the location of the digitised snow layer

- **Problem 3:**

  The impact of variability within snow layers on brightness temperature simulations from snow emission models at the plot scale is unknown

- Aim:

  To characterise variability within snow layers along a 5 m trench, and determine the impact of this variability on simulated brightness temperatures from the n-layer Helsinki University of Technology snow emission model (n-HUT)

  - Objective 1: To use automated technique from Aim 2 to assign snow properties to layers and characterise variability in snow layer properties across the snowpack
  - Objective 2: To run n-HUT snow emission model at all points along 5 m trenches

- **Problem 4:**

  Roughness of snow layers within the snowpack is unknown, yet is theoretically a very sensitive parameter for snow emission models

- Aim:

  To quantify internal snow layer boundary roughness

  - Objective 1: To use the more accurate digitised snowpack stratigraphy from Aim 2 to calculate roughness metrics for snow layer boundary roughness

- Objective 2: To characterise and quantify variation in snow layer boundary roughness within and between different snowpacks

3.2 Development of stratigraphy digitisation method

Tape et al. (2010) developed a method to identify and quantify snowpack stratigraphy using near infra-red (NIR) photography. By adapting a Fuji S9100 digital camera to be sensitive to light with mid-point wavelength of 850nm and photographing the side of a snow trench at 50 cm horizontal intervals, the stratigraphy of the snowpack became more apparent and could be quantified digitally from the photographs (Matzl and Schneebeli, 2006). In the field, snowpack properties were recorded for each snow layer along the trench. This section presents a series of optimisations and improvements which have been made to the initial methodology from Tape et al. (2010). They both, improve the ease with which snow stratigraphy data can be collected from the NIR photography, and offer improvements in the accuracy and precision of that data addressing Aims 1 and 2 in the previous section.

3.2.1 Preparing the NIR images

The techniques described here can be applied to any NIR images which are obtained using a field methodology similar to that described in Tape et al. (2010). All the examples are taken from fieldwork carried out at Churchill MB, Canada in the winter of 2010/2011 (described in Section 3.3). The trench images contain horizontal and vertical points of reference, a horizontal measuring staff which covers the entire length of the trench and a vertical metre rule or additional measuring staff which is positioned on the trench for each photo (Figure 3.1). Each trench is 5 m long and covered by 10 individual images, taken at 50 cm intervals.

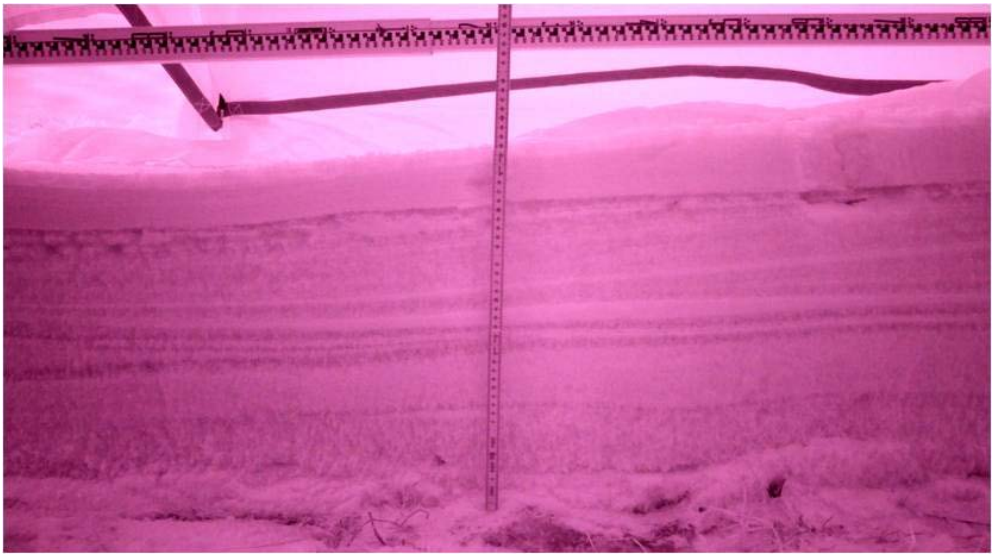

FIGURE 3.1: An example of NIR snow trench photography

The images were stitched into one large image covering the entire trench, however, before this, they needed to be corrected for lens barrel distortion. In past work the commercial software PTgui has been used to carry out this correction (Tape et al.,

2010). Here the open source alternative Hugin (*Hugin* 2011) is used as it offered better scripting capabilities for processing a high volume of images. Figure 3.2 shows the final stitched NIR image from this process that is now suitable for layer identification and digitisation. The example trench is the first trench collected on an open tundra site at Churchill MB in 2012, this is described in section 3.3.

FIGURE 3.2: NIR images stitched together to show stratigraphy across trench

3.2.2 Extracting snow stratigraphy information from NIR snow trench photography

Previously the pixel locations of the layers in the snowpack were recorded one by one to record the snowpack stratigraphy. This was a time consuming and laborious process, which made editing the location of the snow layers and correcting any mistakes difficult and time consuming.

Snowpack digitisation was made more efficient by recording the location of the snow layers in the snowpack using Adobe Illustrator image processing software. Two layers were used in the software, one containing the images from the NIR photography and a second containing the stratigraphy of the snow. Each layer identified in the snowpack was drawn in a different colour over the image and once all the layers had been drawn the layer containing the NIR photography

was turned off, leaving an image the same size as the NIR photography, but only containing the digitised snow layers. The layer locations (in pixels) were extracted from the image using the Image Processing Toolbox in MATLAB, and the different layers identified and separated using their RGB values. The output from this process for the example trench is shown in figure 3.3.

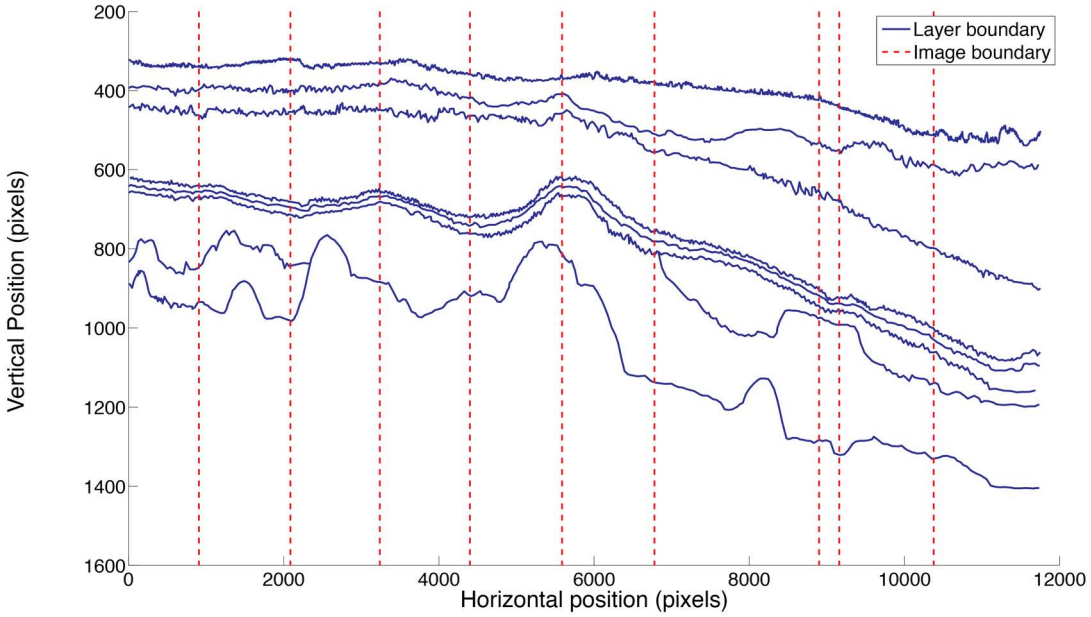

FIGURE 3.3: Position of digitalized snow layers in pixels, i.e. before pixel locations have been translated into geo-referenced cm co-ordinates

Snow and radiative transfer models require snowpack snow layer heights that are parameterised in cm. By measuring the graduations on the horizontal and vertical measuring devices it is possible to convert a pixel × pixel co-ordinate read from the image in MATLAB into a cm × cm co-ordinate.

3.2.3 Calculating positions in digital images in cm

In Tape et al. (2010) and Rutter et al. (2014) a manual graduation size quantification method is used. The location of graduations and the number of pixels between them can be quantified using the Matlab image processing toolbox which records the locations of points located with a cursor on the image. Here the horizontal pixel per cm values were measured using a more automated method, which completely removes the element of human error from the process and also decreases the time taken by a factor of approximately ten.

To measure the graduations a GUI has been developed where a line is drawn over the graduations of the staff (Figure 3.4) and the distance between every edge under that line measured automatically. From this, the number of pixels between each graduation can be determined as well as their exact location on the image. To do this the Canny edge detection algorithm (Canny, 1986) is applied to the image, as shown in Figure 3.4b. The Canny algorithm works by applying a Gaussian filter to the image and the regions of the image with a high spatial derivative are then highlighted to create a gradient magnitude image. Edges are determined by the location of ridges in the gradient magnitude image, the algorithm tracks along the ridges setting all other values to zero thereby defining the image edges. Two threshold values, T1 and T2, are set as parameters where T1>T2. Tracking can only start at a location on a ridge where the pixel brightness value, or ridge height is greater than T1, and continues out from the starting point in all directions until

the ridge height is less than T2 (Canny, 1986). The parameters are set to identify the outline of the graduations on the measuring staff. Noise, identified as edges less than 10 pixels in length, is then removed from the image. When a line is drawn over these detected edges using a GUI, the pixel co-ordinates of the points underneath that line are checked against the binary edge image created by the Canny algorithm. By doing this the position of edges can be detected. After the locations have been recorded, any errors (such as areas where the graduations are obscured) are removed manually from the data.

(A) Measuring staff prior to applying edge detection

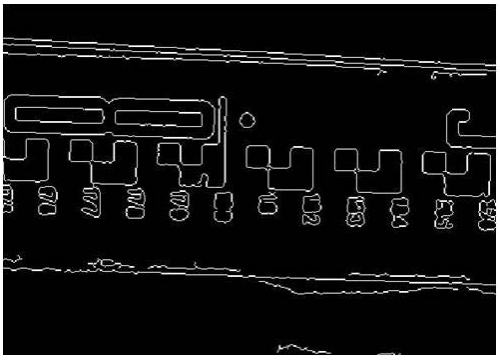

(B) Measuring staff after applying edge detection algorithm

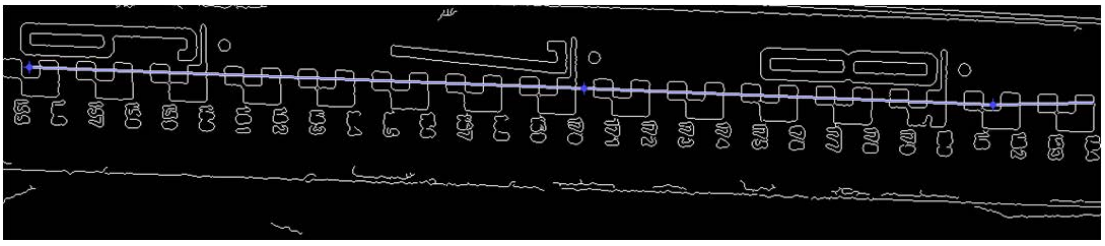

(C) GUI for quantifying size of cm graduations in pixels

FIGURE 3.4: The impact of applying the canny edge detection algorithm to a measuring staff to assist in determining the pixel per cm ratio across a snow trench

To convert the pixels per graduation into a geo-referenced location efficiently the variation in pixel per cm values across the image are converted into a translation

matrix (**T**). **T** is the same size as the stitched image, where each cell contains a decimal value which, when divided by the pixel co-ordinates of that location, returns that same location as a geo-referenced cm by cm x, y co-ordinate. The purpose of this is to allow snow layer boundaries to be identified on the stitched trench image and then quickly converted into a format for use in mathematical models or in the measurement of roughness. Once **T** has been created changes can be made to the digitised stratigraphy image and quickly converted into cm.

To create the translation matrix, Tape et al. (2010) used one pixel per cm value for a trench and used this to translate every co-ordinate of a snow layer using Equations 3.1 and 3.2, where cm_x and cm_y are the horizontal and vertical location of a point in cm, p_x and p_y are the horizontal and vertical location of a point in pixels, and g_x and g_y the average pixel per graduation values in the x and y dimensions respectively.

$$cm_x = \frac{p_x}{g_x}, \tag{3.1}$$

$$cm_y = \frac{p_y}{g_y}, \tag{3.2}$$

This method can yield accurate results when applied on a smooth surface such as

a frozen lake (Tape et al., 2010), but when applied to more varied terrain error increases. One source of error occurs because small variations in the distance between the trench face and the camera, of just a couple of cm, can vary the pixel per cm ratio across the image. On a flat surface it is easier to ensure that this distance remains constant, but in a tundra region the surface is uneven and covered in vegetation, making it almost impossible to achieve the kind of precision required to negate this error.

If every graduation across an image is quantified, a very accurate per pixel method (PPM) of translating between pixels and cm can be implemented. The number of pixels which constitute a single cm graduation is defined as p_g and so, within that cm of the trench image the size of a pixel in cm equals $1/p_g$.

The translation from pixels to cm using the translation matrix ($\mathbf{T}$), of i rows and j columns, can be described using matrix algebra as follows, where p is the position of point to be calculated in pixels and c is the position of the point in cm:

$$c = \sum_{j=1}^{p} \mathbf{T}_{i=1,j} \tag{3.3}$$

Taking the pixel co-ordinate of the end of the measuring staff in the one value per trench method, and translating that position into cm gives a value of 502

cm, compared to 518 cm using the per pixel method, this technique represents a significant increase in accuracy over the existing methodology.

3.2.4 Accounting for artefacts in digitised snow stratigraphy information

While this new method of geo-locating positions in NIR imagery provides substantial benefits, both in terms of increasing accuracy and reducing uncertainty, there is an issue that has been recognised, where abrupt discontinuities can occur in the digitised snow layer boundary positions where adjacent images meet. When vertical positions are calculated using the cumulative per pixel translation method, these values differ between images and, as a result, a step in layer boundary height can occur between images. The best way to illustrate this is to draw a horizontal layer across the stitched snow trench image, and then digitise this line. Figure 3.5 shows the output from this process; discontinuities at image boundaries are very apparent. In the same way when layer boundaries in a snow trench are digitised (Figure 3.6) the same discontinuities are visible at the image join locations. Removal of these discontinuities is not a simple process of subtracting the height of the discontinuity from each layer. As the true location of the horizontal layer is not known, such a simple subtraction would increase uncertainty i.e. the horizontal layer drawn on the images would not be equal to the digitised layer with the discontinuities height removed. Instead the influence

of the abrupt discontinuity would occur more gradually over a larger area of the layer.

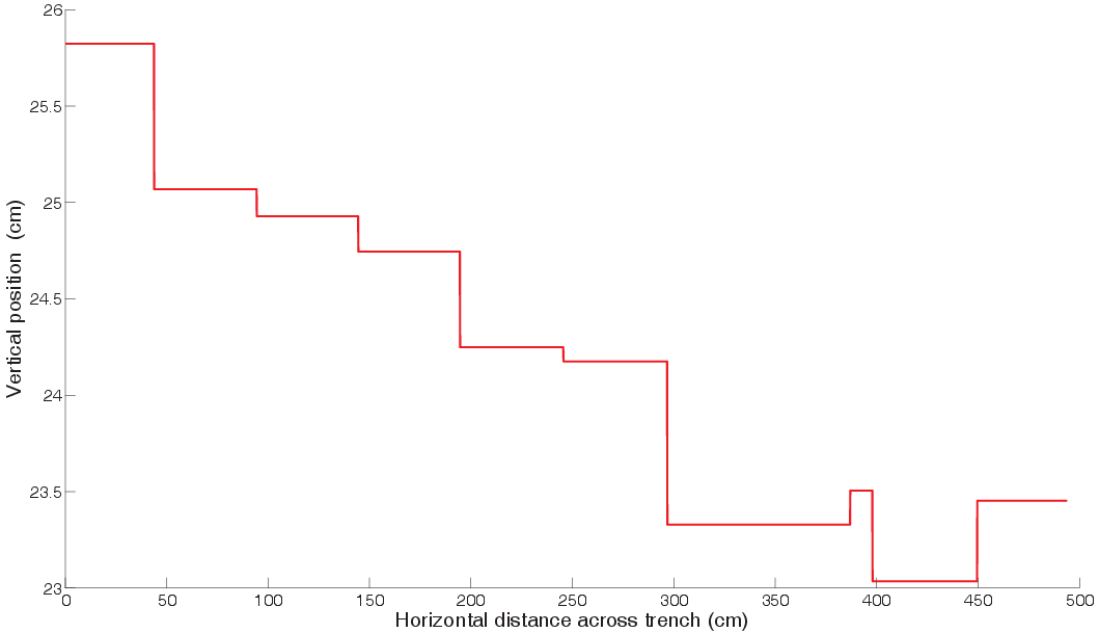

FIGURE 3.5: Horizontal test layer translated using the per pixel translation method

Despite the visual impact of the abrupt discontinuities (for comparison Figure 3.3 shows the raw data from the snow trench, prior to translation and therefore missing the discontinuities) it is only necessary to consider methods of accounting for the discontinuities if they have the potential to impact on the data outputs e.g. the calculation of layer boundary roughness. There are many potential methods which can be used to measure boundary roughness, here the random roughness metric is used, which is simply the standard deviation (SD) of the layer boundary elevation from the mean boundary elevation (Fassnacht et al., 2009b). This roughness metric is used because it is effective at describing layer boundary roughness at a variety of scales and is very fast to calculate, making it suitable

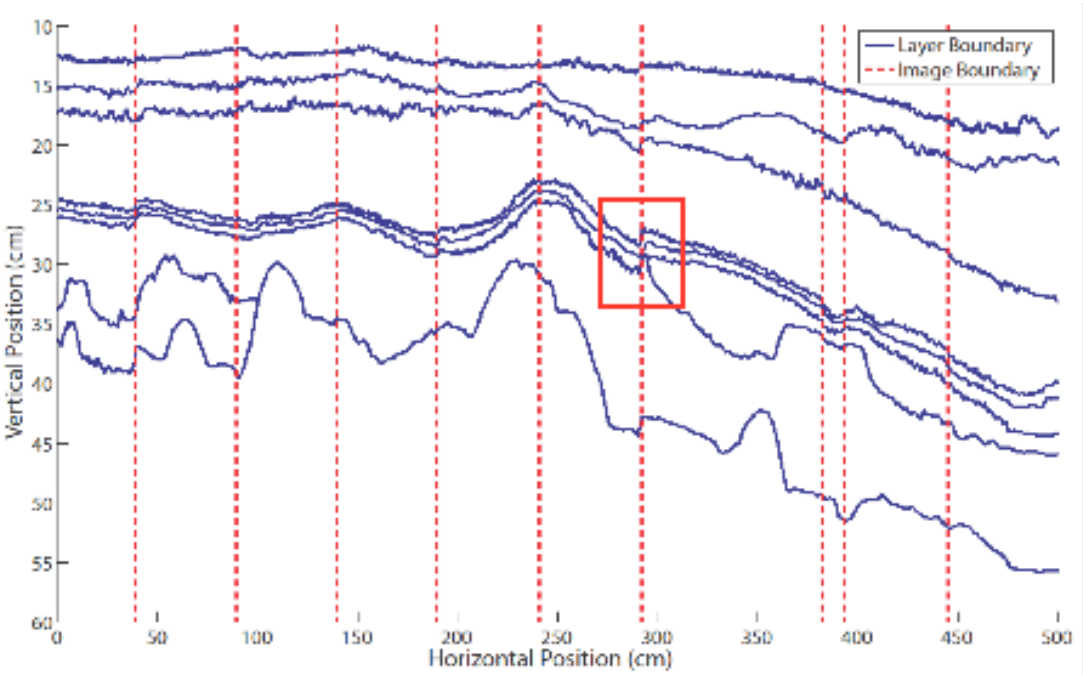

FIGURE 3.6: Un-smoothed snow layers quantified from NIR photography of snow trench wall, Red box indicates area displayed in Figure 3.7

for the iterative method which is used in section 3.2.4.2. If the random roughness metric is applied to the section of the layer boundaries highlighted in Figure 3.6 the impact of the discontinuity on layer boundary roughness is substantial (Figure 3.7). If the roughness metric is applied across an entire trench, histograms of layer boundary roughness values allow comparisons of image join roughness along the layer boundary.

Figure 3.8a shows that several of the roughness values at image joins lie outside the mean plus one standard deviation. For this reason, a method for removing these discontinuities, while minimising the impact on the rest of the layer has been developed.

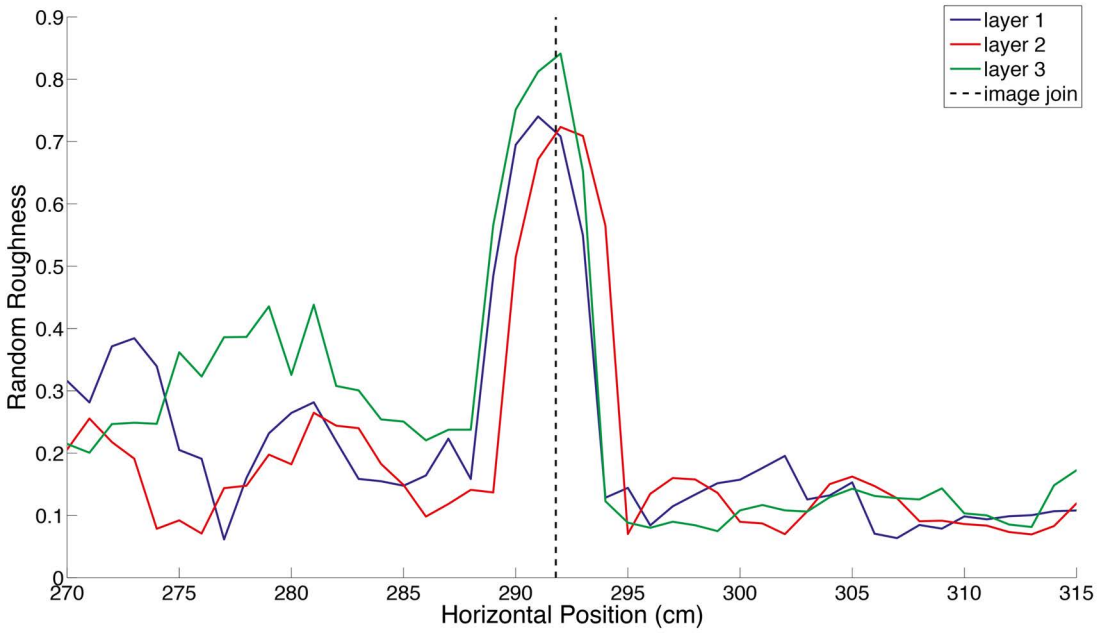

FIGURE 3.7: Random roughness over the section highlighted in Figure 3.6, layers numbered in descending order according to height

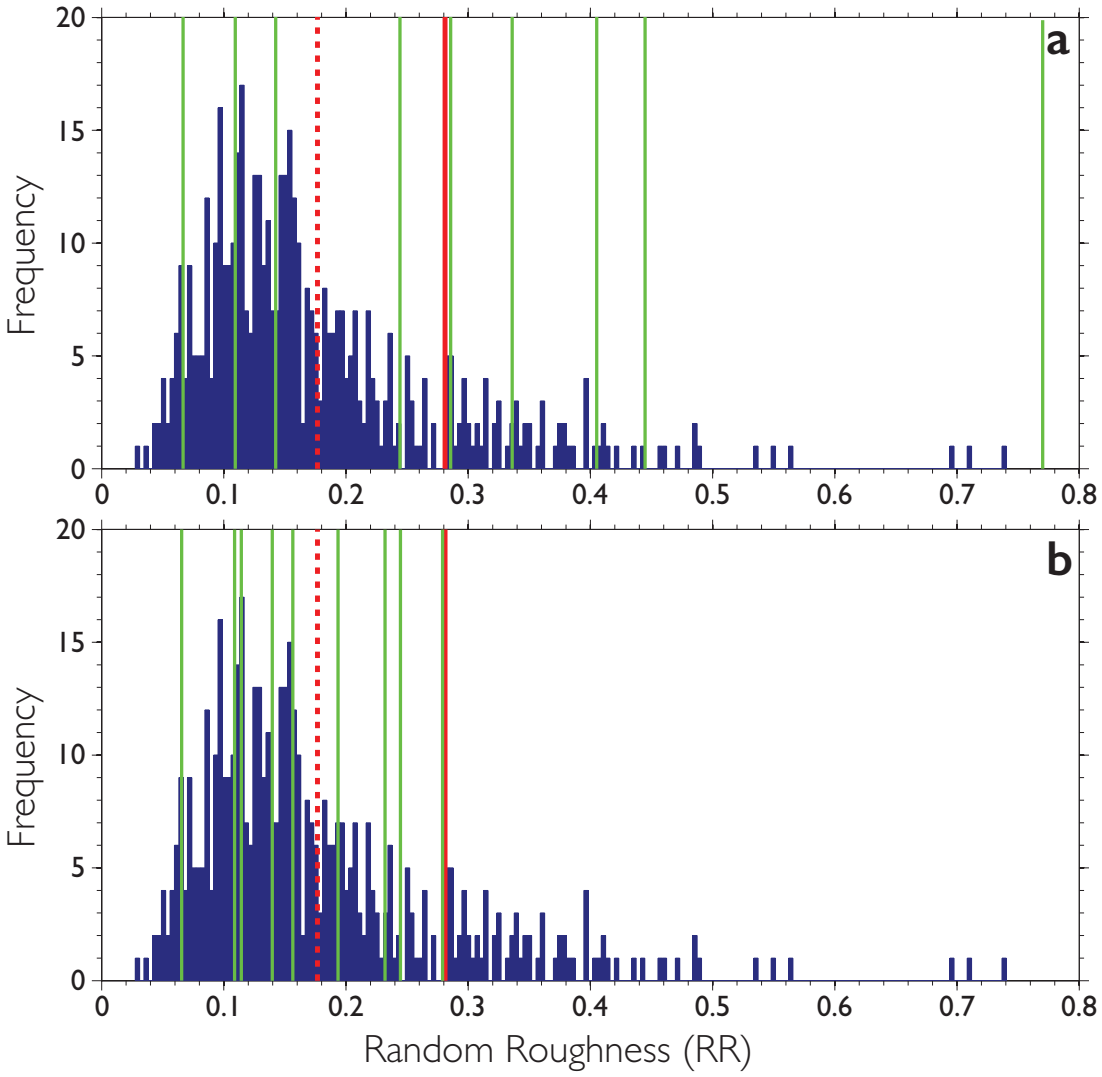

FIGURE 3.8: a) Histogram of the random roughness metric for a sample snow layer showing location of image boundaries in green b) Histogram of the random roughness metric for a sample snow layer showing location of image boundaries in green after smoothing has been applied

3.2.4.1 Applying smoothing

From a stitched image the locations where image boundaries occur are recorded. The discontinuity that occurs in the translation array over the join is measured and smoothing is applied by taking the value for pixels either side of the join, and linearly interpolating the values between these points. Interpolation over the discontinuity (from horizontal positions x_0 to x_1) is carried out using

$$T = T_0 + (T_1 - T_0)\frac{x - x_0}{x_1 - x_0} \tag{3.4}$$

Where T is the translation value for the horizontal position x. This is applied to the translation array automatically for every row and at every image join location; the degree of smoothing is defined as $x_1 - x_0$.

3.2.4.2 Smoothing Optimisation

An iterative process was used to determine the optimum level of smoothing, (the number of pixels to smooth either side of the join), to apply over snow trench image joins. The random roughness over the joins was measured for a layer boundary, if any joins had a roughness greater than the mean of that layer plus 1 standard deviation then two pixels either side of the image join were smoothed, and the test repeated. The level of smoothing was increased until the

roughness for all joins on that layer boundary were less than the mean plus one standard deviation. An upper limit of smoothing was also set in the case that it is not possible to reduce roughness adequately over every join. Histograms of the random roughness for each layer boundary before and after smoothing are shown in Figure 3.8. The impact smoothing has directly on the layer boundary roughness is shown in Figure 3.9, which shows the same layer sections as Figure 3.7 after smoothing has been applied. The impact of this smoothing method is visible by comparing the smoothed and unsmoothed snow layer boundaries over the entire trench (Figure 3.6 3.10).

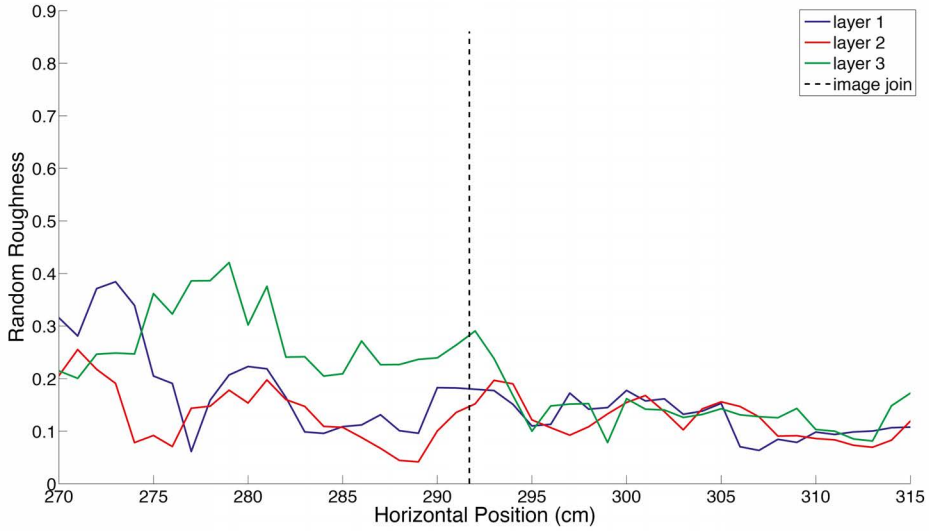

FIGURE 3.9: Random roughness over the section highlighted in Figure 3.6 after smoothing has been applied, layers numbered in descending order according to height.

The smoothing methodology described in section 3.2.4.1 can be optimised to favour either a smoother transition across a join or a higher proportion of the layer represented by the data in each image, i.e. if the the gradient in the translation

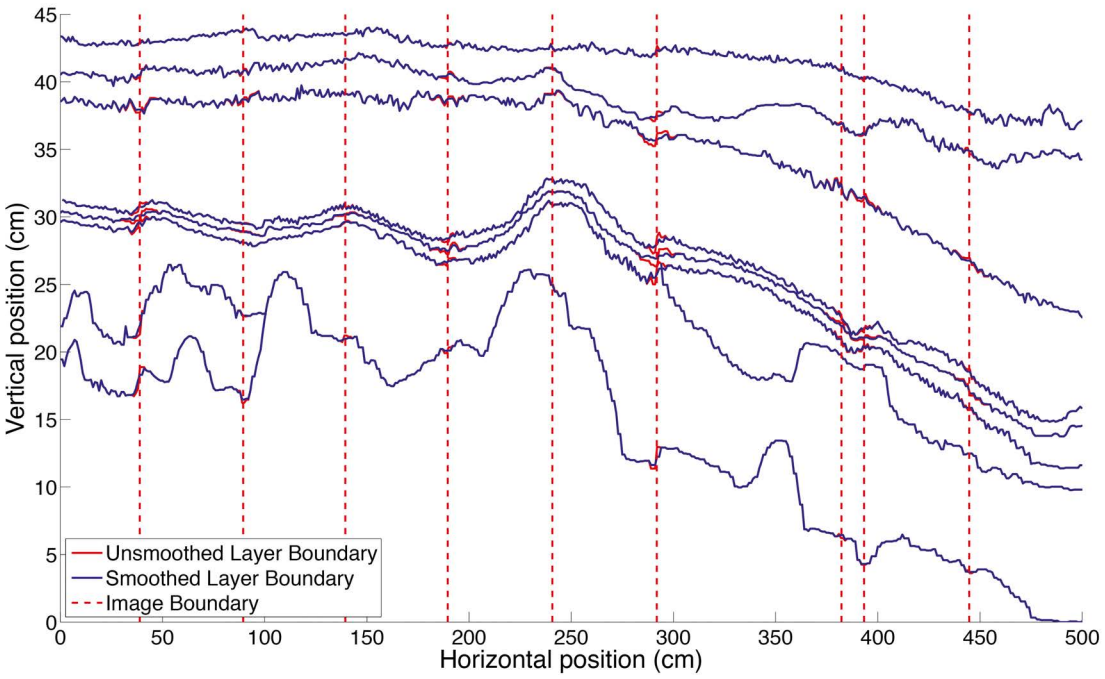

FIGURE 3.10: Impact of smoothing on whole trench

between each image the flatter, less of that layer is at its original unsmoothed location. In order to determine the optimum level of smooting the effect of the artefacts on snow surface roughness metrics (Fassnacht et al., 2009b) is measured. When the artefacts no longer affect the random roughness metric, the standard deviation of the difference between the surface elevation and the mean surface, then the correct level of smoothing has been applied.

Figure 3.8a shows a histogram of the random roughness metric for the surface layer of a snow trench, the mean (dashed red vertical line) and 1 standard deviation from the mean (red vertical lines) are also marked, the random roughness values of the artefacts are marked by green vertical lines. If we categorise the histogram into signal and noise, noise being any reading within one standard deviation of the mean it is clear that several of the artefacts impact on the signal. As smoothing

is applied to the translation matrix the impact of these artefacts decreases. We increase the smoothing level until the random roughness metric for the artefact is below one standard deviation of the mean. For this particular layer this is shown in figure 3.8b. Figure 3.9 shows the impact that this level of smoothing has on the roughness metric itself, again at a smoothing level of 16 cm. The effect of the smoothing can be clearly seen at the point of the image join.

Figure 3.6 shows the smoothed snowpack stratigraphy. This method is able to visibly remove the effect of the artefacts on the snow layer as well as crucially remove their impact from the data itself.

3.2.5 Assigning snowpack properties to digitised stratigraphy

In previous work, measurements of snowpack properties taken in the field were assigned to digitised snow layers using a fixed protocol and human interpretation (Rutter et al., 2014). An automated approach was not possible because the exact position of the snow layers was not completely known. With the improved technique described in the previous section it is now possible to locate the position of the measurements in the digitised snow trench and, as a result, automatically assign measured snow properties to snow layers.

Figure 3.11 shows the locations of density measurements in an example 5 m trench in Churchill MB. Where measurements overlapped layers, the value from

that measurement was assigned to that layer. Where more than one measurement existed within a layer, an average of all the measurements in the layer at that horizontal position was taken. The outcome of this automated process was a table of x positions for each layer and a density value attributed to the layer at that point. The same process was used for grain size and temperature data. These values could then be averaged to provide an average value for each property for each layer or interpolated horizontally to give continuous variation in the property value along the layer. Where the layer had a greater spatial extent than the measurements, the value of the furthest left or furthest right value was continued until the end of the trench. No extrapolation took place. Whilst this provides a good graphical representation of the variation in properties that occurs within a trench, it makes an assumption that properties change linearly, which may well not be the case.

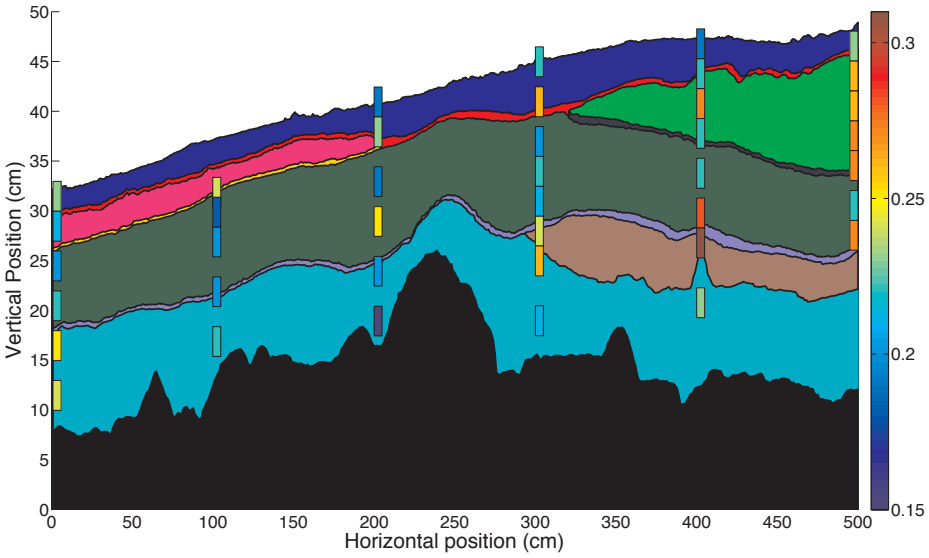

FIGURE 3.11: Locations of density measurements placed automatically on snowpack stratigraphy

3.3 Field Methods

3.3.1 Field Site

Field work was conducted in Churchill MB (58.7692°N -94.169268°W) over the 8-9th January 2011. Churchill is broadly representative of a subarctic tundra region on the northern edge of the tree line. The landcover consists of scattered forest, lakes and large areas of exposed shrub-land (Derksen et al., 2012a). Churchill generally experiences a winter typical of subarctic regions and this was the case in 2010 - 2011. Prevailing winds of approximately 6 m s^{-1}, an average air temperature of -25°C and a winter snowfall of 201 cm were recorded (Environment Canada, 2013).

Four 5 m trenches were dug in total, at two different sites shown in Figure 3.12. The trenches were dug perpendicular to each other to capture stratigraphic variability in three dimensions. Trenches 1 and 2 were dug on an open tundra area located next to a forest. Trenches 3 and 4, were located in a fen and so somewhat more sheltered from the wind. In each trench ten NIR photos were taken overlapping each other by approximately 50 cm and covering the entire length of the 5 m trench. At every meter along the trench snow grain diameter, density, temperature, hardness and manual stratigraphy was recorded. Density was measured using a stainless steel 10 cm^3 snow density cutter and digital scales, grain diameter was recorded using a field microscope, and temperature

was recorded at 4 cm intervals using thermocouples inserted into the snow trench face.

FIGURE 3.12: Locations where trench sampling took place. The red marker shows the location of trenches 1 and 2 and the green marker shows the location of trenches 3 and 4

3.4 Results

The results are split into two main sections. The first section will describe and characterise the snow trenches. Differences and similarities between the snow stratigraphy recorded in the trenches at each site and between the two sites will be outlined. It will also address the variation that occurred within the snow layers within each snow trench. The second section will address the impact of the

variation in snow properties within layers and within the snowpack on simulated brightness temperatures from snow emission models.

3.4.1 Variation in snowpack properties and characteristics

During the winter of 2010-2011 the majority of snow accumulated from precipitation between December and January and while there were precipitation events later in the season, the continuously high wind speeds encouraged wind redistribution and thus snow depths remained shallow into the latter half of the season (King et al., 2014).

Overall the snowpack was characterised as having 10 - 20 cm of depth hoar at the base of the pack overlaid with wind and melt-refreeze crusts between layers of wind slab. Depth hoar growth occurs when a strong temperature gradient is present (Baunach et al., 2001). This is demonstrated by the increased thickness of depth hoar in trenches 1 and 2 where depth hoar formed in the hummocks and undulations on the tundra surface.

Figure 3.13 summarises the difference in snow depth and SWE for all for trenches. Trenches 1 and 2 had a wider range of depths than Trenches 3 and 4, this was caused by the more hummocky undulating subnivean topography but comparatively smooth snow surface at the open tundra site. At the fen site where trenches 3 and 4 were located the subnivean surface was much less hummocky. The snow depth was greater at the open tundra site, although the SWE for that site was not

significantly greater. This is explained by the hard compacted, high density wind slab which formed the upper part of the snowpack on the tundra site. The fen site had a much softer looser upper snowpack consisting mainly of larger facetted grains or freshly deposited snow which was decomposing on the surface. Figure 3.14 shows the variation which occurred within the snow layers in each snowpack, the layers are organised so the bottom layer is on the right hand side of each plot, and the upper on the left.

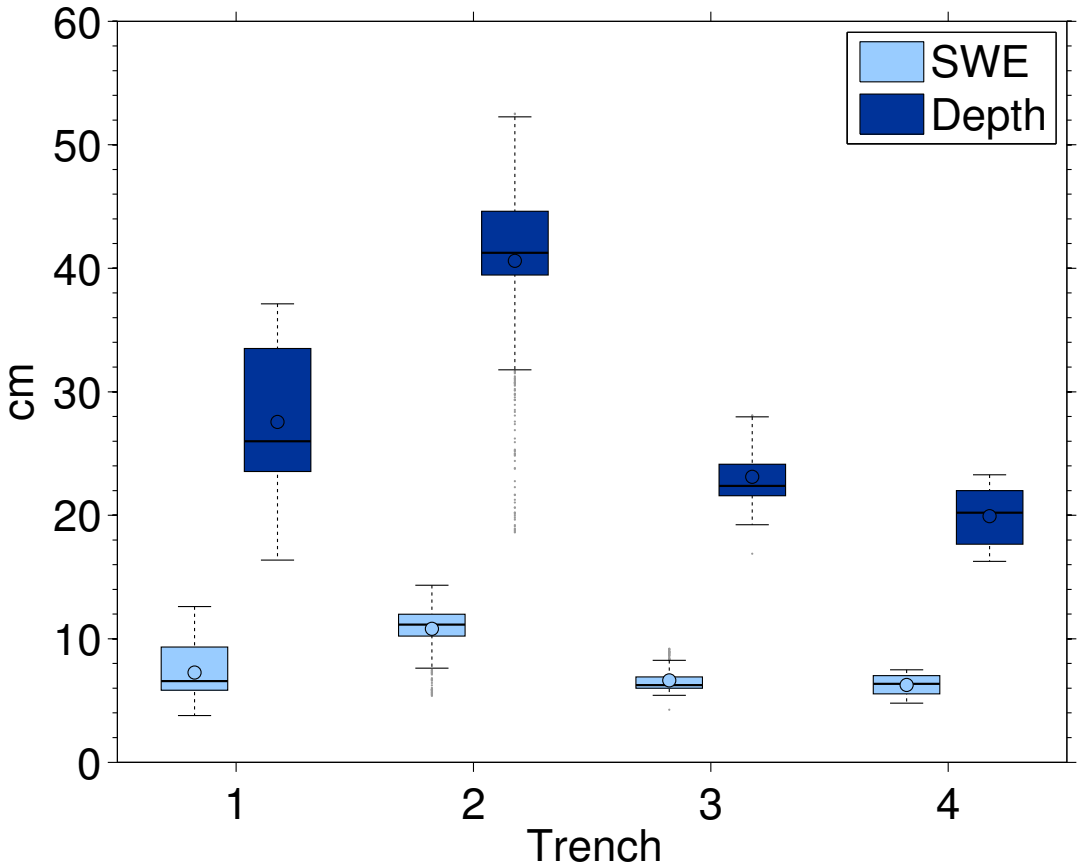

FIGURE 3.13: Difference in range of total snowpack SWE and Depth measurements across entire trench. The whiskers of each plot are the lowest or highest datapoint within 1.5× the interquartile range. The boxes cover the 1st to third quartile the median marked by a line and the mean by a hollow circle, this convention is used for all subsequent box plots.

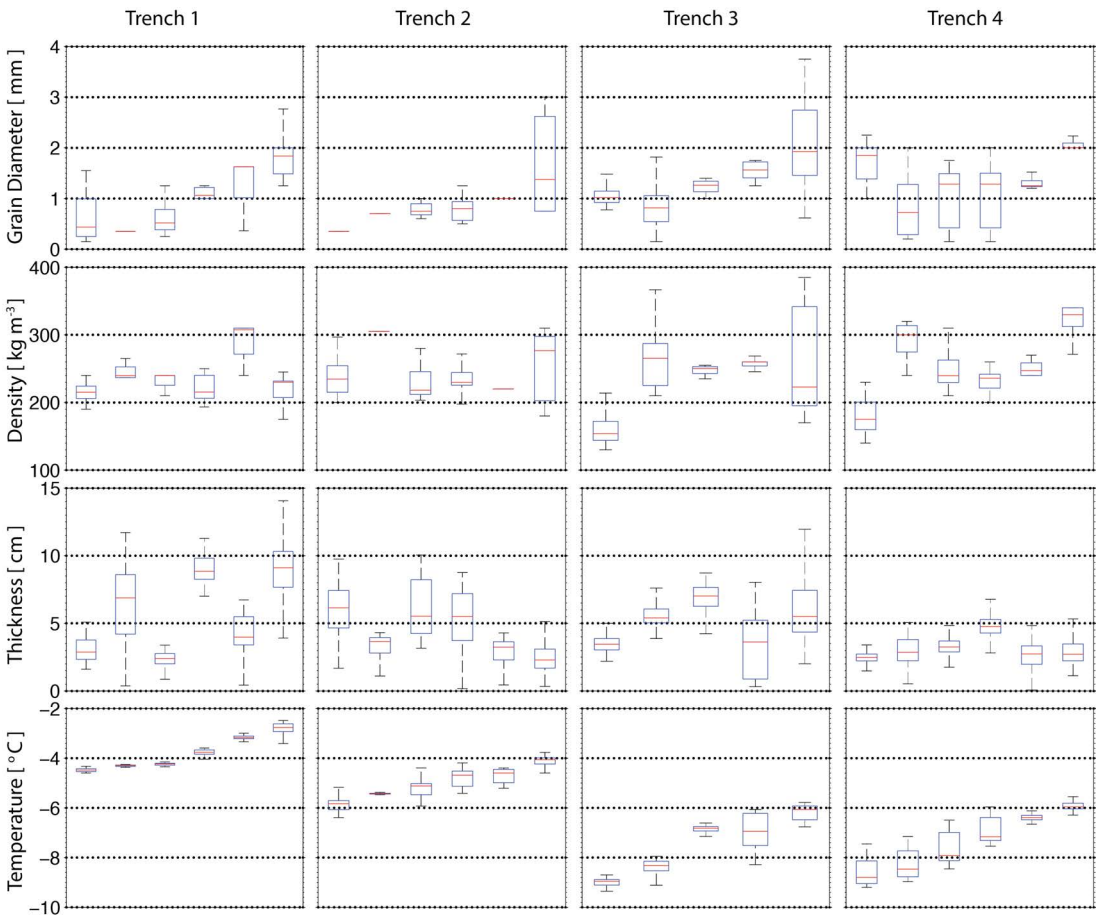

FIGURE 3.14: Variation in snow properties within and between layers in each trench.

The stratigraphic information digitised from the snow trenches 1 to 4 is shown in Figures 3.16 to 3.19 respectively, snow grain type symbols are taken from Fierz et al. (2009) and a guide can be found in Figure 3.15. These Figures provide a visualisation of the variation which exists within the layers of the snowpack. Figure 3.20 shows how trenches 1 and 2 are related to each other spatially. By considering Figures 3.16 and 3.17 in relation to Figure 3.20 (the colour scales are identical) you can see that properties such as grain diameter and density exhibit a similar level of variability in both trenches, and therefore in both spatial

directions. Trenches 1 and 2 varied more between orthogonal directions, the impact of the wind is evident in the high number of discontinuous layers in trench 2 (5) compared to trench 1 (3). Additionally the depth of Trench 2 was much greater, having an average depth of 38 cm compared to Trench 1 which had an average depth of 28 cm. Between trench 3 and 4 there is less quantifiable difference with both trenches consisting primarily of continuous layers and both trenches having similar average depths, 18 cm compared to 22 cm.

FIGURE 3.15: Snow microstructure and grain type symbols used in this thesis (classification/symbols from Fierz et al. (2009))

The results of the random roughness metrics are shown in Figure 3.21. At the base of the snowpack the greater roughness was observed at Trenches 1 and 2. This reflected the more undulating subnivean topography at this site. However, the roughness dropped off substantially towards the top of the snowpack, and overall trenches 3 and 4 had a higher and more consistent level of roughness throughout the snowpack.

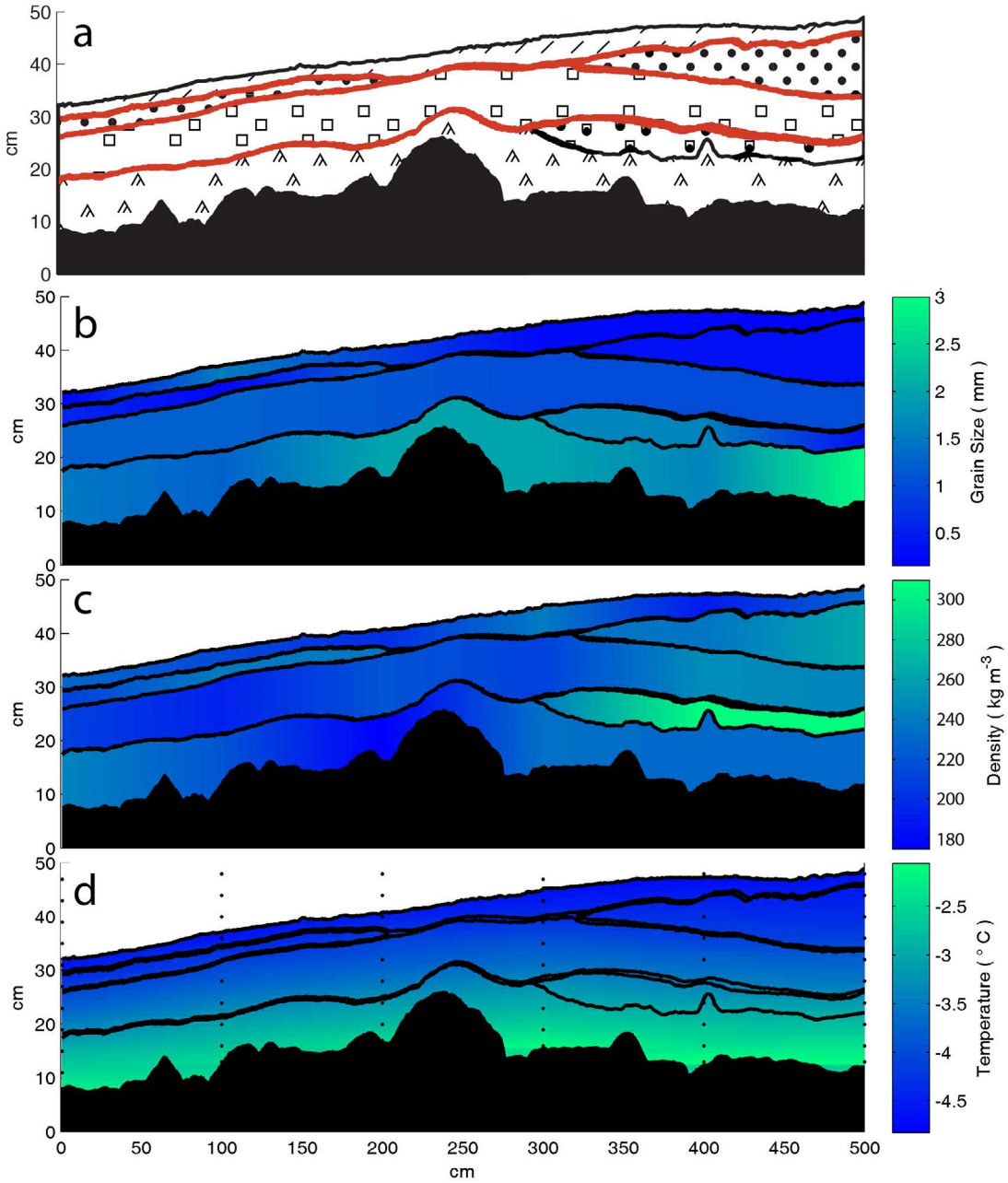

FIGURE 3.16: Stratigraphy and snowpack properties of Trench 1, ice crusts are marked in red on the top image

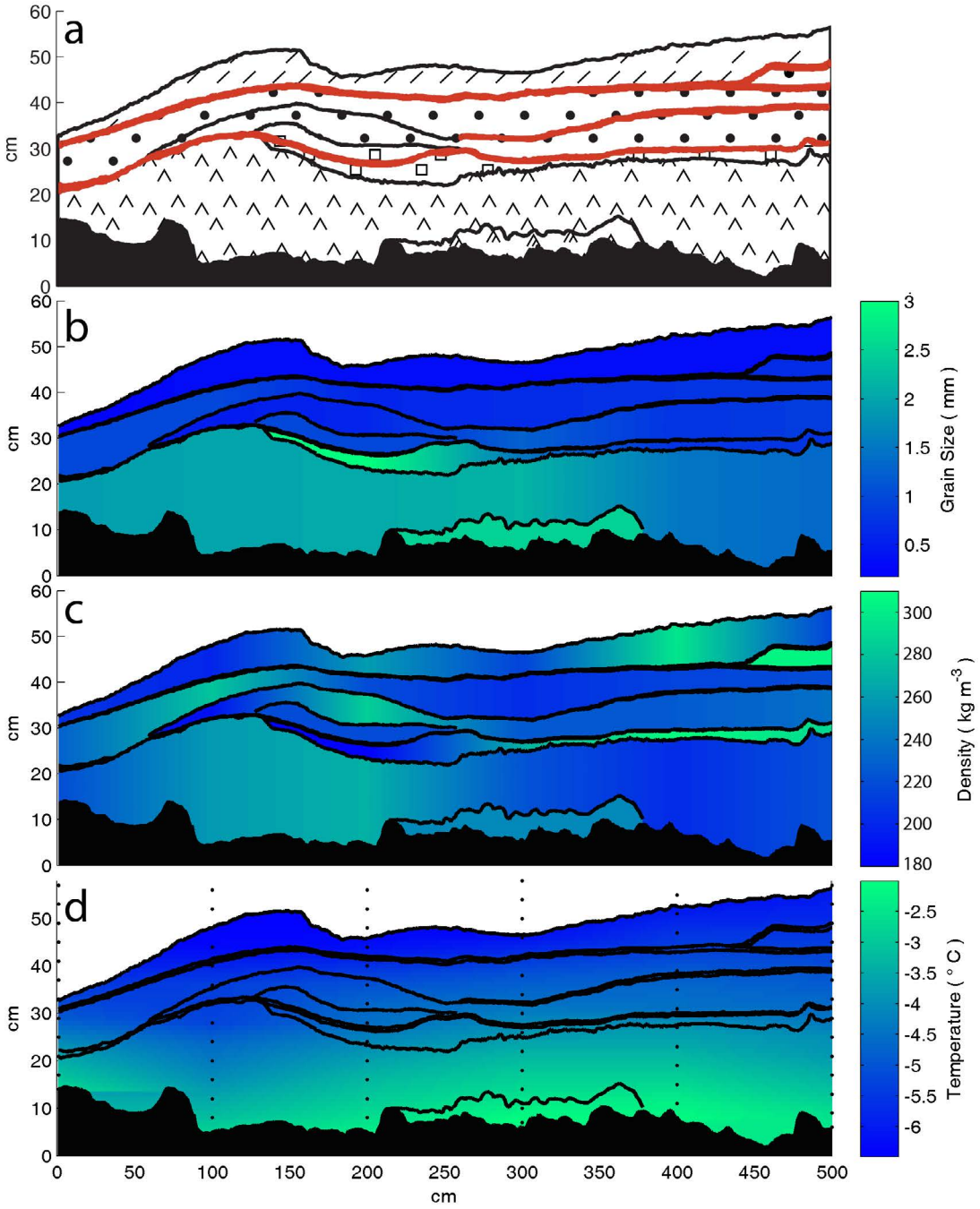

FIGURE 3.17: Stratigraphy and snowpack properties of Trench 2, ice crusts are marked in red on the top image

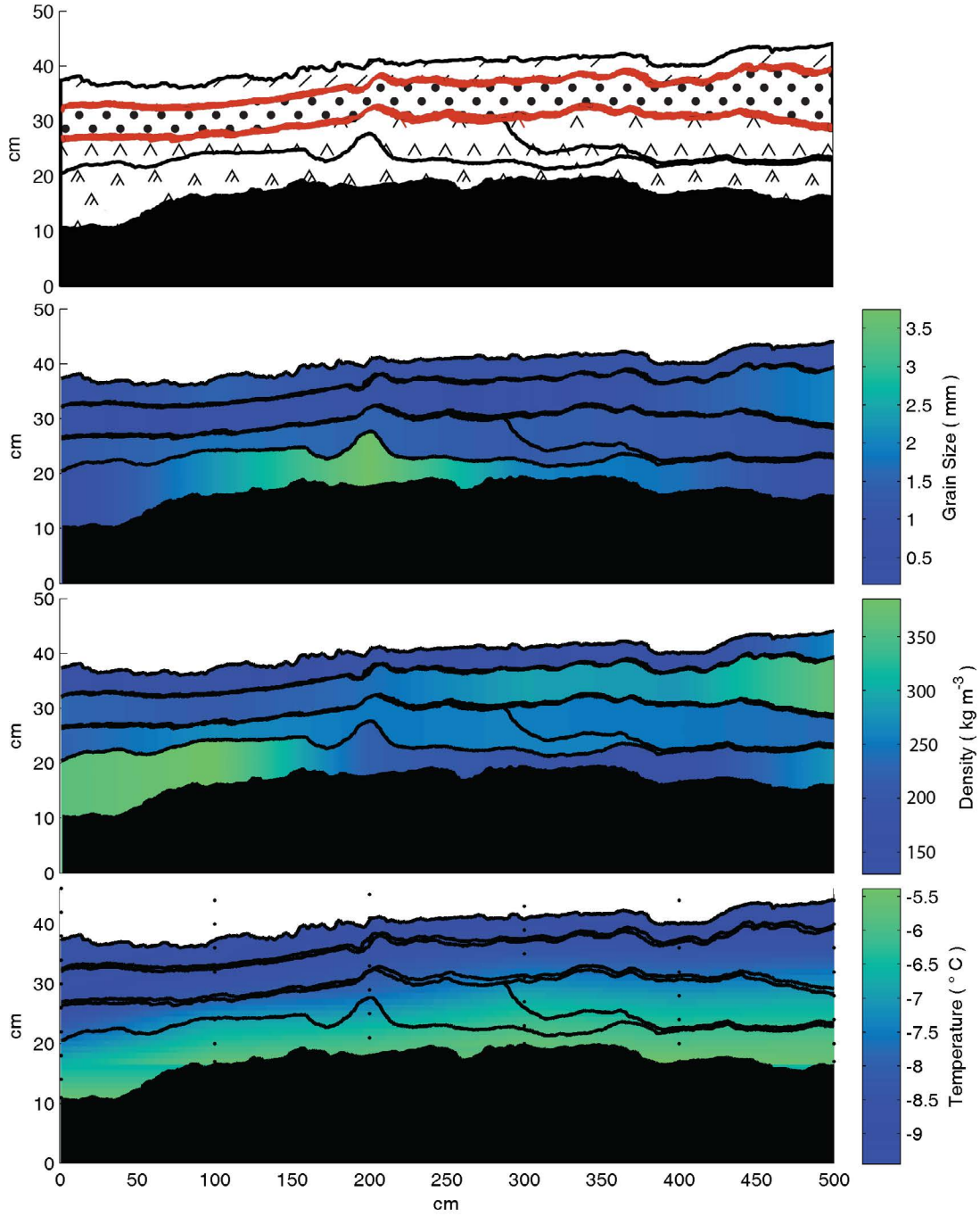

FIGURE 3.18: Stratigraphy and snowpack properties of Trench 3, ice crusts are marked in red on the top image

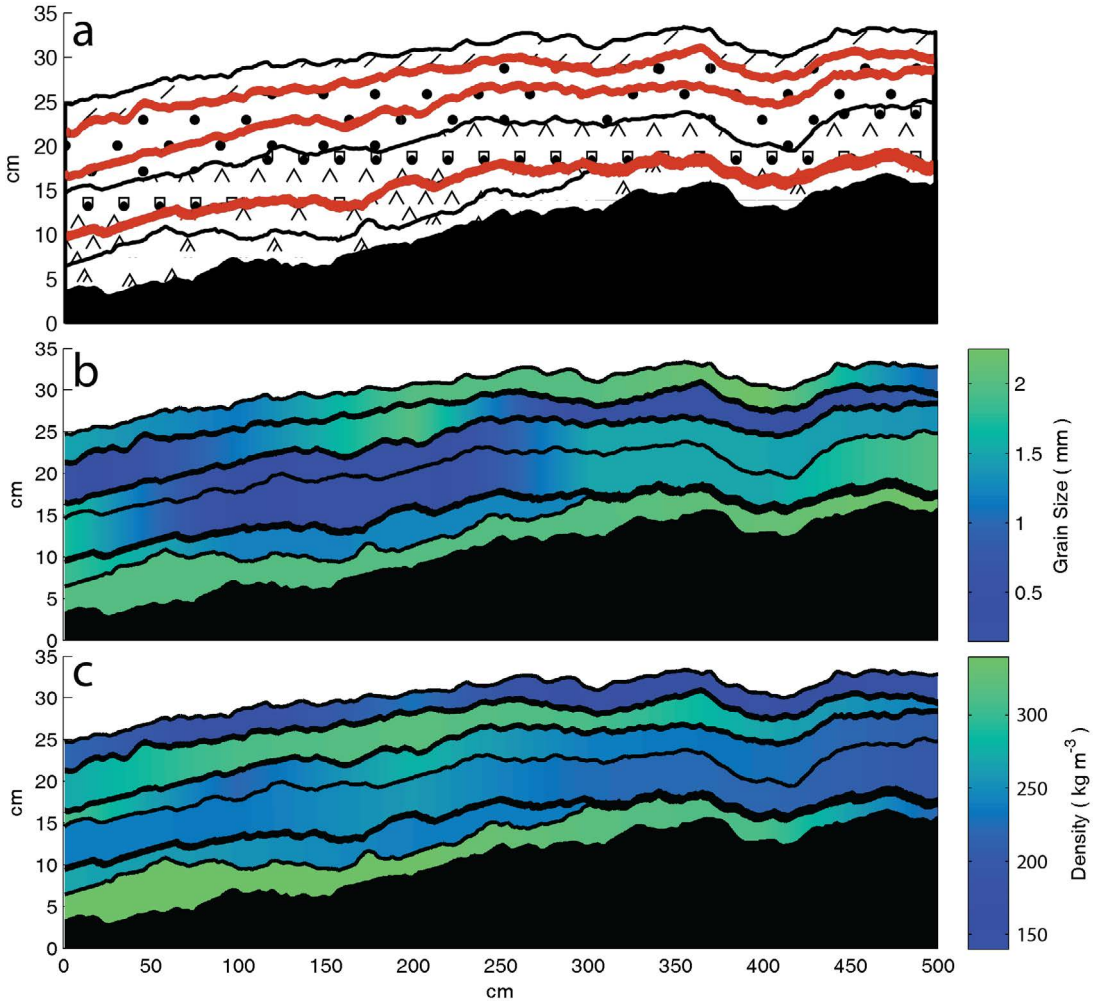

FIGURE 3.19: Stratigraphy and snowpack properties of Trench 4, ice crusts are marked in red on the top image

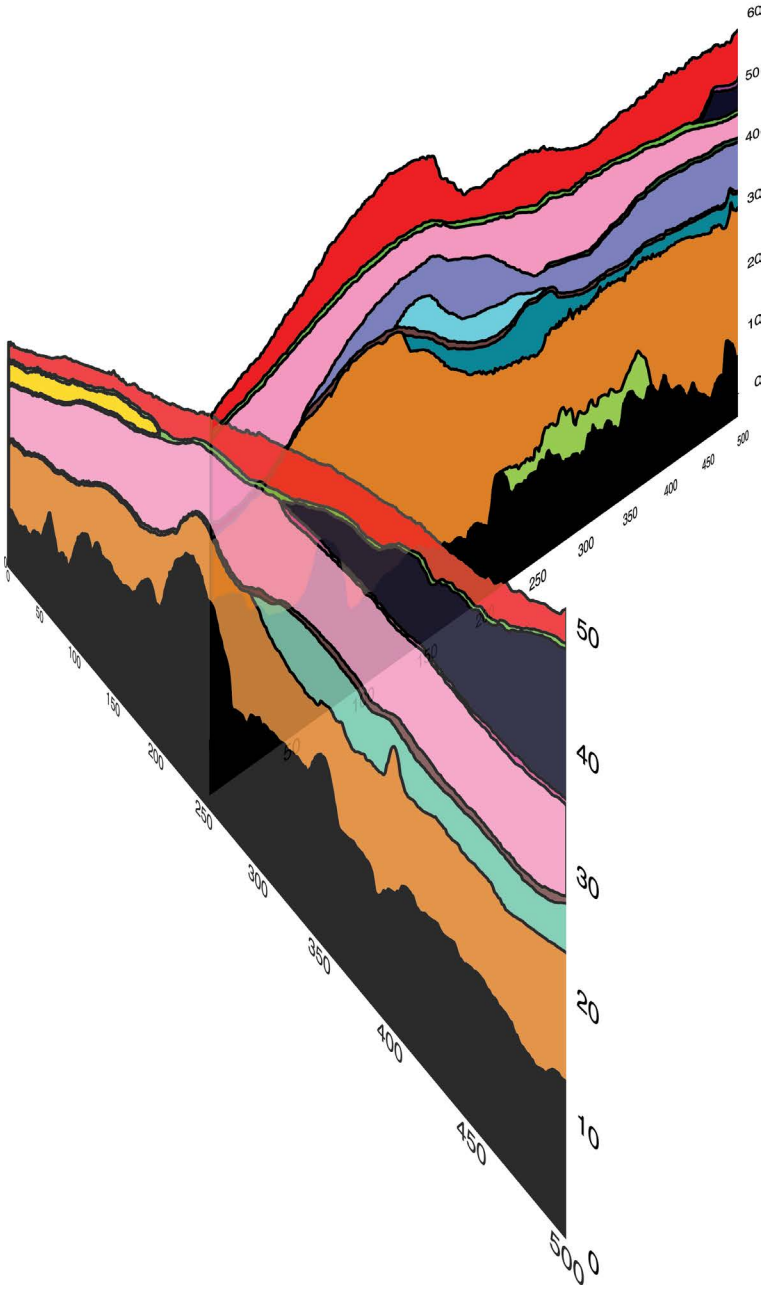

FIGURE 3.20: Stratigraphy from trenches 1 and 2, showing how they relate to each other in three dimensions.

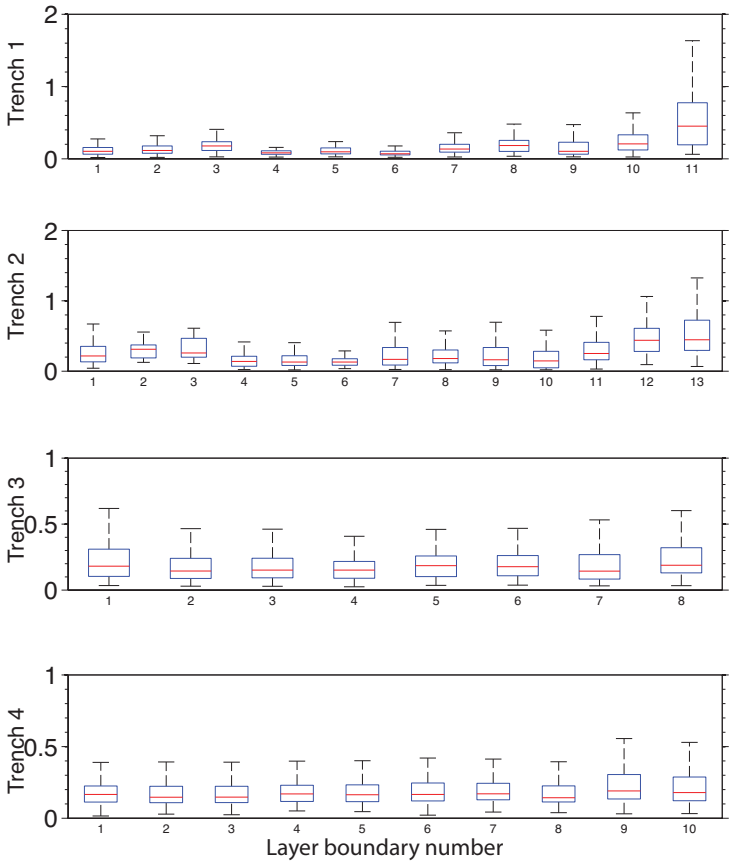

FIGURE 3.21: Boxplots for random roughness.

3.4.2 Variation in n-HUT model Tb

The n-HUT model was initialised with the trench stratigraphy data in three ways, of increasing complexity

1. Bulk Properties: the average of all of the data collected over the course of the trench was averaged into one layer, the n-HUT model was then used to simulate the brightness temperature for this snow layer, the output can be found in Table 3.1.

2. Layered average: The average of each layer is taken to produce one averaged multi-layered snow profile. Properties of discontinuous layers were included with adjacent layers so the overall mean depth was equal to the profile depth. The results from these simulations can be found in Table 3.2.

3. Trench simulation: Properties were averaged for each layer and then the n-HUT run for each horizontal profile. The mean and standard deviations of the brightness temperature distributions can be found in Table 3.3 and the distributions of the simulations found in Figures 3.22 to 3.25.

Table 3.1: Simulated brightness temperatures from using bulk snowpack properties

Trench	19V	19H	37V	37H
1	247	236	208	199
2	244	233	194	186
3	249	237	215	205
4	249	238	219	210

Table 3.2: Simulated brightness temperatures from using averaged snowpack based on trench data

Trench	19V	19H	37V	37H
1	232	158	202	141
2	233	176	188	145
3	238	182	209	161
4	233	163	209	148

Table 3.3: Mean and standard deviations of simulated brightness temperatures from trenches

	Mean			
Trench1	19V	19H	37V	37H
1	186	131	176	125
2	206	149	179	132
3	243	186	213	165
4	239	167	214	151
	Standard Deviation			
Trench	19V	19H	37V	37H
1	1.41	5.22	3.74	6.23
2	2.89	8.89	7.82	9.09
3	0.62	0.46	3.37	2.50
4	0.78	1.16	4.00	3.15

Table 3.4 shows the differences between brightness temperature of each pair of trenches in different orthogonal directions when the different methods of simulating brightness temperature were used. When the bulk, one layer simulation was used there was little difference between trench pairs, with the exception of 37 GHz for trenches 1&2. Overall the disparity between the pairs of trenches increased the more complex the method of simulation used.

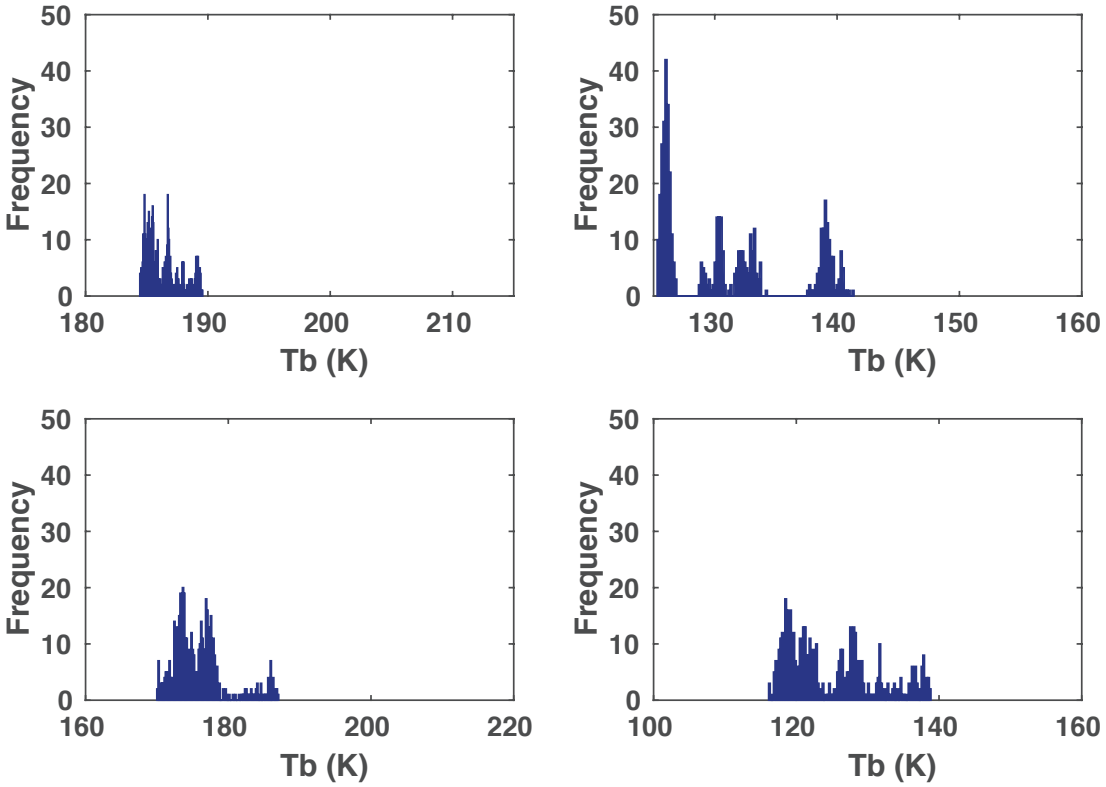

FIGURE 3.22: Histograms showing the distribution of Brightness Temperatures simulations for Trench 1 when variable layer heights are used with the mean properties for top-left)19V, top-right)19H, bottom-left)37V, bottom-right)37H

TABLE 3.4: The absolute difference in simulated brightness temperatures between the pair of orthogonal trenches at each site. Three different methods of using the trench data are compared

	Freq/polariastion	1 layer Bulk	n-layer	mean from trench
Trench 1&2	19V	2.4	1.4	19.9
	19H	2.7	18.3	18.3
	37V	13.6	14.6	2.7
	37H	13.4	4.7	7.6
Trench 3&4	19V	0.3	5.2	4.3
	19H	0.9	19.7	19.3
	37V	3.9	0.1	0.7
	37H	4.3	13.8	13.3
Mean		5.2	9.7	10.8

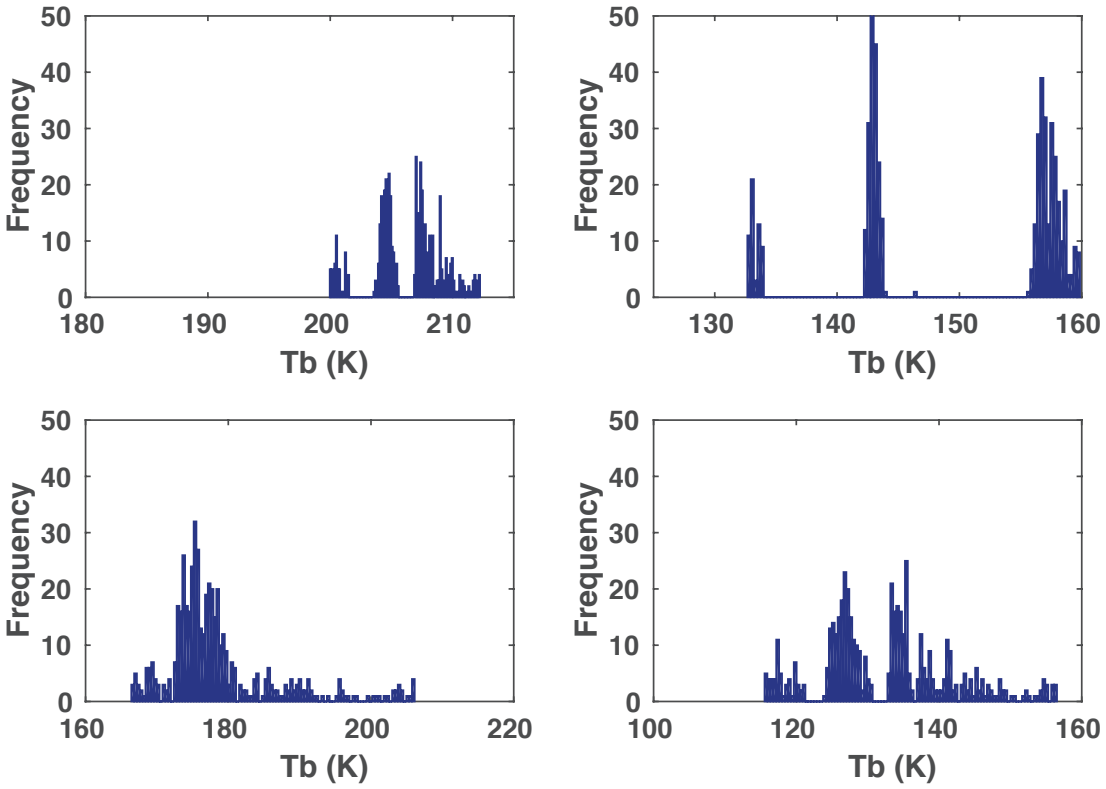

FIGURE 3.23: Histograms showing the distribution of Brightness Temperatures simulations for Trench 2 when variable layer heights are used withe mean properties for top-left)19V, top-right)19H, bottom-left)37V, bottom-right)37H

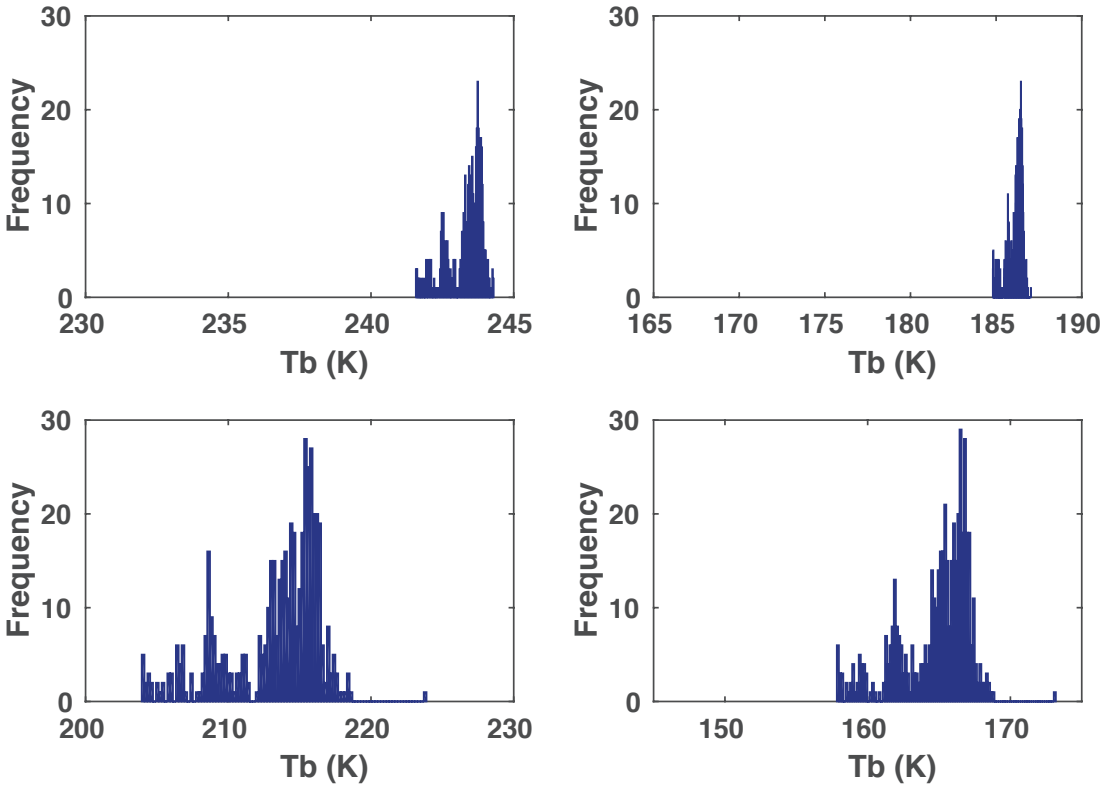

FIGURE 3.24: Histograms showing the distribution of Brightness Temperatures simulations for Trench 3 when variable layer heights are used withe mean properties for top-left)19V, top-right)19H, bottom-left)37V, bottom-right)37H

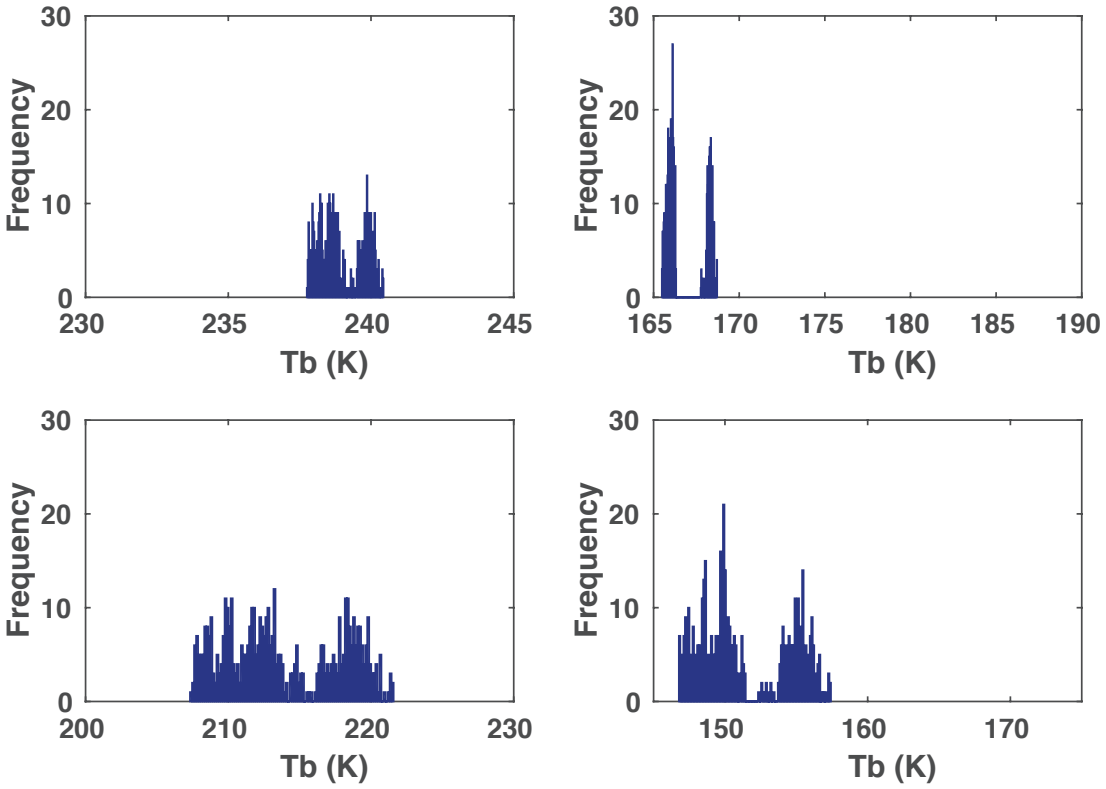

FIGURE 3.25: Histograms showing the distribution of Brightness Temperatures simulations for Trench 4 when variable layer heights are used withe mean properties for top-left)19V, top-right)19H, bottom-left)37V, bottom-right)37H

3.5 Discussion

Quantifying snow stratigraphy from near-infrared photography has the potential to introduce error into the digitised snow profile information, as a result of an imperfect method of translating pixel co-ordinates from a photograph into a geo-referenced location. While past methods of conducting this translation have proved accurate on flat terrain such as frozen lakes, when applied to areas of more varied subnivean terrain large errors are introduced to the digitised snow layer boundary data. To address this problem a semi-automated method of quantifying scale across a stitched snow trench image was developed, allowing for pixel co-ordinates to be translated more accurately. An adverse effect of this method was that discontinuities form in the image, where boundaries in the stitched snow trench image occur. The impact of these artefacts was negated by applying optimal smoothing to the layers at the image joins in an iterative manner. The result is a more accurate method of quantifying snow trench stratigraphy from near infra-red photography that is accurate on a variety of subnivean surfaces and also offers a substantial improvement in efficiency over existing post-processing methods.

The new method was used to measure layer boundary roughness from within the snowpack, a property which has been shown to be important in radar applications (Rott and Mätzler, 1987; Ulaby et al., 1981) but whose impact on passive microwave remote sensing is unknown. It has been demonstrated that there is

substantial variation within the snowpack, and that the degree of variation is likely to depend on the roughness of the subnivean topography. Additionally, the speed of the wind at a site may work to reduce the roughness in the upper layers, and it is believed this was the case at our site, although, it is well documented that very high wind speeds will lead to surface features such as drifts or sastrugi, and so this hypothesis will require further investigation.

The improved accuracy of this method also allowed properties to be assigned to snow layers based on in situ measurements, which removes the subjectivity from previous work. Using this automated technique, the variation of the internal properties of snow layers was investigated. This was found to vary significantly, although the degree of variability was not substantially different when layers from two different trenches at the same site were compared. This implies that one trench is able to capture a significant amount of variability from within a snow layer, although the variation in the stratigraphy itself is significant.

The impact that this variation had on the actual modelled brightness temperature is interesting. The mean brightness temperature from two trenches at the same site is usually very similar, often within sensor noise, when bulk values were used. However, as the stratigraphy was represented with an increased level of accuracy, more variation in brightness temperature simulations was found. Where discontinuous ice layers were present the distribution of simulated brightness temperatures for a trench split so that contained multiple peaks for vertically

polarised radiation. This demonstrates the significant impact that the presence of even a very thin ice layer can have on a snow pack's microwave signature.

Chapter 4

Improved measurement of ice layer densities and application in snow microwave emission models

4.1 Aims

The aim of this chapter, as set out in Chapter 1 is to improve the parameterisation of ice layers in snow emission models by measuring and analysing the influence of their structural properties (such as density and bubble size) on the accuracy of simulated brightness temperatures. This will be achieved by addressing the following three objectives...

1. To develop a new field method for measuring the density of ice layers

2. To compare simulated and observed brightness temperatures using measured ice layer densities to test the sensitivity of the MEMLS and DMRT-ML snow emission models to changes in ice layer parameterisation

3. To examine the impact that any sensitivity could have on ice layer detection algorithms

4.2 Measurements of ice layer density

4.2.1 Development of ice density measurement method

A new laboratory and field-based method was developed to measure the density of ice layers found in seasonal snow, based on volumetric displacement. The basic principle is that when an ice layer sample is submerged in a vessel of liquid, calculating the volume displacement and sample mass will yield an estimate of density. The laboratory and field protocol for measuring the density of ice layers with this method is outlined in Figure 4.1. The mass of a sealed 50 ml centrifuge tube with 2.5 ml graduations containing white spirit (sometimes termed 'mineral spirits'), was measured with a precision of ± 0.001 g under laboratory conditions before entering the field. White spirit is immiscible with water and has a low freezing point (-70°C), which means it can be used at temperatures < 0°C eliminating potential sample melt. White spirit also has a low density (650 kg m^{-3}), making it likely that the ice sample would sink and be completely submerged. In the

field the centrifuge tube was held by a fixed, levelled, mounting system within the macro setting range of a compact camera. Each camera image was centred on a visible datum on the mounting system to ensure the camera was correctly focused, and that repeat images were consistently made from the same horizontal position. Images were taken before and after each ice sample was submerged as shown in Figure 4.2.

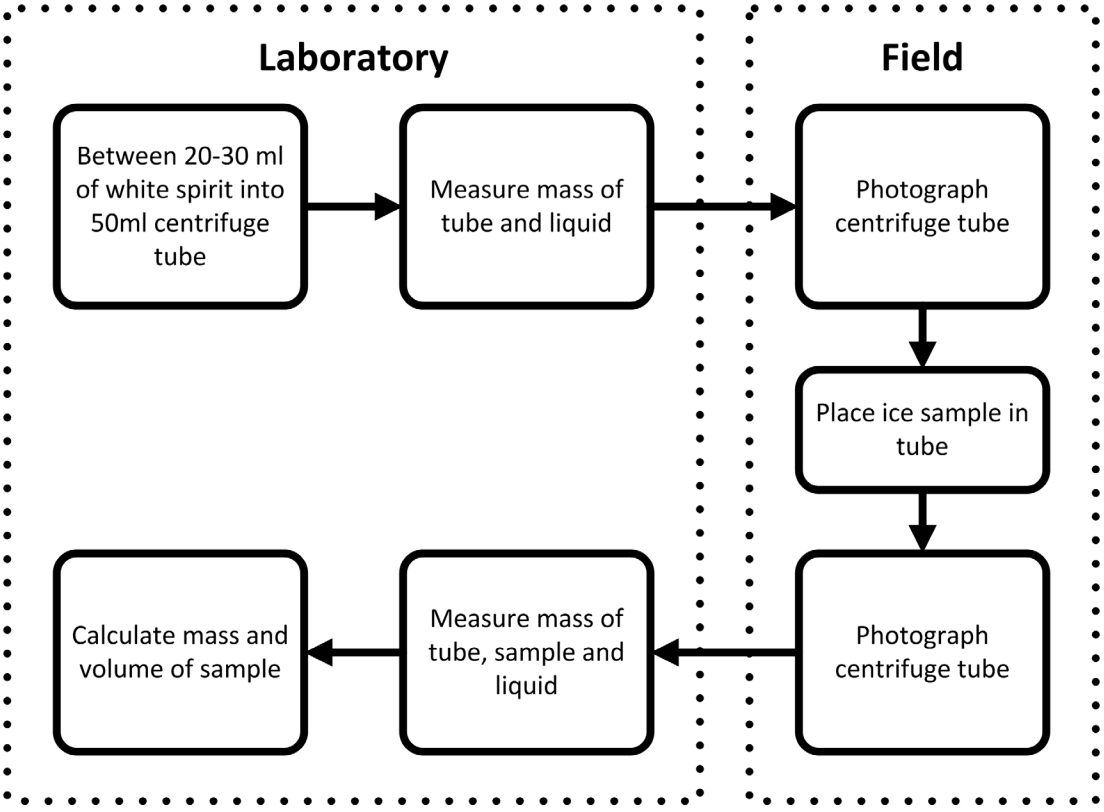

FIGURE 4.1: Flow chart describing the methodology to measure densities of ice samples from a snowpack

In each image three positions were identified during post processing: the liquid level, the graduation above the liquid level and the graduation below the liquid level. Pixel co-ordinates of these positions were taken and as the volume of the graduations on the centrifuge tube were known, and their location in pixels known,

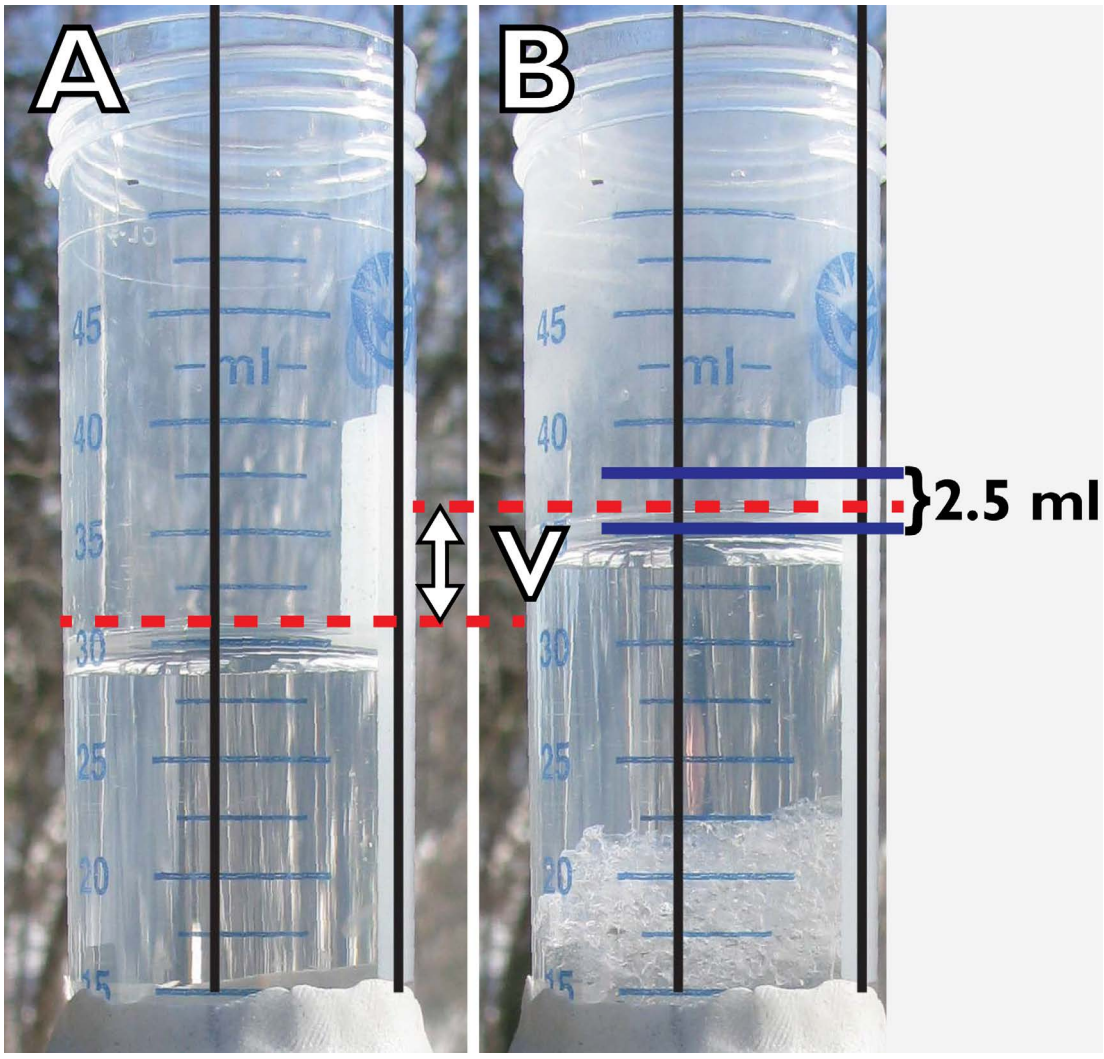

FIGURE 4.2: Example of pair of photos used in calculation of ice sample volume. A, taken before the sample was added and B, taken after. V is equal to the volume of the ice sample. Black lines are guides added to help assess the quality of the photos.

the height of the liquid level in pixels could be translated to a volume in ml at a higher resolution than just the centrifuge tube graduations would allow. The top of the liquid level was located rather than the meniscus for ease of identification; as relative volume change was used no error was introduced. After images were taken, the centrifuge tube containing the sample was sealed and the change in mass was measured on return to the laboratory. Only samples where the liquid

in the tube was level in both images and the sample was short enough to be fully submerged were used in analysis.

4.2.2 Methodological error

Ice layers found in snowpacks are very difficult to accurately and consistently re-create under laboratory conditions. Therefore to assess the accuracy of the ice density measurement technique, ball bearings of known volume were measured. Stainless steel ball bearings were used (manufactured to a diameter of 1 cm $\pm 2.5 \times 10^{-5}$ cm), resulting in a volume range of 0.5236 cm$^3 \pm$ 0.0004 cm^3. The volume of the ball bearings was calculated from photos of the before and after images of 10 ball bearings submerged in the centrifuge tube. The expected total volume of all ball bearings of approximately 5.236 cm^3 is comparable to the mean volume of ice samples collected in the field during pilot studies. Of 134 samples, each consisting of 10 ball bearings, the mean volume was 5.045 cm^3. The volume measurements were normally distributed and an error value based on ± 1 standard deviations was calculated, resulting in a systematic volume measurement error or bias of -0.19 cm^3.

The largest source of error is in reading the height of the liquid in the centrifuge tube from the camera photos. Identifying the precise height of the surface of the liquid between the graduation markings on the cylinder is limited by the quality of the camera focus and resolution of the camera. If the camera focus

is not perfect it is difficult to perfectly locate the height of the liquid, and error and uncertainty occurs. Based on carrying out 10 repeat measurements on 10 centrifuge tube photos we estimate the error to be ± 0.125 cm^3 in each volume measurement photo, equating to a root mean squared error in the measurement of the ice sample volume of ± 0.18 cm^3, as each volume measurement involves reading the volume from two photos.

To calculate the optimum sample volume the number of ball bearings used in each volume measurement was increased from 1 to 24, a volume range of 0.52 cm^3 to 12.57 cm^3. Correlation between standard deviation and sample volume was not statistically significant (confidence >99%), demonstrating that the error in volume measurement was independent of sample volume. Field trials suggested that 10 cm^3 was the maximum sample volume routinely possible to use due to the diameter of the centrifuge tube. Although no minimum sample volume was set, effort was always taken to obtain the largest possible.

To estimate the potential impact of the uncertainty in volume measurement on samples taken in the field, the random (± 0.18 cm^3) volume measurement error from the ball bearing experiment was applied to a theoretical ice sample of volume 4.89 cm^3 and mass 4.53 g (equating to a density of 916 kg m^{-3}). This volume error from the ball bearing experiment translated into an observed volume range of 4.53 - 4.89 cm^3 (i.e. 4.71 cm$^3 \pm 0.18$ cm^3). Assuming no error in the balance (precision of ± 0.001 g), the upper density value (minimum volume) was 951 kg m^{-3} and the lower density value (maximum volume) was 881 kg m^{-3},

representing an uncertainty in density of ±35 kg m^{-3} or 4%. The impact of the error was estimated to be low enough to justifying the practical application of this technique.

4.2.3 Field Measurements

4.2.3.1 Ice layer measurements

During the winter of 2013, ice layer density measurements were collected at three sites in Canada: North Bay, Ontario (46.33°N, 79.31°W) between 8-9 February, CARE, Egbert, Ontario (44.23°N, 79.78°W) on 25 February, and Trail Valley Creek, Inuvik, North West Territories (68.72°N, 133.16°W) on 9 April.

In North Bay, information on the snow stratigraphy, density and the mean maximal extent of individual snow grains was collected in a woodland clearing. Ground based radiometers were used to collect brightness temperatures at this site. An artificial ice layer was created on the surface of the snowpack and compared with naturally formed ice layers. Artificial ice layers have been created in previous work (Montpetit et al., 2012) so it is important to know if their characteristics differ from naturally occurring ice layers. To create the layer a very thin top layer of undulating recent snow (less than 6 hours old) was swept from the snowpack to expose a melt crust below, this was done to maintain an ice layer of even thickness across the site. After the removal of recent snow, water was sprayed onto the snowpack to create a surface ice layer (air temperatures were approximately

-20°C). A natural ice layer covering the entire clearing was also present lower within the snowpack (formed by 2 mm of rain on 30 January). Density, bubble diameter, and thickness measurements of both natural and artificial ice layers were made; whenever bubbles were visible their diameters were measured using a field microscope and snow grain card, a resolution of 0.1 mm was possible with the field microscope. Very small bubbles, with a diameter of < 0.1 mm were recorded as being visible although a diameter could not be applied to them. Layer thickness was measured to a resolution of 1 mm for each sample. 15 density measurements were made of the natural and 15 of the artificial ice layer.

At CARE, measurements were conducted in an open, grass-covered field. A spatially continuous ice layer formed over an area of at least 200×100 m in the 10 cm deep snowpack as a result of above-freezing daytime temperatures for a period of 4 days prior to measurement; ice layer thickness and densities were measured in the same manner as in North Bay, 29 measurements of ice density and thickness were made.

In Inuvik, water was sprayed onto a 30 cm tundra snowpack when air temperatures were approximately -25°C to form an artificial ice layer on the surface of the snowpack as no natural ice layer was present. Water was sprayed over an area of 1 m^2, concentrating the spraying towards one edge, creating an ice thickness gradient that allowed 28 measurements of ice layer density across a range of ice layer thicknesses.

4.2.3.2 Brightness Temperature observations

Brightness temperatures were measured at 19 and 37 GHz using portable surface-based microwave radiometers (dual polarisation, $\approx$ 1.5 m above the snow, 52.5° incidence angle, sampled at a 1 second integration time and averaged over 3 minutes) at the North Bay field site. Radiometers were calibrated using a two-point procedure, before and after field measurements, using a microwave absorber at ambient temperatures (warm target) and another cooled by liquid nitrogen (cold target) (Solheim, 1993). A non-linear iterative procedure was used to account for sensor drift between calibrations before and after field measurements; coefficients for converting target, load and noise diode voltages into brightness temperatures were calculated. As a result, brightness temperature measurements were produced to an accuracy of <2.0 K (Derksen et al., 2012a). After brightness temperatures were recorded, a snow pit was excavated in the radiometer footprint to measure a vertical profile of snow stratigraphy, temperature, grain diameter (mean maximal diameter) and density.

4.3 Results: Ice layer measurements

4.3.1 Ice layer bubble size and thickness

Table 4.1 summarises the measurement of ice layer thickness and bubble size. In some cases bubbles were visible in the ice layer, but were not large enough

to be measured using the field microscope. These were noted as < 0.1 mm in Table 4.1. For the purpose of calculating the mean and standard deviation of the bubble distribution a value of 0.05 mm was applied to these bubbles. There was no correlation between ice layer thickness and bubble diameter.

TABLE 4.1: Measurements of ice layer bubble size and thickness (all sizes in mm)

		Bubble Diameter				Layer Thickness		
	Type	n	n < 0.1	Mean	SD	n	Mean	SD
CARE	Natural	0	-	-	-	29	8	0.6
North Bay	Natural	14	4	0.16	0.12	15	3	0.6
	Artificial	12	6	0.08	0.03	15	5	0.9
Inuvik	Artificial	0	-	-	-	28	2	0.5
Overall	-	26	10	0.12	0.1	86	5	2.7

4.3.2 Ice layer density

Mass and volume measurements were made of 86 samples of ice layers and are summarised in Table 4.2 and Figure 4.3. The mean sample volume was 6.4 cm^3 meaning the random error on the density measurements was $\pm 18 kgm^{-3}$. Ice layer densities varied between 841 and 980 kg m^{-3}, with an overall mean of 909 kg m^{-3} and standard deviation of 23 kg m^{-3}. Natural ice layers were on average less dense than artificial ones although the difference was within the methodological error.

TABLE 4.2: Ice layer density measurements, (all values have been corrected to account for the measured $-0.19 cm^3$ bias in volume)

Site	n	Mean (kg m^{-3})	SD (kg m^{-3})
CARE	29	906	17
North Bay - Natural	15	890	21
North Bay - Artificial	15	921	18
Inuvik	28	915	26

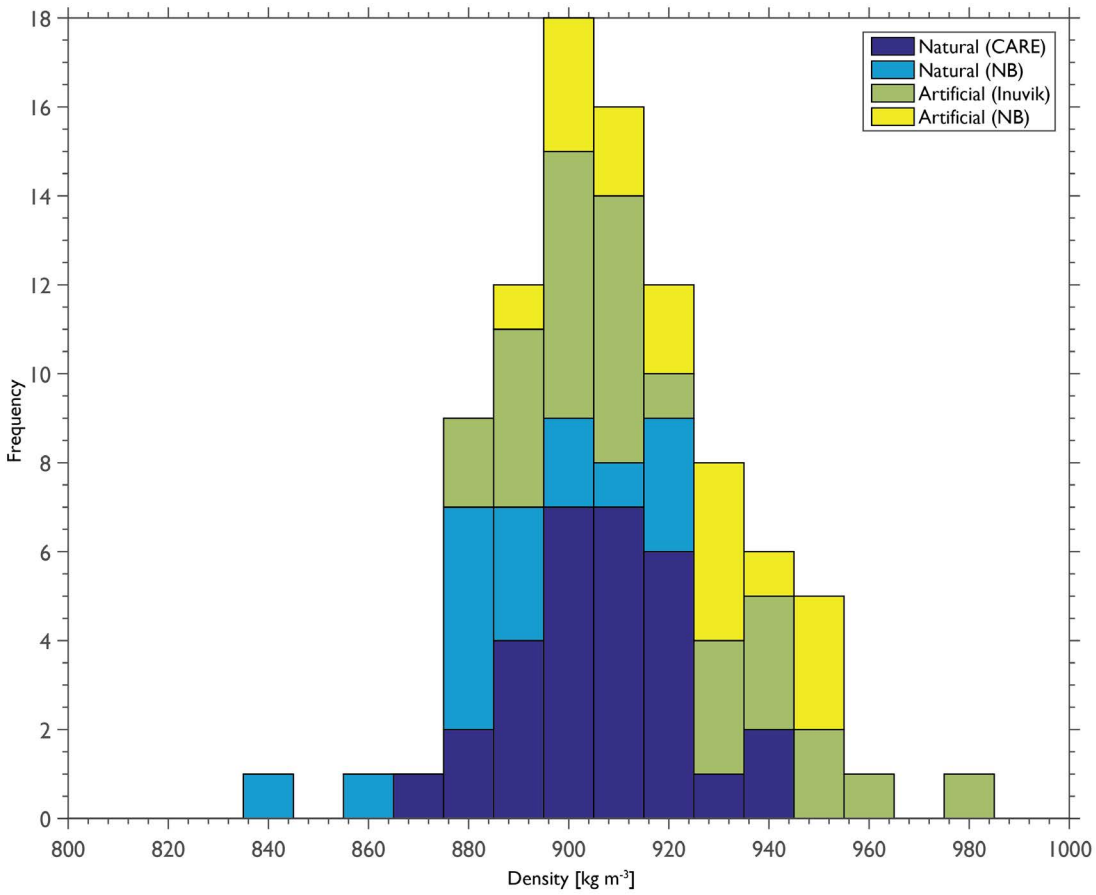

FIGURE 4.3: Summary of ice layer density measurements. Stacked histogram showing frequency of each density measurement, colours show distribution of artificial and natural ice layers across multiple sites

4.3.3 Error in measured density

Three sources of error were identified, the systematic error that exists in the method used to measure the volume of the ice samples (and would apply to any object measured using this method) which was described in the methodological error section, the random error in the method and the error from sample porosity, (which applies only to the measurement of ice layer density using the submersion method). In this section we will quantitatively assess the impact these sources of error on the measurements of ice layer density.

The measured ice layers had a closed porosity, where the layers contained bubbles but they were not connected in a porous structure. However, due to the presence of bubbles in the ice layers some increase in porosity would occur when the ice layer was broken and placed in the centrifuge tube, this is called the effective porosity.

To quantitatively evaluate the effect of effective porosity on the ice layer density measurements, the ice layer, and the bubbles within it were numerically modelled. The ice layer was represented using spheres, representing air bubbles scattered randomly within an ice sample of size x, y, z and density d.

We randomly placed spheres within the x, y, z co-ordinate system without any overlap. The size of the spheres was determined by taking a random sample from a normal distribution of bubble sizes based on a given mean and standard deviation. A sphere size was chosen from the random sample and located at random within the x, y, z axes, if that sphere in that location overlapped another sphere then the location was changed. If after 1000 attempts a location for the sphere could not be found its radius was changed to another random sample from the normal distribution and the process repeated. After each sphere was placed, the total volume of all the spheres and the density of the ice sample was calculated. Spheres were added to the sample until the desired density was reached.

Slices were taken through the ice sample and the volume of the spheres that would be open to the surface (and therefore allow liquid to penetrate the ice surface)

was calculated. For instance, if the slice went through a sphere at exactly the halfway point, half of the volume of that sphere would be added to the porosity value for that sample. This approach is illustrated schematically in Figure 4.4. This method assumes that the ice layer is a solid ice layer containing bubbles rather than a granular snow-like structure. Great care was taken to only measure and include impermeable layers which are more likely to exhibit this structure.

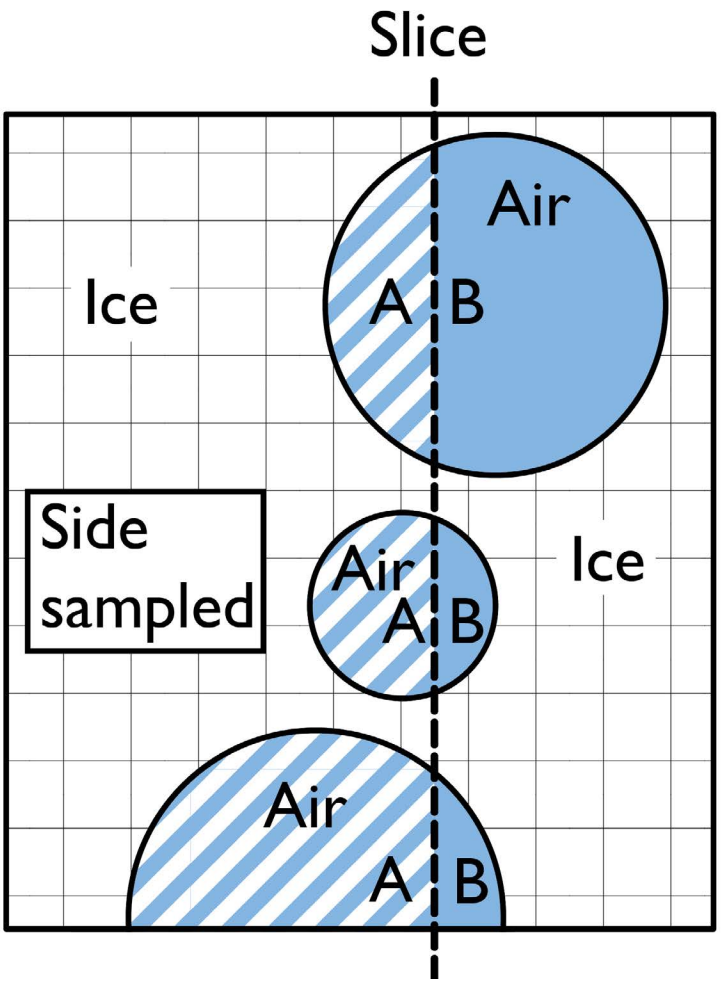

FIGURE 4.4: schematic representation of slicing technique to measure porosity. Air bubbles (shaded in blue) are shown in an ice sample, the theoretical slice was made at the location of the dashed line. The left hand side was chosen as the side to be sampled, and so all of the striped areas marked 'A' were calculated and summed to calculate the overall porosity of the sample.

The mean and standard deviation of bubble diameter measurements were used to create the distribution of bubbles in the ice layer. Examples of the ice layers with bubbles distributed in them are shown in Figure 4.5.

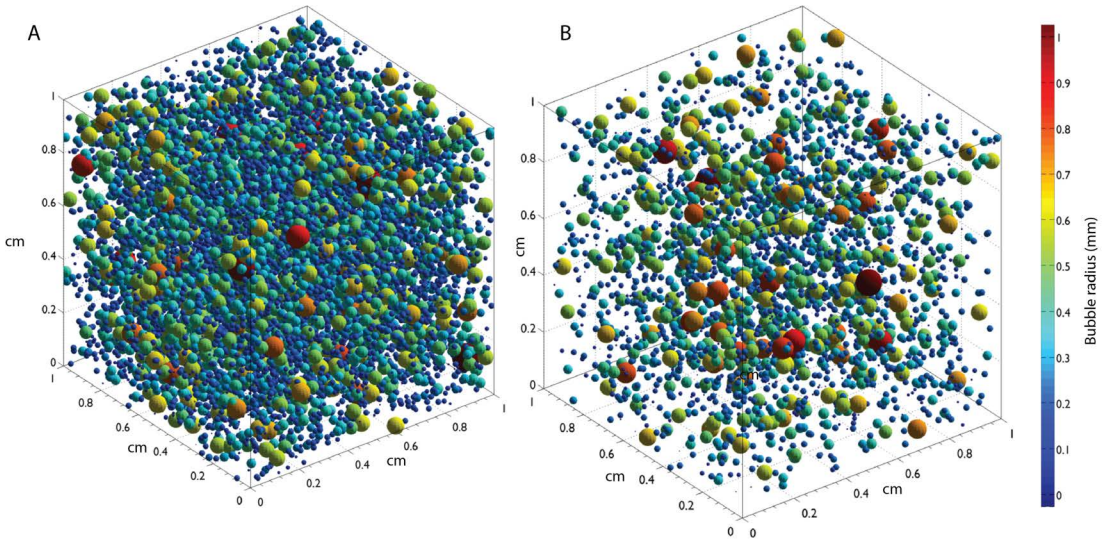

FIGURE 4.5: Examples of the numerical representation of the ice layers used to investigate porosity, a) shows a sample with simulated density of 800 kg m^{-3} and b) shows a sample with density 885 kg m^{-3}

For a theoretical ice sample of size $1 \times 1 \times 1$ cm the sample density was increased in increments of 0.01 kg m^{-3}, and porosity was measured through the sample by taking slices at 0.1 cm intervals. The relationship between effective porosity and density (d) for this bubble and sample size is linear, and the effective porosity (p) in cm^3 is found using:

$$p = 0.000078d + 0.72 \tag{4.1}$$

this assumes the same porosity on all edges of the ice sample (where the sample was broken). The bubble diameter mean and standard deviation were taken as the overall values from all samples. To calculate the impact of this porosity on our samples we assumed a sample width of 2 cm (the width of the centrifuge tube), we measured the sample thickness and we measured the volume (with known methodological error) so we were able to estimate the maximum and minimum dimensions of each sample. By using the relationship in Equation 4.1 we estimated the porosity of each sample based on the measured density. Sample porosities ranged from 6.5×10^{-5} to 0.0001 cm^3. The mean increase from using either the maximum or minimum value for density in the porosity calculations was 1.42×10^{-6} cm^3.

The maximum random error (± 0.18 cm^3), the volume measurement bias (-0.19 cm^3) and the porosity correction were applied to each of the volume measurements and the maximum range of density calculated for each sample. Due to the very high densities of the samples porosity was negligible (less than 0.0001 cm^3). Overall the measurements of ice layer density (909 ± 18 kg m^{-3}) were not significantly different to measurements of pure ice.

4.4 Simulation of brightness temperatures using measured ice density

Objective measurements of ice layer density with fully characterised uncertainty (see previous section) were applied to the representations of ice layers in snow emission models. In this section we: 1) outline how ice layers are represented in snow emission models and how the models were initialised, 2) describe how we initialised the snow emission models and, 3) present the impact of measured ice layer densities on simulation bias of brightness temperatures, and the impact on the polarisation ratio method of detecting ice layers (Grenfell and Putkonen, 2008).

4.4.1 Model Initialisation

4.4.1.1 DMRT-ML

The vertical profile of snow properties measured at North Bay (Figure 4.6) was used to initialise both snow emission model simulations. The two layers directly beneath the artificial surface crust were merged together for model initialisation as an exact lower boundary was not evident in the stratigraphy; an average grain diameter of both layers was used (0.95 mm).

The measured soil temperature was -2°C and an assumed soil permittivity value of 6-j was used (Zhang et al., 2003). The n-HUT soil model was used in the DMRT-ML model runs (as in Roy et al. (2013)). The bubble diameter in ice layers was set to 0.12 mm, as 0.12 mm was the mean bubble size recorded across all ice layer samples. In later sections, the properties of the ice layers were scaled to investigate the sensitivity of model output to specific parameters based on our observations. Model initialisation values are summarised in Table 4.3.

Table 4.3: Summary of range of input and initialisation parameters across all model runs

		Measured				Modelled				
Type	T (cm)	D^a	$G_d{}^b$	$B_d{}^c$	Temp(°C)	D	G_d	B_d	$l_c{}^d$	P
Ice	0.5	909	-	0.2	-13	500 - 916	-	0.2 - 0.5	0.67	-
Snow	17.75	330	0.95	-	-7	330	0.95	-	0.17	-
Ice	0.25	909	-	0.2	-1	500 - 916	-	0.2 - 0.5	0.67	-
Snow	2.5	340	1.35	-	-1	340	1.35	-	0.20	-
Ice	1	909	-	0.2	-0.73	500 - 916	-	0.2 - 0.5	0.67	-
Soil	-	-	-	-	-2	-	-	-	-	6-j

[a]Density (kg m^{-3})
[b]Grain Diameter (mm)
[c]Bubble Diameter (mm)
[d]Correlation Length (mm)

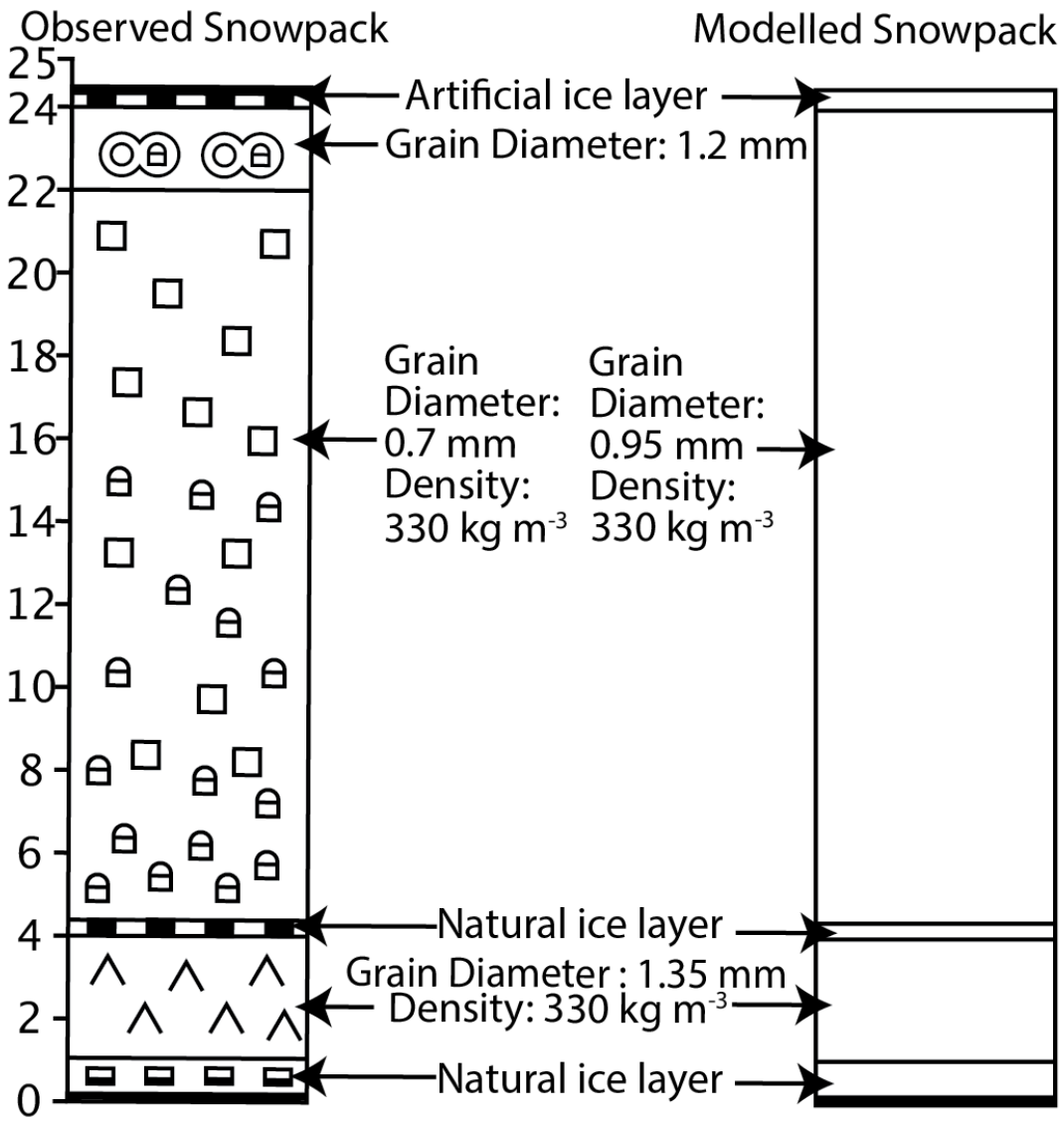

FIGURE 4.6: Observed and modelled snowpack at North Bay, explanation of snow symbols in figure 3.15

4.4.1.2 MEMLS

MEMLS was initialised using the same snowpack stratigraphy as DMRT-ML (as shown in Figure 4.6). Density and temperature parameters were directly transferable between models. MEMLS does not use the grain size parameter to define snow microstructure but rather correlation length. Initialisation values are

shown in Table 4.3. For snow layers, the grain size of the layer was converted into a correlation length using the relationship in Equation 4.2 presented in Durand et al. (2008)

$$p_{ex} = \begin{cases} 0.18 + 0.09 \ln D_{max}, & v > 0.2 \text{ and } D_{max} > 0.125 \text{ mm} \\ p_0, & \text{otherwise} \end{cases} \tag{4.2}$$

where p_{ex} is the exponential correlation length, D_{max} is the largest measured extension of the snow grain, and v is the volume fraction (snow density divided by density of ice). In the case of ice layers a correlation length of 0.71 mm was used as this value is suggested as a suitable value for ice crusts in Matzler and Wiesmann (1999).

4.5 Results: Brightness temperature simulations

This section is split into three parts: firstly a sensitivity analysis was conducted on the parameters used to describe ice layers in both DMRT-ML and MEMLS, secondly the models were tuned to find the optimum ice layer density to minimise bias and, thirdly the impact of ice layer density on the polarisation and gradient ratios used in ice layer detection was investigated.

4.5.1 Model Sensitivity to ice layer properties

The models were initialised using the snowpack observed at the North Bay field site and described in section 4.4.1. Each snowpack input parameter was varied individually between a range of values typically found in shallow snowpacks. The percentage change in the model output was recorded for each iteration. The results from the MEMLS and DMRT-ML models are discussed below.

4.5.1.1 MEMLS

MEMLS has no ice layer specific parameters, it describes an ice layer using the same parameters as are used to describe any snow layer. These are: density, thickness, temperature and correlation length, the sensitivity to these parameters is shown in Figure 4.7.

Ice layer density was varied between 500 and 900 kg m^{-3}. Between 500 and 600 kg m^{-3} jumps are visible in the sensitivity plot. These jumps are caused by coherence effects as the ice layer switches from a coherent to incoherent layer, this occurs at a slightly different density for both 19GHz and 37GHz which explains the offset between the two. H-Pol is more sensitive to ice layer density than V-pol. Coherence is dependent on layer thickness and density, and this is demonstrated again in the rapid changes in sensitivity which are visible in the ice layer thickness sensitivity plot between 0.01 and 5 mm. For 37 GHz both H-pol and V-pol demonstrate virtually the same sensitivity profile to ice layer thickness, with

only a small difference when the layers are incoherent at very low thicknesses. Correlation length and temperature both exhibit much lower sensitivity compared to ice density or ice layer thickness.

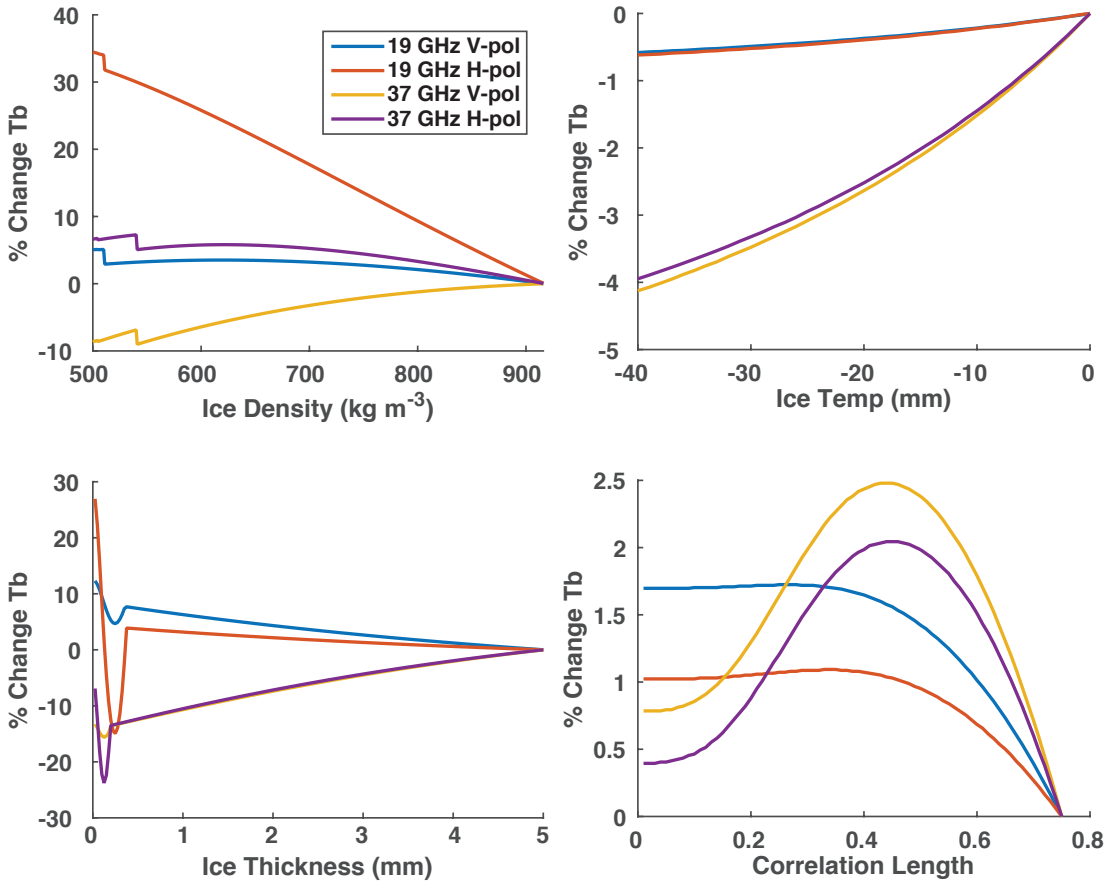

FIGURE 4.7: Sensitivity of MEMLS to ice layer properties

4.5.1.2 DMRT-ML

Unlike MEMLS, DMRT-ML uses an ice layer specific parameter, bubble radius, to describe the microstructure of the ice layer, it does not use a grain size parameter for ice layers. In addition to the bubble radius parameter ice layers are assigned a temperature, density and thickness, the same parameters which are used for

snow layers. The model sensitivity to these parameters is shown in Figure 4.8. Sensitivity to ice layer density was of a similar magnitude to MEMLS, although different in character. DMRT-ML does not include simulation of coherence effects, and this leads to a more linear model sensitivity to this parameter, with the jumps that were exhibited in the MEMLS sensitivity curve absent for DMRT-ML. DM-ML is more sensitive to changes in ice layer temperature than MEMLS, and has similar overall sensitivity to layer thickness at very low thicknesses. However, for thicker layers, changes in layer thickness had much less effect on DMRT-ML than MEMLS. The bubble radius parameter had a very low sensitivity.

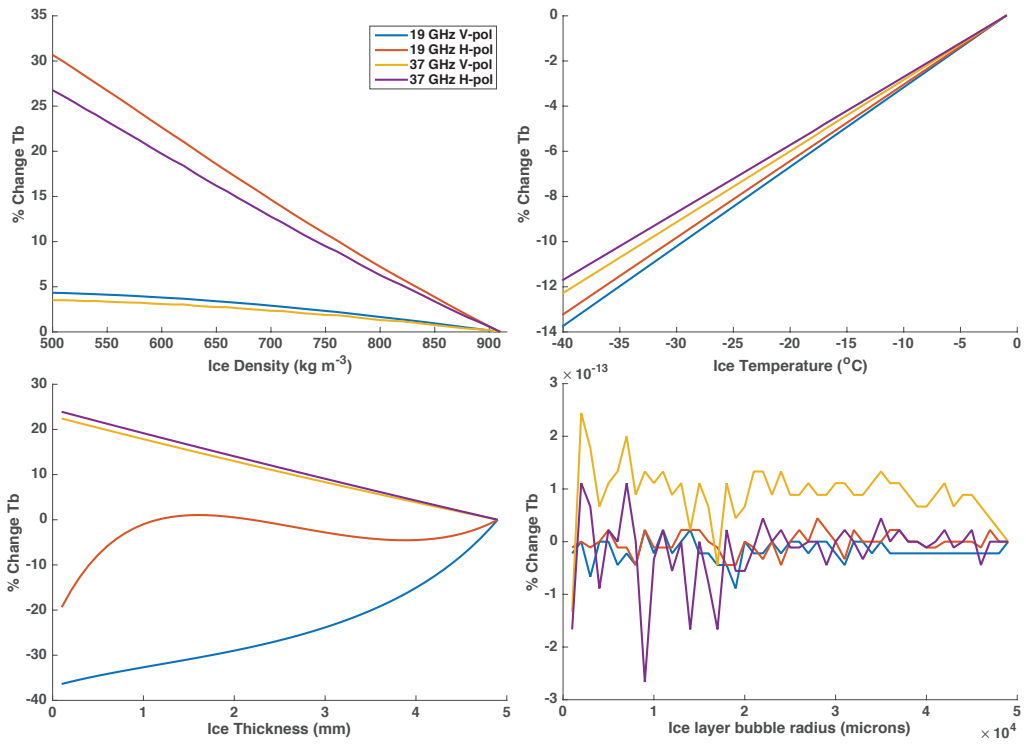

FIGURE 4.8: Sensitivity of DMRT-ML to ice layer properties

4.5.2 Model optimisation using ice layer density

The results of the sensitivity analysis in section 4.5.1 show that V-pol exhibited limited sensitivity to ice layer density compared to H-pol. Based on this the models were tuned to minimise bias for the V-pol simulations. The observed brightness temperatures are shown in Table 4.4 and have an accuracy of ± 2K (Asmus and Grant, 1999).

Table 4.4: Observed brightness temperatures

37 V	37 H	19 V	19 H
208	203	250	232

To minimise bias for V-pol simulations the microstructure parameter for both DMRT-ML (Grainsize) and MEMLS (correlation length) was tuned using a scaling factor. The microstructure parameter was chosen as snow and ice microstructure is difficult to quantify using a field microscope (as was used here) and so there is some inherent uncertainty in the grain size and converted correlations lengths measured in the field. For DMRT-ML the mean bias was zero when the scaling factor was 2.252 and for MEMLS the mean bias was zero when the scaling factor was 0.95.

After applying the optimum scaling factor to the model initialisation data in order to minimise bias for the V-pol simulations the ice layer density at which H-pol simulation bias was minimised was calculated. Ice layer density was varied from 500 kg m^{-3} to 916 kg m^{-3} and model bias was minimised at 497 kg m^{-3} for DMRT-ML and 504 kg m^{-3} for MEMLS, results from the optimisations are

shown in figures 4.10 (DMRT-ML) and 4.9 (MEMLS). For DMRT-ML mean bias across both frequencies and polarisations was $-7.5K$ and for MEMLS mean bias was $-7.7K$.

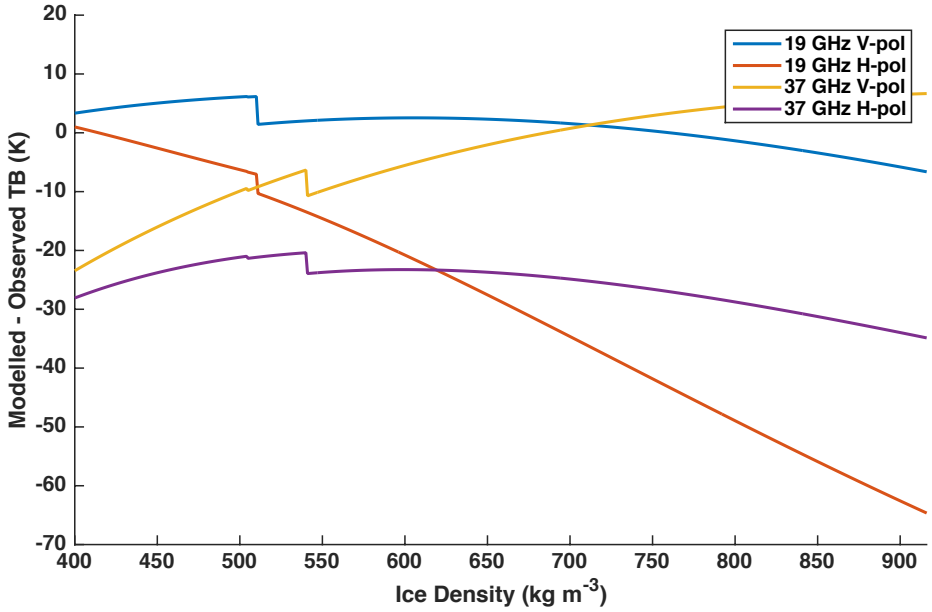

FIGURE 4.9: Difference between modelled and observed brightness temperatures with changing density for MEMLS

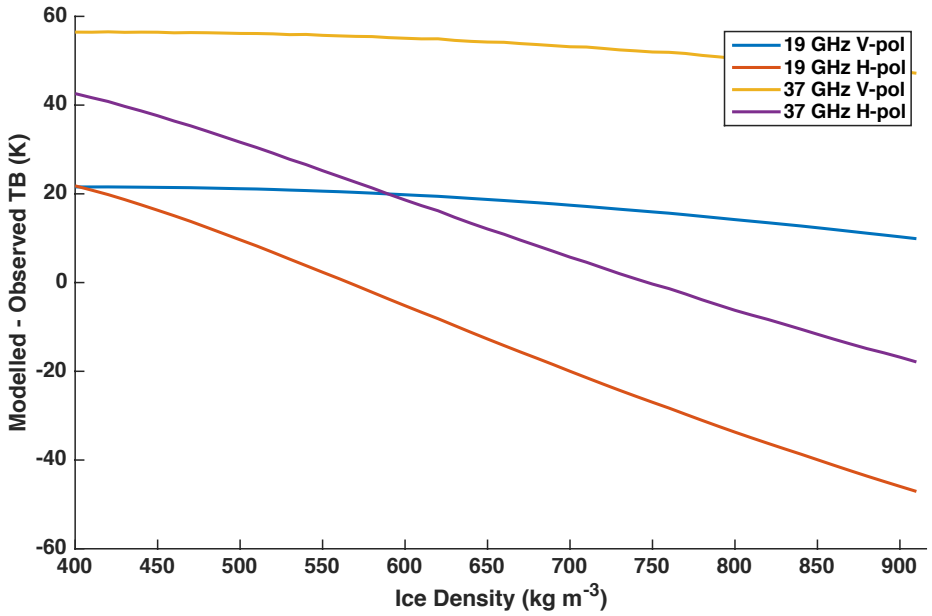

FIGURE 4.10: Difference between modelled and observed brightness temperatures with changing density for DMRT-ML

4.5.3 Effect of ice layer density on polarisation and gradient ratios

Figures 4.11 and 4.12 show the impact of varying ice layer density (between 500 kg m^{-3} and 916 kg m^{-3}) on the gradient ratio

$$GR(37,19) = \frac{[T_B(p, 37\text{GHz}) - T_B(p, 19\text{GHz})]}{[T_B(p, 37\text{GHz}) + T_B(p, 19\text{GHz})]} \tag{4.3}$$

and polarisation ratio

$$PR(v) = \frac{[T_B(\text{V-Pol}, v) - T_B(\text{H-Pol}, v)]}{[T_B(\text{V-Pol}, v) + T_B(\text{H-Pol}, v)]} \tag{4.4}$$

used in the ice layer and rain-on-snow detection algorithm presented by Grenfell and Putkonen (2008). The gradient ratio from the observed brightness temperatures was -0.0917 for V-pol and -0.07 for H-Pol and was not well simulated by either model. MEMLS' simulation of gradient ratio had far higher sensitivity to ice layer density than DMRT-ML's.

The observed polarisation ratio for 19 GHz was 0.0373, both MEMLS's and DMRT-ML's simulations of polarisation ratio were similarly sensitive to changes in ice density. The biases in the simulated polarisation and gradient ratios were minimised when a low, physically unrealistic, ice layer density was used.

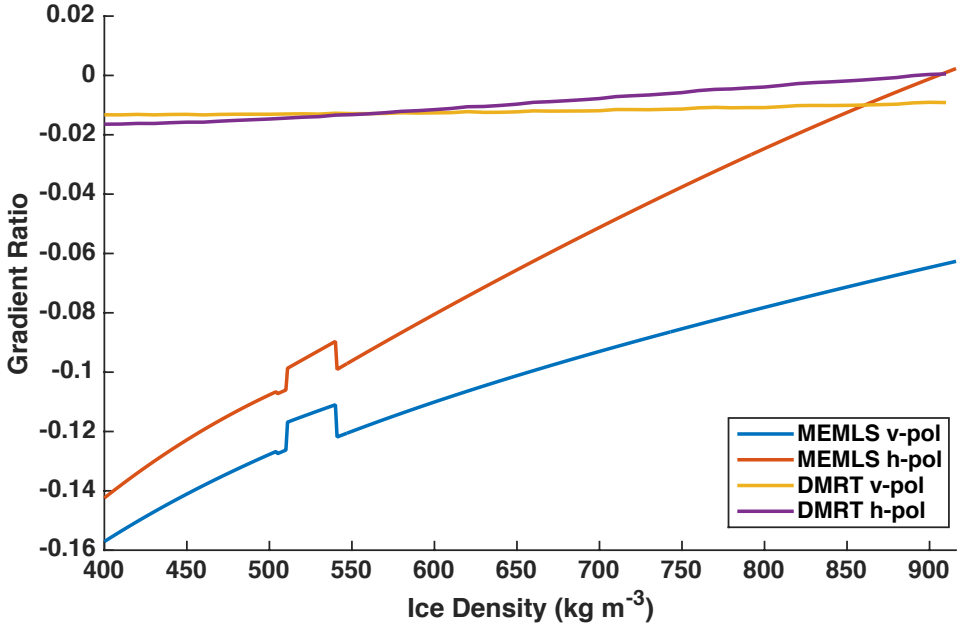

FIGURE 4.11: Effect of density on gradient ratio

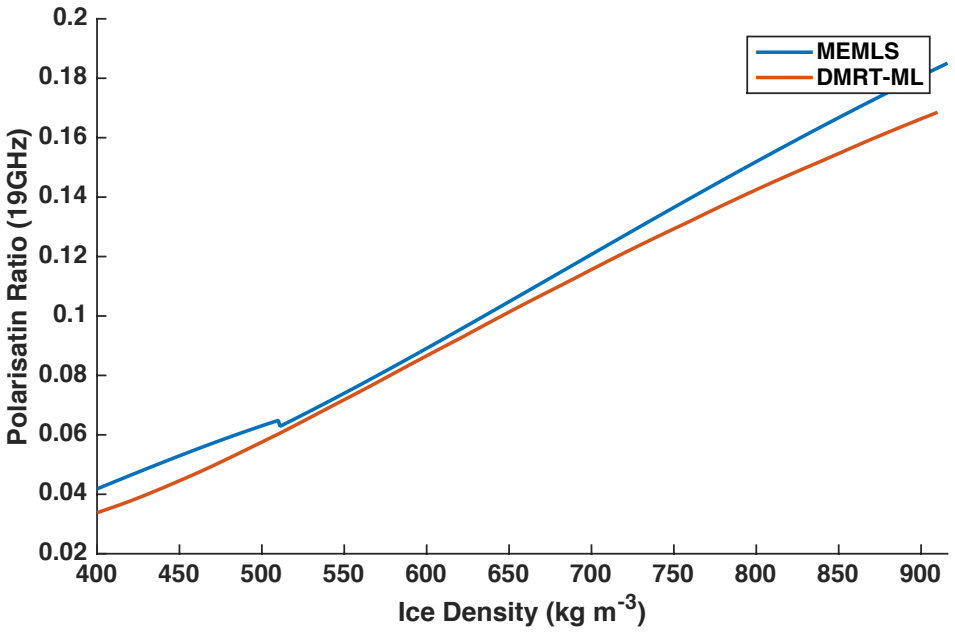

FIGURE 4.12: Effect of density on polarisation ratio

4.6 Discussion and Conclusions

A new laboratory and field protocol was used to produce direct estimates of ice layer density (including uncertainty). Measurements of natural and artificially made ice layers produced an average density of 909 ± 18 kg m^{-3}. The uncertainty terms are related to systematic bias in the method used to measure the volume of the ice samples, and the effective porosity of ice layers. Our measured density values are higher than those in Marsh (1984) (mean 800 kg m^{-3}), and Pfeffer and Humphrey (1996) (400 kg m^{-3} to 800 kg m^{-3}). It is unclear whether previous studies assessed and quantified the density of ice layers that were permeable and porous, including thin, non-continuous ice layers, which may explain the density differences.

Characterisation of ice layer properties is of fundamental importance for the application of snow emission models. When used in two different emission models (MEMLS and DMRT-ML) our ice layer measurements show that physically unrealistic ice layer density values are necessary to optimise agreement between simulations and observations. For the North Bay snowpack presented in this study, bias was minimised when an ice layer density of between 497 kg m^{-3} and 504 kg m^{-3} was used. This is consistent with Durand et al. (2008) who used ice layer densities of 500 kg m^{-3} to improve agreement between simulations and microwave observations. The soil beneath the snowpack also has an impact on

the accuracy of brightness temperature simulations, although it has not been included in this study.

Calculations of absorption occurring in a planar ice layer are well established, modelling bubbly ice has produced good results in other scenarios (Dupont et al., 2014) and changing the bubble diameter within the ice layer (in DMRT-ML) has negligible impact on simulation bias. Consequently, this suggests simulation bias does not result from radiative transfer within the ice layer, but rather at layer boundaries where a high dielectric gradient leads to increased uncertainty in simulated brightness temperatures. Montpetit et al. (2012) hypothesises that MEMLS will better cope with these kinds of simulations as it models coherence effects, however, in this case MEMLS has not performed better than DMRT-ML (which does not include coherence effects).

As the predicted frequency of winter melt events increases, so will the need to detect melt and rain on snow events (Montpetit et al., 2012). One possible method of doing so would be to detect the existence of ice layers (Grenfell and Putkonen, 2008). We have also shown that ice layer density strongly impacts the polarisation ratio used in ice layer detection algorithms (Figure 4.12). Future work in this area should account for density if snow emission models are used. Currently snow emission models are unable to correctly simulate ice layers when physically realistic values of ice layer density are used. Future work is necessary, therefore, to address the disconnect between observed ice layer properties and the necessary ice layer inputs to optimise emission model performance.

Chapter 5

Snow Trenches in Inuvik

5.1 Introduction

In this chapter an array of snow trenches, varying in length from 5 to 50 m, is used to capture variability within snowpack stratigraphy, layer boundary roughness and simulated brightness temperatures over these scales. Subnivean topography is far rougher and more undulating than the snow surface, we hypothesise that the roughness of snow layers decreases with distance away from the ground, a relationship would be useful for applying snow pack and snow emission models in two dimensions.

5.2 Aims and Objectives

The research question of this chapter is: "What is the impact of stratigraphic variability on spatial distribution of brightness temperatures in a snow covered tundra environment?" This question will be answered by addressing three aims and achieving their associated objectives outlined below each aim.

- Aim 1 : To quantify layer thickness and boundary roughness variability
    1. To test our hypothesis that snow layer boundary roughness is a function of the proportional height of the boundary in the snowpack and ground roughness
    2. To quantify the spatial variation in layer thickness in an Arctic tundra watershed
- Aim 2 : To quantifying the impact of spatial variability of stratigraphy on Snow Microwave Emission Models
    1. To simulate brightness temperatures continuously along 5 and 50 metre transects taken from Arctic tundra snowpacks
    2. To compare simulated brightness temperatures at different spatial scales and at different locations within one snowpack.
- Aim 3 : To determine the minimum subset size in each trench location required to calculate the mean brightness temperature for that trench.

5.3 Field Methods

The data requirements for this chapter were to have a large number of trenches, long enough to capture local variability in snowpack stratigraphy, distributed over a single land surface type with in situ measurements to enable snow emission models to be run at each location. The general trench sampling method used in Chapter 3 was also used to collect data for this chapter. Some modifications were applied, which are described in Section 5.3.2.1. The Arctic tundra location of Trail Valley Creek in Inuvik NWT, Canada was chosen to be the location of the snow trenches.

5.3.1 Field Site

To achieve the research aims of this work a large number of snow trenches was required on one land cover type and in one area. The location of Trail Valley Creek in Inuvik NWT, Canada was chosen for this as it provided a small watershed with large areas of flat tundra suitable to the excavation of many trenches quickly and efficiently.

Figure 5.1 shows the location of Trail Valley creek at the margin of the Mackenzie River Delta. Data was collected at the watershed over two periods during March and April 2013.

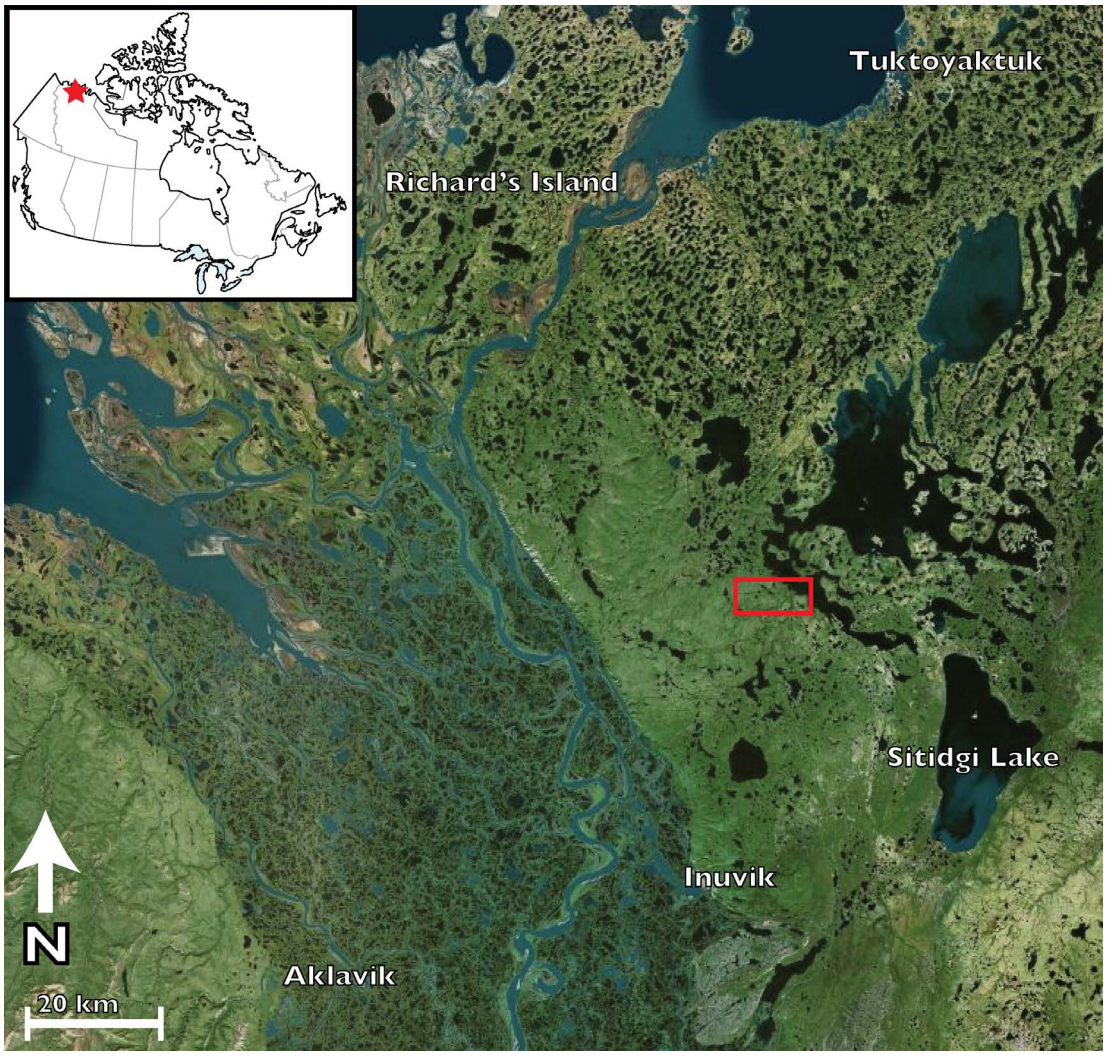

FIGURE 5.1: Landsat image and map showing the location of Trail Valley Creek to the East of the Mackenzie Delta in NWT.

Trail Valley creek experiences a climate typical of the Canadian Arctic, winter temperatures typically range from -35 to -15 C and high wind speeds of 10 to 15 ms^{-1} are regularly experienced throughout the winter (winter meteorological summary shown in Figure 5.2). The tundra is a largely flat undulating surface crossed by gullies and dotted with a vast array of lakes and ponds. During the early season (before December) snow begins to infill the undulations in the tundra and the gullies where the vegetation height is greater (willows as opposed to scrub

on the upland areas). Later in the winter (after March) the bottom of the gullies are filled with snow and only willow and spruce trees protrude from the snow surface.

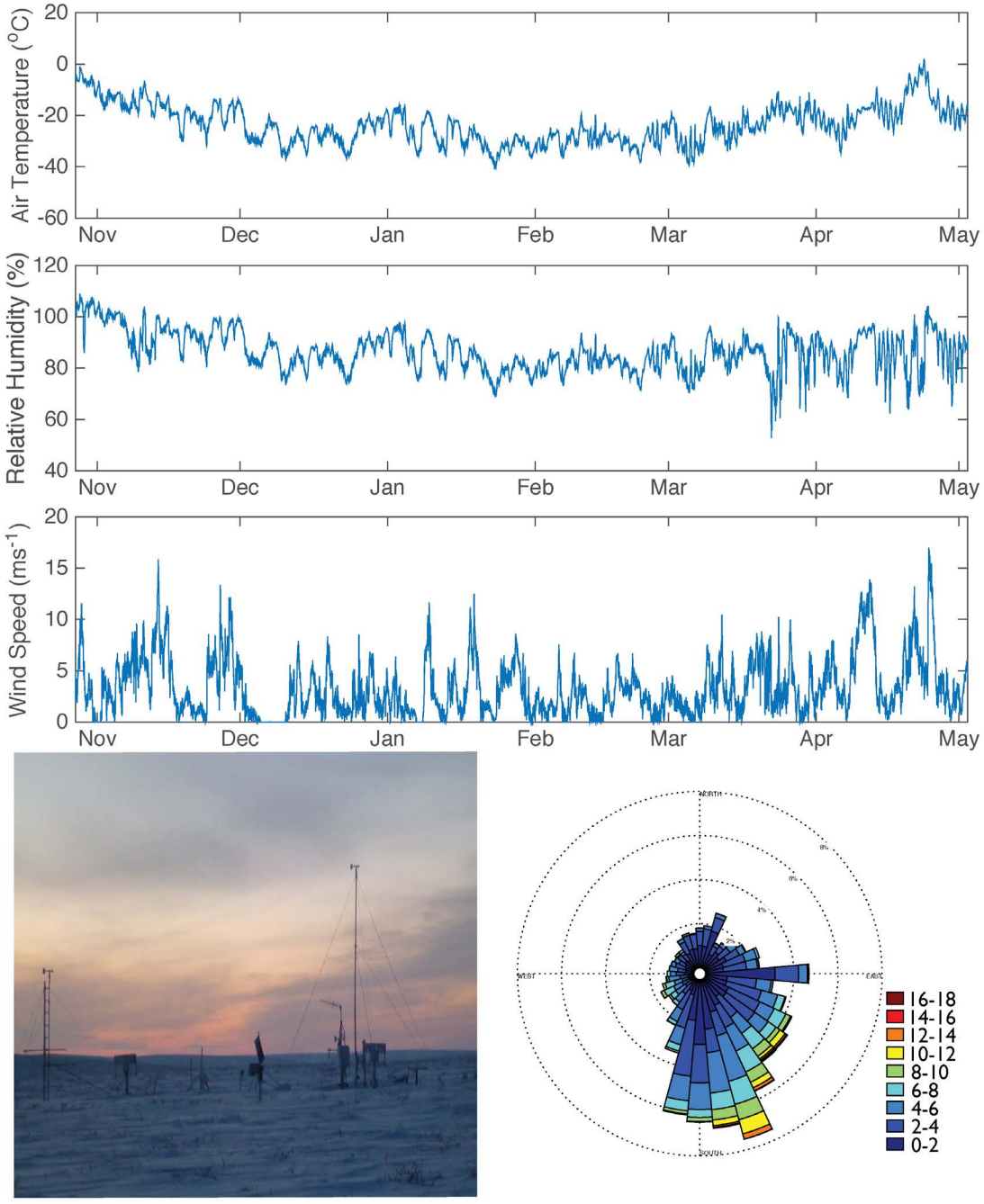

FIGURE 5.2: Meteorological data from Trail Valley Creek collected over the study period in winter 2012-2013 from the main tundra met site situated on the upland tundra plateau (shown in photo).

5.3.2 Field Measurements

5.3.2.1 Application of NIR trenches to distances >50 m

Snow trenches were excavated and used to obtain a large number of snowpack profiles from each site, allowing snowpack variability to be characterised. In order to ensure that as much variability was recorded at each site as possible trenches of 50 m were used. A 50 m trench was dug using ten 5 m trenches situated next to each other. This process was carried out over multiple days, and each 5 m section processed individually using the methods described in Chapter 3. In order to stitch each 5 m section together horizontal and vertical rulers were attached to a board which was visible at the start and repositioned to appear at the end of each 5 m section (shown in Figure 5.3), as the board was not moved between the start and end of each section it was able to act as a point of reference for the trench sections to be aligned in the NIR trench photographs. The method used to stitch the 5 m sections together is the same as the method used to smooth the artefacts and discontinuities which occured between photographs in a 5 m trench.

FIGURE 5.3: Photo showing collection of snowpack data from Trench 4 in Trail Valley creek

5.3.2.2 Trench measurements

Snow trenches were excavated in March and April, Figure 5.4 shows the locations that the trenches and pits were excavated. In Figure 5.4 land cover classifications (Tundra, shrub and willow, and Forest) were created using a LiDAR derived land surface classification as detailed in Marsh et al. (2010) and this was used to classify the land surface on which the trenches were excavated, in addition to local knowledge about the land surface obtained from members of the team who had visited the field site during snow free times of year.

In the trenches measurements of snowpack properties were made every 5 m. This

equates to one stratigraphic profile for a 5 m trench and 10 for a 50 m trench. The horizontal location of the stratigraphic profile within every 5 m trench was chosen in order to maximise the number of layers that were sampled in the stratigraphic profile. Each profile consisted of a visual grain diameter estimate taken to the nearest 0.1 mm using a field microscope. Measurements were made by the same person in each Trench during the April samples, during March measurements were made by either the April sampler or one additional sampler. At the site of the grain size measurements snow density was also measured, either a 100 cm^3 or a 1000 cm^3 sampler was used to measure a sample of snow which was weighed using a spring balance. Measurements of density were taken through the entire snowpack profile irrespective of layer locations and the height of the density sample was recorded. Snowpack properties were assigned using the method described in Chapter 3. Hardness was measured using manual methods described in the international classification of seasonal snow on the ground and grain type was identified also using the guidelines found in the classification. Specific surface area was measured at every April trench using an IRIS (Gallet et al., 2009), and NIR photography was taken of all trenches, as it was required for the digitisation of the snow layers. Table 5.1 outlines the measurements which were made in the snow pits and snow trenches across the Trail Valley Creek watershed. For logistical reasons manual grain size was not recorded at Trench 8, and IRIS was not used at any of the March Trenches or Trench 6 or 2.

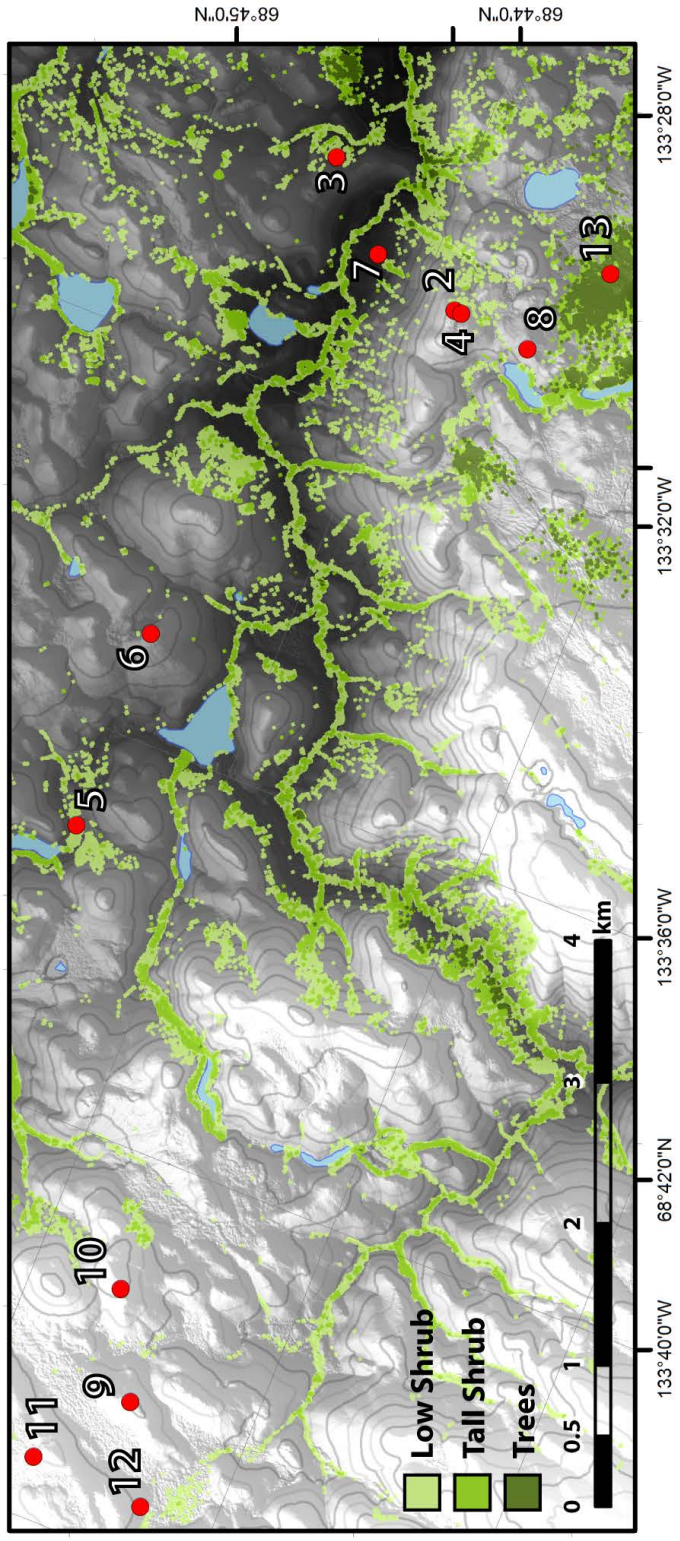

FIGURE 5.4: Locations (red dots) where trenches were dug at the Trail Valley Creek field site. Surface colours indicate land cover type (Blue: water, Dark Green: Forest, Green:Tall shrub/willow, otherwise scrubland. Contours are at 10 m intervals, classification adapted from Marsh et al. (2010)

Table 5.1: Table of all measurements made at trenches their lengths and reference to locations in Figure 5.4

Trench	Landcover Type	Length
2	Tundra	50
3	Tundra	5
4	Tundra	50
5	Willow	5
6	Tundra	5
7	Tundra	5
8	Tundra	5
9	Tundra	5
10	Tundra	5
11	Tundra	5
12	Tundra	5
13	Forest	5

5.4 Results and Analysis

The results and analysis for this chapter are split into three sections determined by the Aims outlined in the first section of the chapter. Analysis has been incorporated with the results and then the results are discussed in the next section

5.4.1 Snowpack characteristics and variability

5.4.1.1 Snowpack variation over 50 m

Two 50 m trenches and a further eleven 5 m trenches were excavated. Not all of these trenches are suitable for analysis. Due to problems with the digital camera auto focus trenches 1 and 3 do not have accurate horizontal positioning of layer properties and scale. While they are useful for some more general applications, they will not be considered here. Trenches 5 and 13 were excavated

on willow and forest landcover types. This means they are particularly useful when examining the differences between landcover types, however, in this chapter only the scrub/low shrub covered tundra landcover type is considered. When exploring the general characteristics of the snowpack over 50 m both trenches 2 and 4 are suitable, however, as trench 2 is the only trench excavated in March, and therefore is likely to have a different structure to the trenches excavated in April it will also not be considered here.

36 layers were identified in Trench 4, the properties of these layers were assigned based on the measurements made in the field at 5 m intervals along the snow trench. Where no measurements were made of a particular layer then properties from a layer with similar proportional height and thickness were used. The general structure of the snowpack was a layer of fresh deposition overlaying a middle section composed of a mixture of wind slab layers of varying thicknesses, grain sizes and types. The bottom layer was depth hoar, which filled the undulations in the ground surface and the areas between vegetation. The depth hoar chains did not extend much into the rest of the snowpack, as a result of this the overall covariance between the depth hoar percentage and snow depth is -0.15 demonstrating that as the depth of the snow increased the depth hoar fraction decreased. It should be noted that many of the middle windslab layers in the snowpack were facetted, but had not metamorphosed to the point where they became cohesive depth hoar chains.

Semivariograms can be used to investigate the spatial variability of snow layers or

snowpack properties over different spatial scales. The semivariance is described as

$$\hat{\gamma}(h) = \frac{1}{2} \cdot \frac{1}{n(h))} \sum_{n(h))}^{i=1} (z(x_i + h) - z(x_i))^2 \tag{5.1}$$

Where z denotes a data value at a particular location, h is the distance between data values, and $n(h)$ is the number of pairs of data values a distance of h apart. In a semivariogram the lag distance (h) is plotted against semivariance. The point that the curve flattens is referred to as the sill. The sill occurs at the point where there is no longer correlation over the lag distance. At this point the property has been, theoretically, completely quantified (Wackernagel, 1995), measurements made past this point no longer provide additional information on spatial variability. The lag distance at which the sill occurs was calculated by fitting a spherical model to the data points as described in Minsasny and McBratney (2005). An example of a spherical fit is shown in Figure 5.5, the purple points are the points from the semivariogram and the blue and orange line shows the fitted model and detected sill.

Figure 5.6 illustrates how variation in the top, middle and bottom snow layers (as defined in the previous section) changes at different spatial scales. The lag distance where the sill is reached is shown in Table 5.2 and varies between 29 and 400 cm for different layers and different trenches. The range at the sill varies independently of type and there is no correlation between trenches.

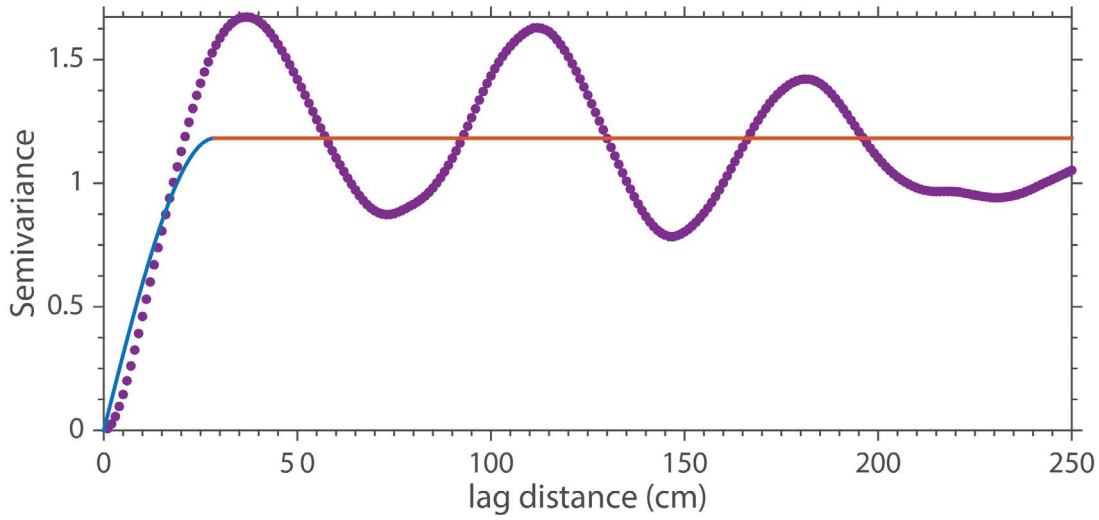

FIGURE 5.5: Example of a spherical model (line) fitted to the semivariogram data points (purple), the sill is highlighted in orange

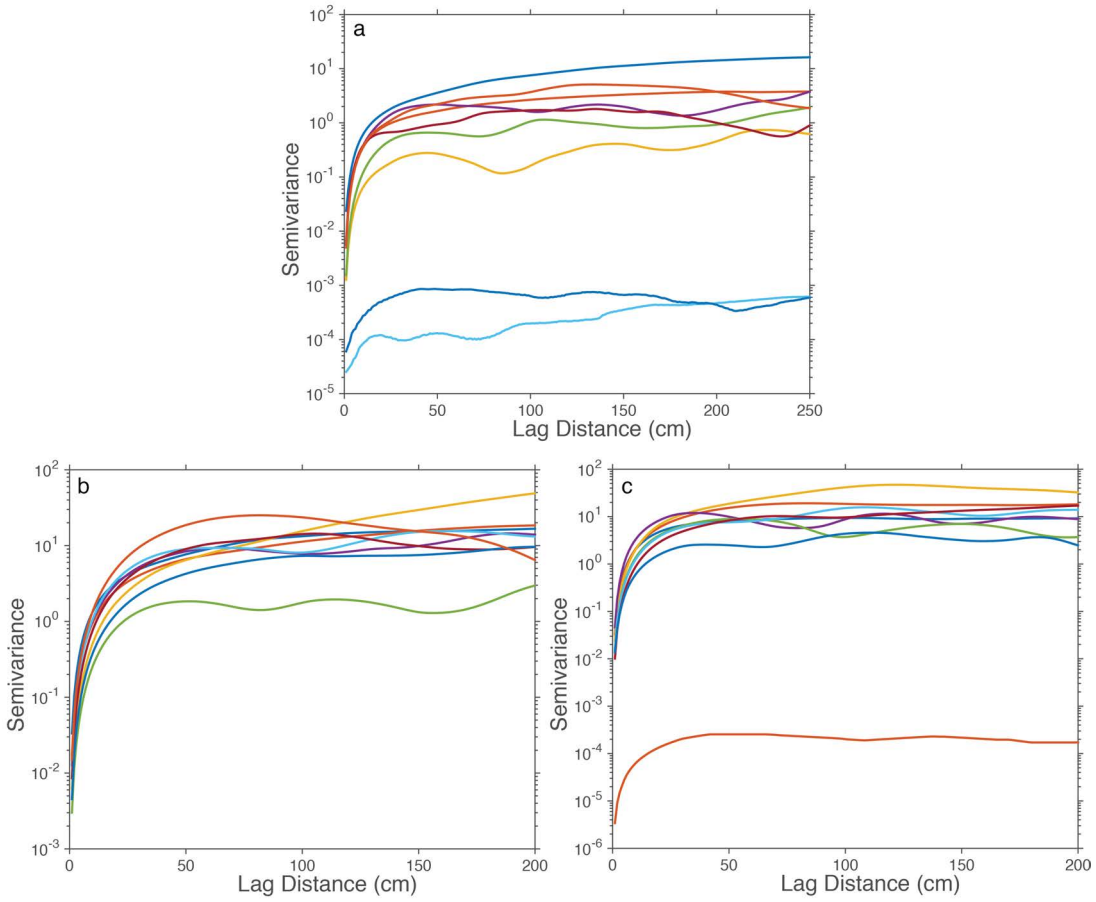

FIGURE 5.6: Semivariogram of snow layer thickness within trenches excavated in Trail Valley Creek for a) the top layer, b) the middle layer and c) the bottom layer, colours relate to the different trenches sampled

Table 5.2: Range (cm) at sill for top middle and bottom layer thicknesses in each trench

Trench	Top	Middle	Bottom
2	296	149	60
4	184	225	78
6	400	351	134
7	49	190	29
8	276	53	39
9	365	178	115
10	85	87	184
11	32	144	103
12	126	68	42

5.4.2 Boundary Roughness Variability

Boundary roughness was measured using the random roughness method outlined in Chapter 3. Roughness was calculated relative to a 50 cm running mean in keeping with past studies such as Rutter et al. (2014). The trenches contained complex stratigraphy particularly in the middle of the snowpack where many wind slab layers overlapped. To maintain consistency the boundary roughness of the snow surface, ground surface, top of the bottom snow layer and bottom of the top snow layer was considered. Figure 5.7 shows the random roughness metric of each 50 cm section of snowpack plotted against the proportional height of the snow layer. Exponential curves were fitted to each roughness profile for each trench, Figure 5.7 shows these fits for each trench and the values for each coefficient in the exponential fit is shown in Table 5.3. While there is an overall relationship showing a decrease in roughness towards the top of the snowpack it was not possible to generalise the relationship between proportional height and boundary roughness using a measurable parameter, such as ground

or snow roughness. Figure 5.8 shows a generalised relationship (fitted exponent) for all of the data points collected as well as 95% confidence prediction bounds. The general fit has the equation $f(x) = 1.986exp(-0.061x)$, the upper prediction bound $f(x) = 1.459exp(-0.0793x)$, and lower prediction bound $f(x) = 2.492exp(-0.04223x)$.

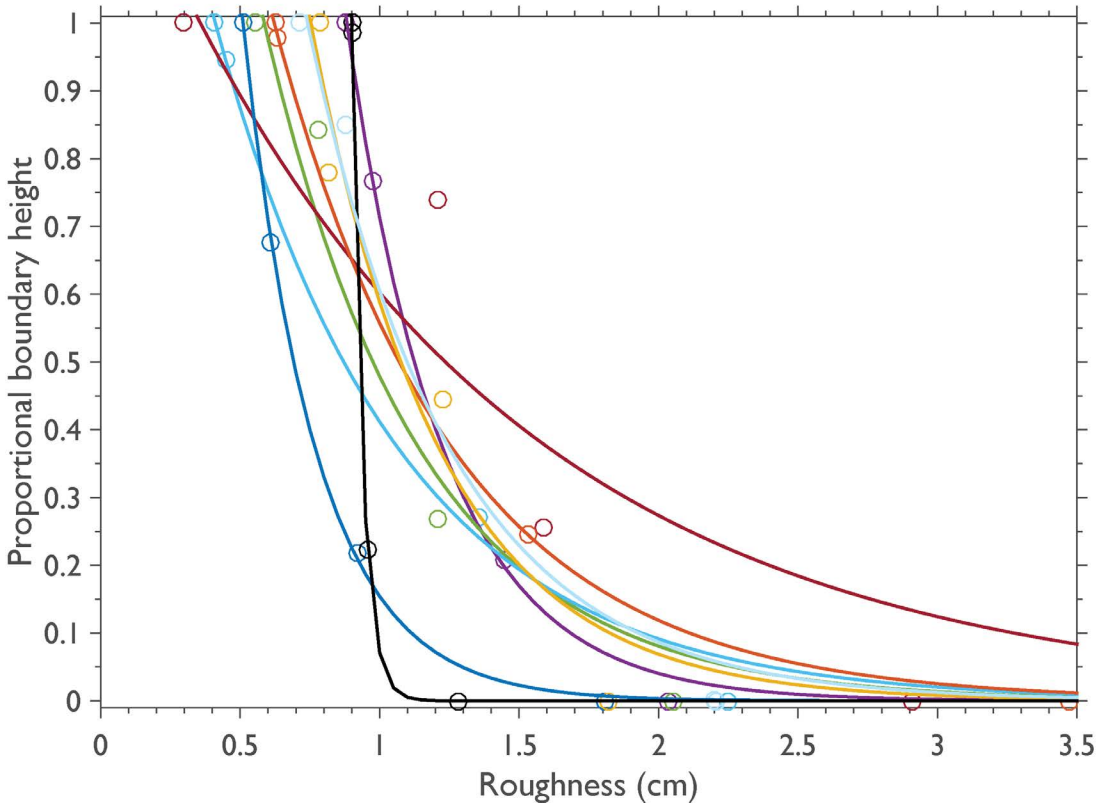

FIGURE 5.7: Layer boundary roughness compared to proportional layer boundary height, each colour indicates the results from each trench, each point represents the roughness of the layer and its proportional height within the trench, lines are exponential fits the coefficients of which are detailed in Table 5.3

TABLE 5.3: Coefficients from the exponential relationships fitted to the boundary height and roughness relationships plotted in figure 5.7, equation of the fits takes the form $a\exp(bx)$

Trench	a	b
2	12.58	-2.87
4	2.84	-1.78
6	1.86	-1.51
7	1.33	-0.79
8	6.99	-3.81
9	2.62	-1.55
10	5.04	-2.15
11	1.99×10^{10}	-26.36
12	4.23	-1.94

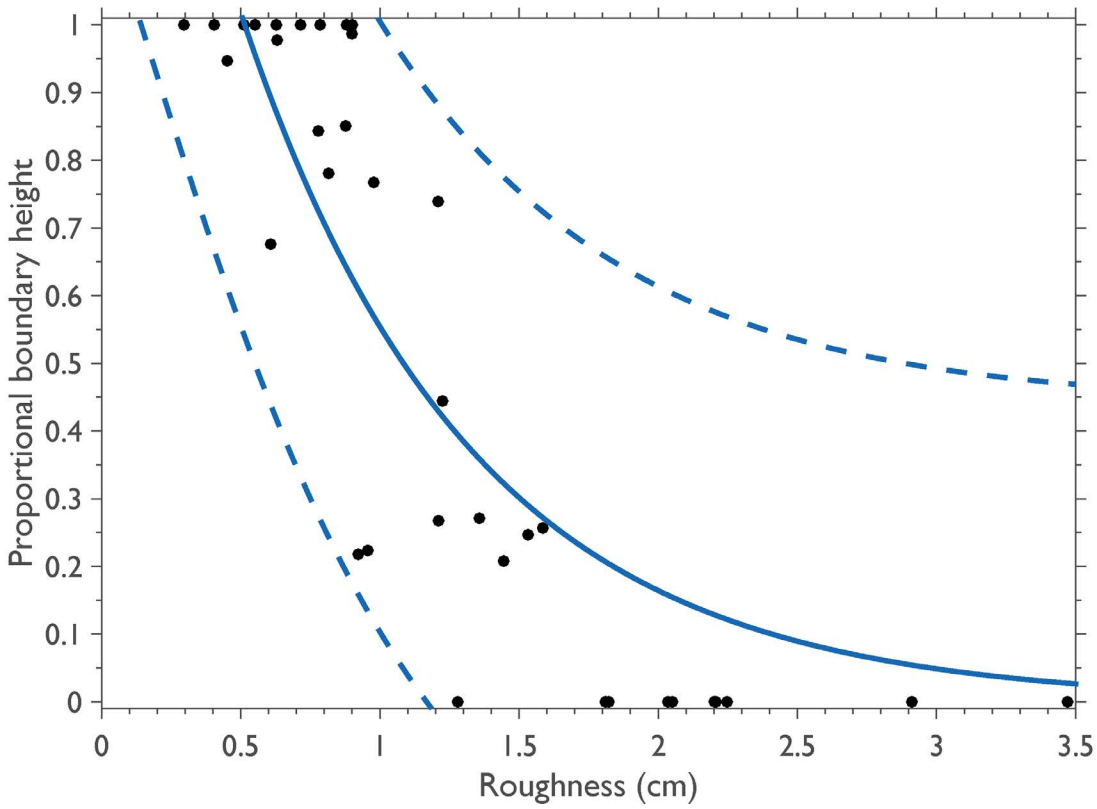

FIGURE 5.8: Layer boundary roughness compared to proportional layer boundary height with a generalised fit and 95% confidence prediction bounds

5.4.3 Variation in simulated brightness temperatures

The n-HUT snow emission model was run for each snow profile in the trenches excavated using the methodology described in Chapter 3. Soil properties were assumed to be a mineral soil with a highly reflective surface and permittivity of $6 - j$ (Hallikainen et al., 1985). Soil properties were assumed to be consistent between sites. For the 50 m trench, Trench 4, it was possible to visualise the additional data that a continuous trench profile provides over a series of 10 pits each approximately 5 m apart from each other. Figure 5.9 shows the brightness temperature simulations from these ten profiles as red lines on the histogram simulations from the entire trench.

From the simulated brightness temperatures semivariograms were plotted, these are shown in Figure 5.10. The values for the range at the sill were calculated using the method mentioned previously and are shown in Table 5.4. Similarly to the results from the layer thickness semivariograms the maximum value for the range at the sill is 297 cm. This means that for the tundra landsurface a trench of 297 cm should be able to capture the variability of the brightness temperature simulations for this land cover.

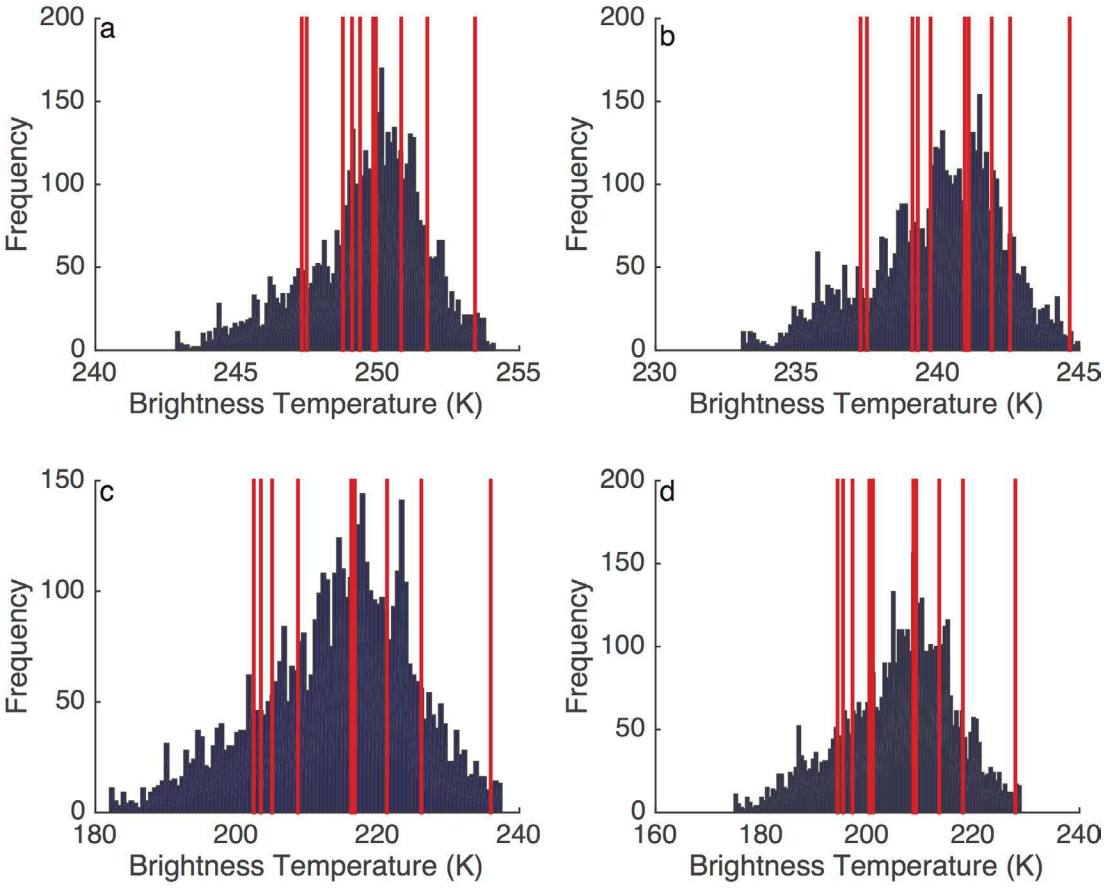

FIGURE 5.9: Comparison of trench data and distributed pit data, for trench 4, snow profiles were distributed approximately every 5 m along a 50 m trench. a) 19V, b)19H, c)37V, d)37H

TABLE 5.4: Range (lag distance) at sill of semivariograms

	Frequency / Polarisation			
Trench	19V	19H	37V	37H
4	80	78	79	79
6	158	154	162	162
7	158	144	176	171
8	28	29	28	28
9	297	261	277	268
10	132	139	131	132
11	180	171	181	175
12	50	50	51	50

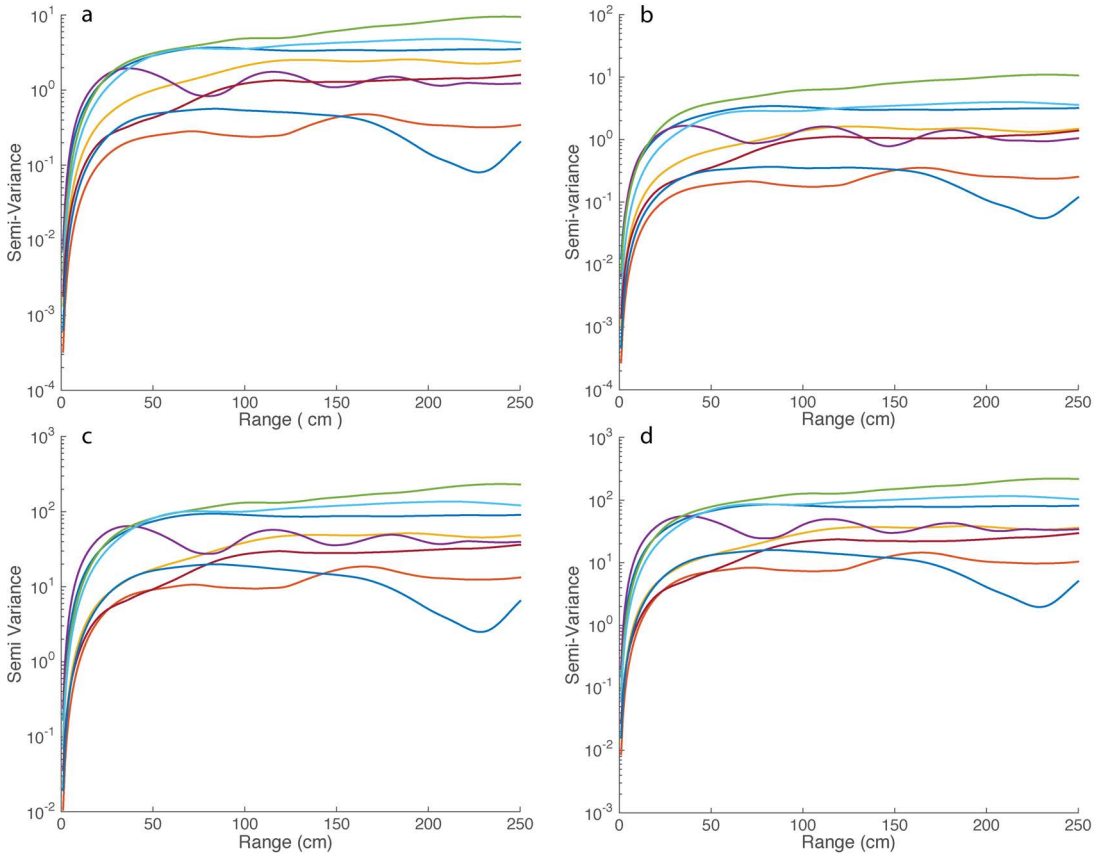

FIGURE 5.10: Semivariograms of simulated brightness temperatures across digitised snow trenches of log-linear scale

5.4.4 Sample size to accurately simulate brightness temperature

Data presented here can be used to inform sampling strategies for arctic environments. The key value is the calculation of the average brightness temperature of the snow cover and so knowing the size of sample which is required to be able to accurately model is crucial.

The brightness temperature simulations generally conformed to a normal distribution (example shown in Figure 5.11) meaning that because of the central

limit theory of normal distributions and due to the large sample size, parametric statistics can be used for data analysis.

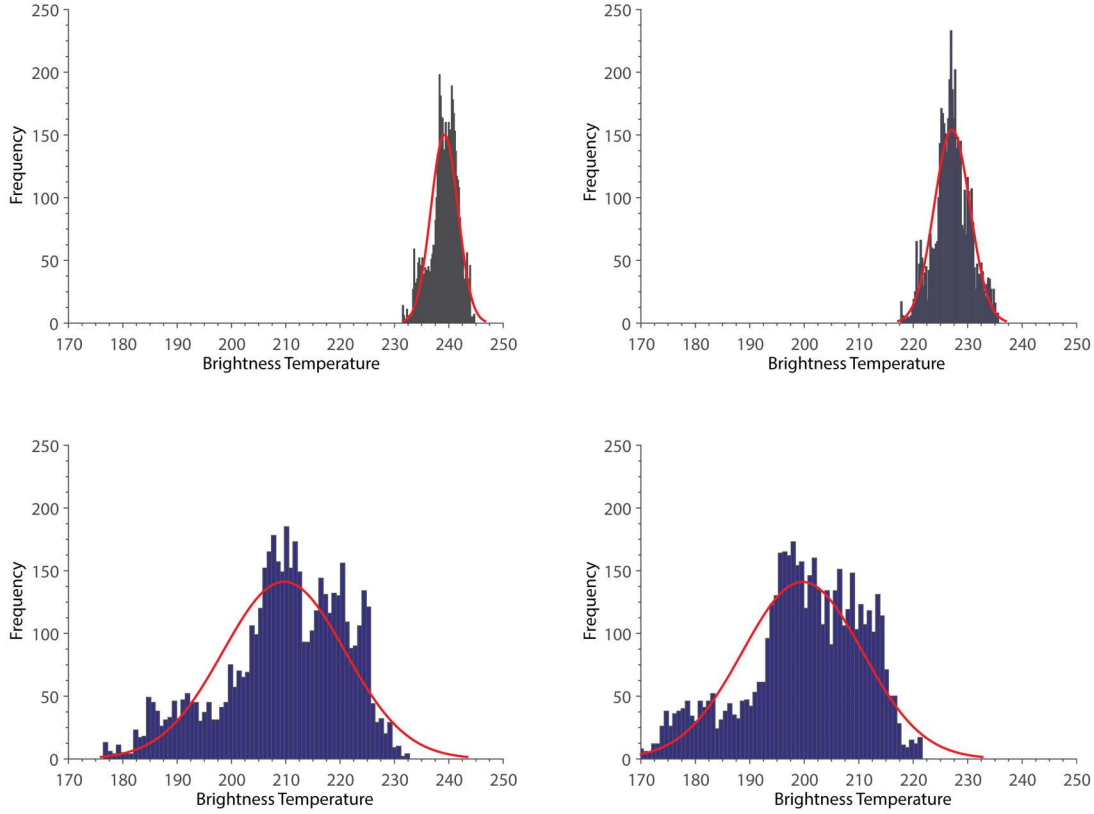

FIGURE 5.11: Histograms for a) 19 GHz V-pol, b) 19 GHz H-pol, c) 37 GHz V-pol, d) 37 GHz H-pol showing the distribution of simulated brightness temperatures obtained from running the n-HUT model for the length of trench 4. Normal distributions have been fitted to the histograms.

If each trench is considered as a population of snow profiles representing a small area which needs to be sampled then it is possible, based on the standard deviation and margin of error of a surface based radiometer (± 2 K) (Asmus and Grant, 1999), to calculate the required sample size to achieve the population mean, to a 99% confidence level using

$$n = (2.326\frac{\sigma}{MOE})^2 \tag{5.2}$$

Where MOE is the margin of error, n is the sample size and σ is the standard deviation of the population (all the values simulated for each trench). Table 5.5 shows the minimum sample size calculated for each trench, polarisation and frequency. Figure 5.12 provides a visual insight into the impact of increasing the sample size to below the given sensor error of a radiometer. Taking account of the ± 2 K error in observed brightness temperatures a 249 cm trench is required to capture the same mean value, accounting for error, as the 50 m trench. This supports the semivariograms in Figure 5.10 which show that variability is fully quantified over 3 m.

Table 5.5: Minimum sample size to achieve population mean for given standard deviation, using a margin of error of ± 2 K and a confidence level of 99%.

Trench	Freq/pol	Mean (K)	SD (K)	population	min sample size
4	19v	239	2.5	5017	9
	19h	227	3.29	5017	13
	37v	210	11.24	5017	133
	37h	200	11.01	5017	116
6	19v	175	1.85	500	3
	19h	155	1.44	500	1
	37v	123	8.25	500	25
	37h	113	7.15	500	16
7	19v	241	1.31	502	2
	19h	224	1.32	502	2
	37v	226	8.06	502	79
	37h	211	7.49	502	60
9	19v	232	3.42	506	15
	19h	222	3.59	506	15
	37v	190	16.93	506	249
	37h	183	16.42	506	216
10	19v	235	2.44	502	8
	19h	218	2.21	502	6
	37v	203	12.98	502	166
	37h	188	11.99	502	122
11	19v	232	1.37	502	2
	19h	201	1.28	502	2
	37v	193	6.52	502	38
	37h	170	5.9	502	24
12	19v	182	0.88	503	1
	19h	163	0.72	503	1
	37v	149	4.98	503	13
	37h	138	4.47	503	9

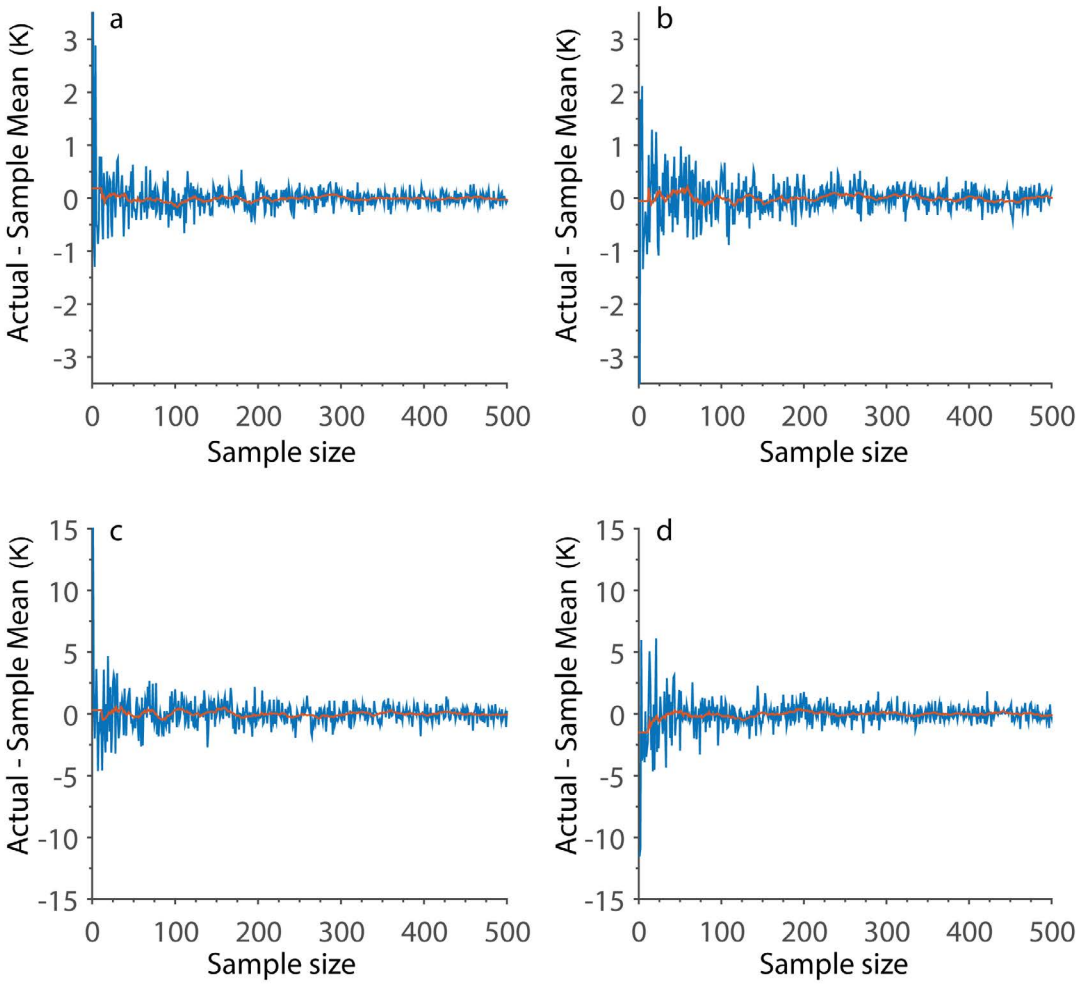

FIGURE 5.12: a random sample was taken from the simulated brightness temperatures with a 50 m snow trench, the mean brightness temperature of that sample is compared to the sample size here, the red line is a 50 sample moving average. a)19 GHz V-pol, b)19 GHz H-pol, c)37 GHz V-pol, d)37 GHz H-pol

5.4.4.1 Differences between sites

As well as investigating the role of stratigraphic variability within different locations in each trench, it is also important to compare the simulated brightness temperatures between different trenches at different locations on the tundra landcover. Figure 5.13 shows the observed satellite brightness temperature as well as the mean brightness temperature for each frequency and polarisation for each trench location. Trenches 6 and 12 had a consistently lower mean brightness temperature due to an increased depth hoar thickness at those sites and a hard coarse, facetted wind slab layer.

Table 5.6 summarises the mean and standard deviation of the simulated brightness temperatures for groups of: all trenches, just the trenches containing the facetted wind slab layer (6 and 12), or just the trenches which didn't contain this layer. The minimum sample size required to obtain the population mean for each of these snowpack categories was also calculated. If samples are just taken randomly, from all sites then 4976 samples are required to accurately calculate the mean. This makes the assumption that samples would include both types of snow, so to capture this variability samples must also be distributed spatially. Note, that the lower sample sizes shown in the table for just sites 6 and 12 are a function of the lower simulated brightness temperatures and the margin or error being based on a static $\pm$ 2 K level.

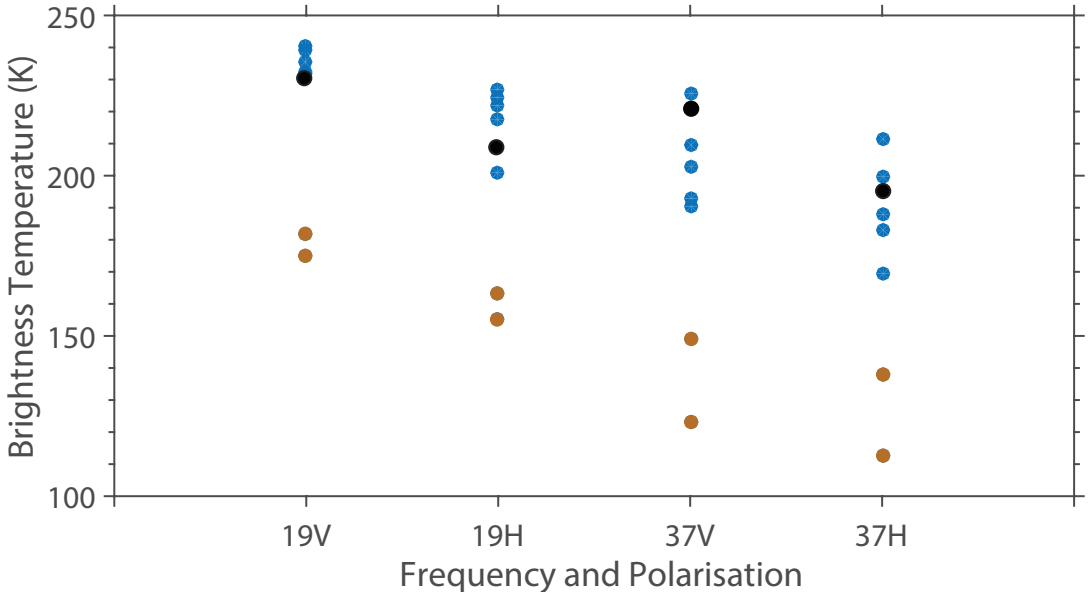

FIGURE 5.13: The mean brightness temperature modelled at every trench excavated in Trail Valley Creek. The orange points are sites 6 and 12, which have a consistently lower modelled brightness temperature than the other sites on tundra landcover over the watershed. SSM/I satellite radiometer readings are shown as black points

TABLE 5.6: Comparison between the simulated brightness temperatures and required minimum sample size between different groups of sites

		All Sites	Without 6 and 12	Just 6 and 12
Mean	19V	231	238	179
	19H	216	224	159
	37V	199	208	136
	37H	187	196	125
Std	19V	20	4	4
	19H	23	8	4
	37V	28	14	15
	37H	28	15	14
Sample Size	19V	3539	124	72
	19H	3966	476	79
	37V	4976	1406	675
	37H	4467	1383	508

5.5 Discussion

The snowpack observed at Trail Valley Creek agreed with previous observations of arctic snowpacks cited in Sturm et al. (1993) and Derksen et al. (2014), a shallow snowpack consisting of approximately six vertical layers. The bottom layer was a depth hoar layer consisting of very large (3.5 mm) chains. This was overlaid with wind slab layers, in some cases (trenches 6 and 12) these layers had become facetted and experienced grain growth, leading to hard, high density coarsely grained layers in the middle of the snowpack.

In terms of the stratigraphic variability of the snowpack, semivariograms showed that variation in layer thickness was fully characterised after only 365 cm. This agrees with similar work by Sturm and Benson (2004) which found that on large scales layers were largely continuous and did not exhibit much variability but at shorter scales variability increased. No ice lenses or layers were present in the snowpack.

Impact that the variability in stratigraphy has on simulated brightness temperatures is addressed in two ways. At individual trench sites the maximum range of the sill for any individual site on the semivariogram of brightness temperature was 297 cm. The range at the sills of the brightness temperature semivariograms was consistently shorter than the semivariograms of layer variability alone, this is because the brightness temperature variation is a function of the variation in

all layers, leading to increased variability over shorter distances and therefore a shorter range at the sill.

The presence of the coarsely grained facetted wind slab layer at some sites caused these locations to have a much lower simulated brightness temperature. This helps address an important question regarding the method in which snow sampling strategies are conducted. The minimum sample size required to obtain the mean brightness temperature for each individual trench was always less than 249. However, for all the trenches it was 4976. When the trenches were subset into those with coarsely grained wind slab layer and those without it, the sample size was less than 1406. This highlights how snowpack sampling strategies need to capture the breadth of different snowpack structures in a field site but also capture the local variability to a high enough degree to ensure the mean at that location is actually representative of that snowpack. This has particular application to work such as Derksen et al. (2012a). Sampling strategies should aim to capture a range of aspects/slope angles and elevations as well as vegetation types. It should be noted that the satellite observations displayed in Figure 5.13 match the mean values for the sites which did not include the coarsely grained wind slab. This highlights the further questions that exist in how sub-footprint variability effects the observed brightness temperature at the satellite scale.

The smaller scale roughness between the boundaries of the snow layers can now be characterised from NIR photograph and the metrics described in Fassnacht et al. (2009b) and Anttila et al. (2014) applied. Snow layer boundary roughness

decreases exponentially within the snowpack from the ground to the surface, although as it was not possible to generalise this, it is only possible to estimate the boundary roughness of internal layers when both the surface roughness and ground roughness are known. The equation $f(x) = 1.986exp(-0.061x)$ described the general relationship of all the boundary roughnesses sampled in relation to their proportional height and for future measurements the 95% upper prediction bound had the equation $f(x) = 1.459exp(-0.0793x)$ and lower prediction bound the equation $f(x) = 2.492exp(-0.04223x)$. Data from other sites will be required to test with wider applicability of this relationship. Aside from snow emission modelling, knowing the roughness of internal layer boundaries has applications to a wide range of snow research, including snow evolution modelling and radar backscatter modelling.

5.6 Summary

At the start of this chapter, three aims were identified, this section will address each of them individually.

5.6.1 Quantify layer thickness and boundary roughness variability

Layer thickness is much more variable in the lower layers of depth hoar, as it is related to the undulation of the ground, and this is demonstrated by the negative covariance correlation between the hoar fraction and snowpack depth. However, when characterising the snowpack using a snow trench there is no significant difference in the range at sill for semivariograms of snow layer thickness. This has important implications for SAR and passive microwave remote sensing, where depth hoar has a large impact, however, more data needed to show if this exists at wider scales.

The roughness between snow layers is quantified here for the first time, the most significant finding being that snow layer boundary roughness decreases with a an exponential relationship as the proportional height of the snow layer increases. This can be used to inform snow evolution, radiometric and surface energy balance modelling.

5.6.2 Quantifying the impact of spatial variability of stratigraphy on Snow Microwave Emission Models

In this work snow trenches of up to 50 m were used to investigate spatial variability of brightness temperature simulations. The main finding is that variability occurs

at a much smaller scale than this, semivariograms reached a sill in brightness temperature simulations before 3 m, meaning that a trench of 3 m length is able to quantify brightness temperature variability to the same level as a 50 m one. This is a key finding for the benefit of small, plot scale trenches for informing variability in brightness temperatures at a wider scale.

5.6.3 Determine what the minimum subset size is

3 m of snow trench measurements will provide enough data points to characterise the brightness temperature at spatial scales of up to at least 50 m. While there are differences between trenches made at different locations within the same landcover type (expected given the variability that is known to exist in tundra environments) at each individual location 3 m allows variability to be fully captured at each site. This is in keeping with other findings looking at spatial scales of variability from the semivariograms presented here.

Chapter 6

Synopsis

6.1 Summary

The overall aim of this thesis is to quantify and evaluate how snowpack stratigraphy influences the precision and accuracy of snow microwave emission models in Arctic tundra environments. This has implications for many areas of research, but the ability to quantify error and uncertainty of stratigraphy measurements and microwave brightness temperature simulations, has particular implications for data assimilation schemes used in deriving SWE products.

Figure 6.1 shows the key way that using trench based NIR photography both provides the data for the observed snowpack stratigraphy, and informs error and uncertainty on those measurements. These measurements of error and uncertainty

can, in turn, be used to inform error analysis on simulated brightness temperatures from snowpack observations and the output from snowpack evolution models. Simulated brightness temperatures from snowpack evolution models and observations are types of data which are implemented, or have the potential to be, implemented in data assimilation schemes (Langlois et al., 2012).

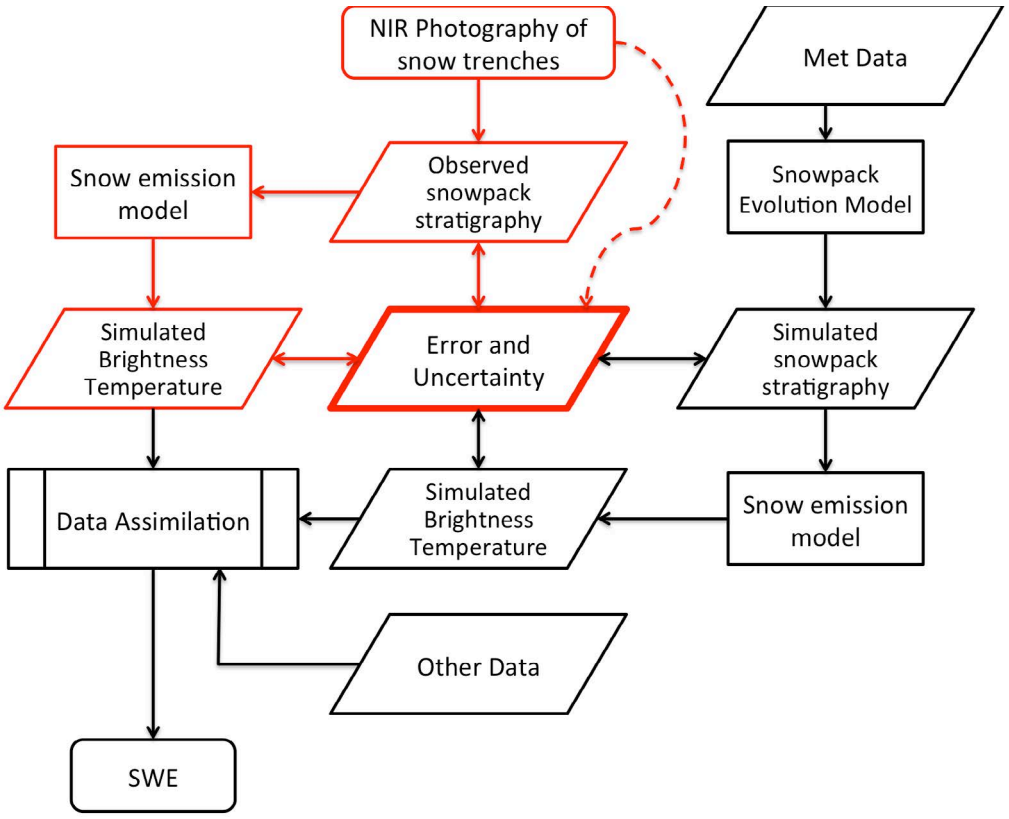

FIGURE 6.1: Flow chart of the key areas used in data assimilation schemes, the sections highlighted in red are improved by the work in this thesis although as can be seen, there are further implications in other areas

6.1.1 Snowpack stratigraphy

In this thesis two key weaknesses in the current literature were identified. Firstly that ice layers pose a considerable challenge to snow emission models (Rees

et al., 2010; Durand et al., 2008) and secondly that spatial variation of snowpack stratigraphy, at spatial scales smaller than the satellite footprint, are not well quantified or characterised for Arctic tundra environments (Rutter et al., 2014; Derksen et al., 2012b). Methodological developments presented here have made considerable improvements to both of these weaknesses. Existing work which addressed the question of snowpack stratigraphy variation at small scales, was limited to looking at single short trenches (Rutter et al., 2014; Domine et al., 2012) or a series of pits (Derksen et al., 2009). Here, a method for digitising snowpack stratigraphy from NIR photography collected along a trench (initially presented by Tape et al. (2010)), was optimised and improved to the point where it was accurate enough for use in a hummocky tundra environment, over distances of up to 50 m, and fast enough to allow spatially distributed sampling to be conducted over a wide tundra area. New methods of converting the NIR photographs collected into pixel co-ordinates provided the main improvement. By addressing each point on an NIR photograph and relating it directly to a location in cm, determined by use of a physical scale present in each photograph, it was possible to ensure accuracy along a trench, or series of trenches, while simultaneously decreasing the time required for analysis to be conducted.

These developments meant it was possible to: collect and analyse the longest (to my knowledge) continuous profiles of cm accurate snowpack stratigraphy, recorded in a tundra environment; collect and analyse a large, spatially distributed snow trench dataset, which allowed stratigraphy variability to be examined across

a tundra watershed; measure internal snowpack layer boundary roughness and locate snowpack properties recorded within a snow trench with cm accuracy, allowing variation in properties, as well as stratigraphy, to be analysed across a trench.

The improved trench methods were used to simulate brightness temperature on data collected in Churchill MB. and Inuvik NWT. At Churchill it was noted that ice layers in the snowpack led to distributions of brightness temperatures which were split into two distinct peaks, dependent on whether or not the ice layer was present in the pack. As no ice layers were present at Inuvik the brightness temperature simulations provided a continuous distribution. Semivariograms of the brightness temperature simulations showed that, variation in brightness temperature occurred at a shorter scale than variation in any individual snowpack layer, and that, for any individual site, a trench of 3 m length would completely characterise the variation in brightness temperature for that area.

Internal layer boundary roughness was measured at both Churchill and Inuvik. At Inuvik, layer boundary roughness decreased exponentially with the proportional height of the layer boundary within the snowpack, although it was not possible to generalise this relationship as a function of either ground or surface roughness. The role of internal layer boundary roughness is an important factor in radar measurements, as layer boundary roughness at scales less than the footprint causes difficulty in radar stratigraphy interpretation (Marshall and Koh, 2008). From a passive microwave perspective, if snow emission models are run in two dimensions

then layer boundary roughness will need to be included. Additionally snowpack evolution models need this data to verify and calibrate their outputs.

6.1.2 Ice layer Density

The second methodological development was to measure the density of ice layers. This was done at sites in Southern and Northern Ontario and Inuvik in the Canadian NWT, on both naturally occurring ice layers and ones created by spraying water onto the snowpack at low temperatures. Ice layers were found be have a density very close to solid, planar ice, and ice layer density was found to have an impact on the accuracy of simulated brightness temperature measurements in the region of 5 - 50 K. Previous work had used ice layer density measurements significantly lower than the recorded value of 909 kg m^{-3} which was found to give more accurate simulations but did not accurately represent reality, suggesting that weaknesses in the way in which snow emission models parameterise ice layers is the cause for the error in the simulated output. The impact of the findings of this thesis are shown in Figure 6.2

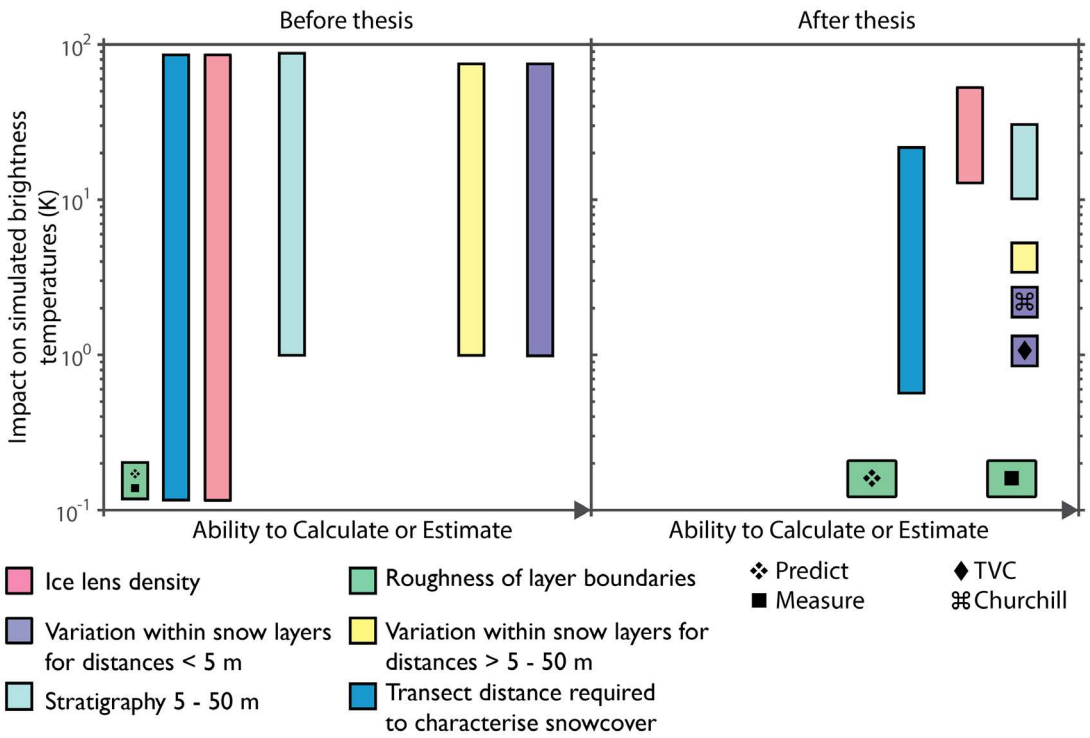

FIGURE 6.2: Conceptual diagram of the areas improved by this research, left hand side shows the state of knowledge before the work conducted here and the right hand side shows the state afterwards. Large areas indicate areas of uncertainty.

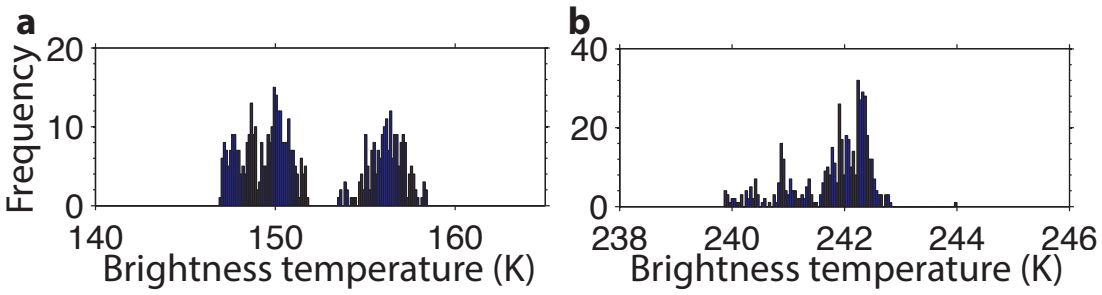

FIGURE 6.3: Comparison of a typical brightness temperature distribution for 19 GHz H-pol when ice layers are a) absent and b) present

When snow emission models and passive microwave observations are used in data assimilation schemes, a key part of the data assimilation algorithm is the weight the observations are given based on the potential error from each of the error sources which act on an observation (Reichle, 2008). Currently only vertically polarised brightness temperatures are considered due to the impact that ice layers have on horizontal polarisations. The work in this thesis highlights stratigraphic variation and ice layers as two sources of error, and provides data and analysis which will aid in their contribution to the error budget of passive microwave observations and simulations. Both of these error sources have been identified previously, however, their role in influencing the brightness temperature within the context of a heterogeneous snowpack was not known.

When ice layers were present in the snowpack the distribution of simulated brightness temperatures was split to form two peaks as shown in Figure 6.3 (b). When calculating the error in simulated or observed brightness temperatures it is important that this difference is recognised, as brightness temperatures when no ice layers are present are likely to form a normal or quasi-normal distribution but when ice layers are present, they will not. The method used to determine the error budget for each of these two scenarios should be tailored to the individual distribution.

It is therefore of key importance to be able to detect if an ice layer is present in the footprint of a satellite radiometer. Methods for doing this have been proposed (Grenfell and Putkonen, 2008) but they use the polarisation ratio, a metric which

has been shown here to be be influenced by the density of the ice layer present. Based on this finding the future work outlined in the following section is suggested.

6.2 Future Work

Future work should focus on...

- Parameterising ice layers to correctly account for ice layer density in snow emission models
- Including ice layer density in the development of algorithms for ice layer detection
- The trench methods demonstrated here should be applied for use with other ground based sensors

References

Albert, M. R. and Perron Jr, F. E. (2000). "Ice layer and surface crust permeability in a seasonal snowpack". In: *Hydrological Processes* 14.18, pp. 3207–3214.

Anttila, K., Manninen, T., Karjalainen, T., Lahtinen, P., Riihelä, A., and Siljamo, N. (2014). "The temporal and spatial variability in submeter scale surface roughness of seasonal snow in Sodankylä Finnish Lapland in 2009-2010". In: *Journal of Geophysical Research: Atmospheres* 119, pp. 1–17.

Armstrong, R. L. and Brodzik, M. J. (2002). "Hemispheric-scale comparison and evaluation of passive-microwave snow algorithms". In: *Annals of Glaciology* 34.1, pp. 38–44.

Armstrong, R. L., Chang, A., Rango, A., and Josberger, E. (1993). "Snow depths and grain-size relationships with relevance for passive microwave studies". In: *Annals of Glaciology* 17, pp. 171–176.

Asmus, K. W. and Grant, C. (1999). "Surface Based Radiometer (SBR) Data Acquisition System". In: *International Journal of Remote Sensing* 20.15-16, pp. 3125–3129.

Barnett, T. P., Adam, J. C., and Lettenmaier, D. P. (2005). "Potential impacts of a warming climate on water availability in snow-dominated regions." In: *Nature* 438.7066, pp. 303–9.

Baunach, T., Fierz, C., Satyawali, P. K., and Schneebeli, M. (2001). "A model for kinetic grain growth". In: *Annals of Glaciology* 32.1, pp. 1–6.

Bernier, P. Y. (1987). "Microwave remote sensing of snowpack properties: potential and limitations". In: *Nordic Hydrology* 18.1, pp. 1–20.

Boyarskii, D. A. and Tikhonov, V. V. (2000). "The Influence of Stratigraphy On Microwave Radiation From Natural Snow Cover". In: *Journal of Electromagnetic Waves and Applications* 14.9, pp. 1265–1285.

Brown, R. D., Derksen, C., and Wang, L. (2007). "Assessment of spring snow cover duration variability over northern Canada from satellite datasets". In: *Remote Sensing of Environment* 111, pp. 367–381.

Canny, J (1986). "A computational approach to edge detection." In: *IEEE Transactions on Pattern Analysis and Machine Intelligence* 8.6, pp. 679–98.

Chang, A. T. C., Foster, J. L., Hall, D. K., Rango, A., and Hartline, B. K. (1981). *Snow water equivalent determination by microwave radiometry.* Tech. rep. Goddard Space Flight Centre, Greenbelt, Maryland, 20771: NASA Technical Report 19810011961.

Chang, A. T. C., Foster, J. L., Hall, D. K., Rango, A, and Hartline, B. K. (1982). "Snow Water Equivalent Estimation by Microwave Radiometry". In: *Cold Regions Science and Technology* 5.3, pp. 259–267.

Chang, A. T. C., Foster, J. L., and Hall, D. K. (1987). "Nimbus-7 SMMR derived global snow cover parameters". In: *Annals of Glaciology* 9, pp. 39 –44.

Chang, A. T. C., Foster, J. L., Hall, D. K., Goodison, B. E., Walker, A. E., Metcalfe, J. R., and Harby, A. (1997). "Snow parameters derived from microwave measurements during the BOREAS winter field campaign". In: *Journal of Geophysical Research* 102.D24, p. 29663.

Chapin, F. S., Sturm, M., Serreze, M. C., McFadden, J. P., Key, J. R., Lloyd, A. H., Mcguire, D. A., Rupp, T. S., Lynch, A. H., Schimel, J. P., Beringer, J, Chapman, W. L., Epstein, H. E., Euskirchen, E. S., Hinzman, L. D., Jia, G., Ping, C. L., Tape, K. D., Thompson, C. D. C., Walker, D. A., and Welker, J. M. (2005). "Role of land-surface changes in Arctic summer warming". In: *Science* 657.2005.

Church, J. E. (1933). "Snow Surveying: Its Principles and Possibilities". In: *Geographical Review* 23.4, pp. 529–563.

Clifford, D. (2010). "Global estimates of snow water equivalent from passive microwave instruments: history, challenges and future developments". In: *International Journal of Remote Sensing* 31.14, pp. 3707–3726.

Colbeck, S. C. (1991). "The layered character of snow covers". In: *Reviews of Geophysics* 29.90, pp. 81–96.

Colbeck, S. C. and Anderson, E. A. (1982). "The Permiability of Melting snow". In: *Water Resources Research* 18.4, pp. 904–908.

Crook, J. A., Forster, P. M., and Stuber, N. (2011). "Spatial Patterns of Modeled Climate Feedback and Contributions to Temperature Response and Polar Amplification". In: *Journal of Climate* 24.14, pp. 3575–3592.

Derksen, C. (2008). "The contribution of AMSR-E 18.7 and 10.7 GHz measurements to improved boreal forest snow water equivalent retrievals". In: *Remote Sensing of Environment* 112.5, pp. 2701–2710.

Derksen, C. and Brown, R. D. (2012). "Spring snow cover extent reductions in the 2008,Äì2012 period exceeding climate model projections". In: *Geophysical Research Letters* 39.19, p. L19504.

Derksen, C., Walker, A., Ledrew, E., and Goodison, B. (2002). "Time-series analysis of passive-microwave-derived central North American snow water equivalent imagery". In: *Annals of Glaciology* 34.1, pp. 1–7.

Derksen, C, Lemmetyinen, J, Toose, P, Silis, A, Pulliainen, J, and Sturm, M (2014). "Physical properties of Arctic versus subarctic snow: Implications for high latitude passive microwave snow water equivalent retrievals". In: *Journal of Geophysical Research: Atmospheres* 119.

Derksen, Chris, Walker, A, and Goodison, B (2003). "A comparison of 18 winter seasons of in situ and passive microwave-derived snow water equivalent estimates in Western Canada". In: *Remote Sensing of Environment* 88.3, pp. 271–282.

Derksen, Chris, Silis, A., Sturm, M., Holmgren, J., Liston, G. E., Huntington, H. P., and Solie, D. (2009). "Northwest Territories and Nunavut Snow Characteristics from a Subarctic Traverse: Implications for Passive Microwave Remote Sensing". In: *Journal of Hydrometeorology* 10.2, pp. 448–463.

Derksen, Chris, Toose, Peter, Lemmetyinen, Juha, Pulliainen, Jouni, Langlois, Alexandre, Rutter, Nick, and Fuller, M C (2012a). "Evaluation of passive microwave brightness temperature simulations and snow water equivalent retrievals through a winter season". In: *Remote Sensing of Environment* 117, pp. 236–248.

Derksen, Chris, Smith, S L, Sharp, M J, Brown, Laura, Howell, S E L, Copland, L, Mueller, D R, Gauthier, Y, Flecther, C G, Tivy, A, Bernier, Monique, Bourgeois, J, Brown, Ross D, Burn, C R, Duguay, Claude R, Kushner, P, Langlois, Alexandre, Lewkowicz, A G, Royer, Alain, and Walker, A (2012b). "Variability and change in the Canadian cryosphere". In: *Climatic Change*.

Diffenbaugh, Noah S, Scherer, Martin, and Ashfaq, Moetasim (2013). "Response of snow-dependent hydrologic extremes to continued global warming." In: *Nature Climate Change* 3.4, pp. 379–384.

Domine, Florent, Gallet, Jean-Charles, Bock, Josué, and Morin, Samuel (2012). "Structure, specific surface area and thermal conductivity of the snowpack around Barrow, Alaska". In: *Journal of Geophysical Research* 117.January, D00R14.

Dupont, Florent, Royer, Alain, Langlois, Alexandre, Gressent, Al, Picard, Ghislain, Fily, M, Cliche, Patrick, and Chum, M (2012). "Monitoring the melt season length of the Barnes Ice Cap over the 1979 ,Äì 2010 period using active and passive microwave remote sensing data". In: *Hydrological Processes* 26, pp. 2643–2652.

Dupont, Florent, Picard, Ghislain, Royer, Alain, Fily, Michel, Roy, Alexandre, Langlois, Alexandre, and Champollion, Nicolas (2014). "Modeling the Microwave Emission of Bubbly Ice: Applications to Blue Ice and Superimposed Ice in the Antarctic and Arctic". In: *IEEE Transactions on Geoscience and Remote Sensing* 52.10, pp. 6639 –6651.

Durand, Michael T. and Margulis, Steven A (2006). "Feasibility test of multifrequency radiometric data assimilation to estimate snow water equivalent". In: *Journal of Hydrometeorology* 7.3, pp. 443–457.

Durand, Michael T. and Margulis, Steven a. (2007). "Correcting first-order errors in snow water equivalent estimates using a multifrequency, multiscale radiometric data assimilation scheme". In: *Journal of Geophysical Research: Atmospheres* 112.D13, n/a–n/a.

Durand, Michael T., Kim, Edward J, and Margulis, Steven A (2008). "Quantifying uncertainty in modeling snow microwave radiance for a mountain snowpack at the point-scale, including stratigraphic effects". In: *IEEE Transactions on Geoscience and Remote Sensing* 46.6, pp. 1753–1767.

Durand, Michael T., Kim, Edward J, and Margulis, Steven A (2011). "A First-Order Characterization of Errors From Neglecting Stratigraphy in Forward and Inverse Passive Microwave Modeling of Snow". In: *Geoscience and Remote Sensing Letters* 8.99, pp. 730–734.

Elder, Kelly, Cline, Don W, Liston, Glen E, and Armstrong, Richard L. (2009). "NASA Cold Land Processes Experiment (CLPX 2002/03): Field Measurements of Snowpack Properties and Soil Moisture". In: *Journal of Hydrometeorology* 10.1, pp. 320–329.

Fassnacht, Steven R, Williams, M W, and Corrao, M V (2009a). "Changes in the surface roughness of snow from millimetre to metre scales". In: *Ecological Complexity* 6.3, pp. 221–229.

Fassnacht, Steven R, Stednick, J D, Deems, J S, and Corrao, M V (2009b). "Metrics for assessing snow surface roughness from digital imagery". In: *Water Resources Research* 45, W00D31.

Fierz, C, Armstrong, Richard L., Durand, Y, Etchevers, P, Greene, E, McClung, D M, Nishimura, K, Satyawali, P K, and Sokratov, S A (2009). *The International Classification for Seasonal Snow on the Ground*. Tech. rep. Paris: UNESCO-IHP.

Foster, J (1997). "Comparison of snow mass estimates from a prototype passive microwave snow algorithm, a revised algorithm and a snow depth climatology". In: *Remote Sensing of Environment* 62.2, pp. 132–142.

Foster, J. L., Rango, A., Hall, D. K., Chang, A T C, and Allison, L. J. (1980). *Snowpack monitoring in North America and Eurasia using passive microwave satellite data*. Tech. rep. Goddard Space Flight Centre, Greenbelt, Maryland, 20771: NASA Technical Memorandum 80706.

Foster, J L, Barton, J S, and Chang, A T C (2000). "Snow crystal orientation effects on the scattering of passive microwave radiation". In: *IEEE Transactions on Geoscience and Remote Sensing* 38.5, pp. 2430–2434.

Foster, J L, Sun, C J, Walker, J P, Kelly, R E J, Chang, A T C, Dong, J R, and Powell, H (2005). "Quantifying the uncertainty in passive microwave snow water equivalent observations". In: *Remote Sensing of Environment* 94.2, pp. 187–203.

Foster, J.L., Hall, D.K., Chang, A T C, Rango, A., Wergin, W., and Erbe, E. (1999). "Effects of snow crystal shape on the scattering of passive microwave radiation". In: *IEEE Transactions on Geoscience and Remote Sensing* 37.2, pp. 1165–1168.

Gallet, Jean-Charles, Domine, Florent, Zender, C S, and Picard, Ghislain (2009). "Measurement of the specific surface area of snow using infrared reflectance in an integrating sphere at 1310 and 1550 nm". In: *The Cryosphere* 3.2, pp. 167–182.

Goodison, B.E. and Walker, A.E. (1995). *Canadian development and use of snow cover information from passive microwave satellite data*. Ed. by B.J. Choudhury and P. Pampaloni Y.H. Kerr, E.G. Njoku. 1st ed. Utrecht: VSP.

Goodison, B.E., Glynn, J.E., Harvey, K.D., and Slater, J.E. (1987). "Snow Surveying in Canada: A Perspective". In: *Canadian Water Resources Journal* 12.January 2015, pp. 27–42.

Gray, D M and Male, D H (1981). *Handbook of Snow.* Caldwell, New Jersey: The Blackburn Press.

Green, Jeff, Kongoli, Cezar, Prakash, Anupma, Sturm, Matthew, Duguay, Claude R, and Li, Shusun (2012). "Quantifying the relationships between lake fraction, snow water equivalent and snow depth, and microwave brightness temperatures in an arctic tundra landscape". In: *Remote Sensing of Environment* 127, pp. 329–340.

Grenfell, T C and Putkonen, J (2008). "A method for the detection of the severe rain-on-snow event on Banks Island , October 2003 , using passive microwave remote sensing". In: *Water Resources Research* 44, W03425.

Grippa, M., Mognard, N., Le Toan, T., and Josberger, E.G. (2004). "Siberia snow depth climatology derived from SSM/I data using a combined dynamic and static algorithm". In: *Remote Sensing of Environment* 93.1-2, pp. 30–41.

Grody, N.C. and Basist, A.N. (1996). "Global identification of snowcover using SSM/I measurements". In: *IEEE Transactions on Geoscience and Remote Sensing* 34.1, pp. 237–249.

Grody, Norman (2008). "Relationship between snow parameters and microwave satellite measurements: Theory compared with advanced microwave sounding

unit observations from 23 to 150 GHz". In: *Journal of Geophysical Research: Atmospheres* 113.22, pp. 1–17.

Hall, D K, Chang, A T C, and Foster, J L (1986). "Detection of the depth-hoar layer in the snow-pack of the Arctic coastal plain of Alaska, U. S. A., using satellite data". In: *Journal of Glaciology* 32.110, pp. 87–94.

Hallikainen, Martti T, Ulaby, F T, Dobson, Myron, El-rayes, Mohamed, and Wu, Lil-kun (1985). "Microwave Dielectric Behavior of Wet Soil-Part 1: Empirical Models and Experimental Observations". In: *IEEE Transactions on Geoscience and Remote Sensing* GE-23.1, pp. 25–34.

Hallikainen, M.T. and Jolma, P.A. (1992). "Comparison of algorithms for retrieval of snow water equivalent from Nimbus-7 SMMR data in Finland". In: *IEEE Transactions on Geoscience and Remote Sensing* 30.1, pp. 124–131.

Hancock, Steven, Baxter, Robert, Evans, Jonathan, and Huntley, Brian (2013). "Evaluating global snow water equivalent products for testing land surface models". In: *Remote Sensing of Environment* 128, pp. 107–117.

Heggli, Martin, Frei, Esther, and Schneebeli, Martin (2009). "Instruments and methods Snow replica method for three-dimensional X-ray microtomographic imaging". In: *Journal of Glaciology* 55.192, pp. 631–639.

Holland, M M and Bitz, C M (2003). "Polar amplification of climate change in coupled models". In: *Climate Dynamics* 21.3-4, pp. 221–232.

Huang, Chunlin, Margulis, Steven A, Durand, Michael T., and Musselman, K N (2012). "Assessment of snow grain-size model and stratigraphy representation

impacts on snow radiance assimilation: Forward modeling evaluation". In: *IEEE Transactions on Geoscience and Remote Sensing* 50.11, pp. 4551–4564.

Hugin (2011).

Jeffries, M. O., Richter-Menge, J., Overland, J. E., and Eds (2014). *Arctic Report Card 2014*.

Jia, Gensuo J., Epstein, H E., and Walker, D. A. (2006). "Spatial heterogeneity of tundra vegetation response to recent temperature changes". In: *Global Change Biology* 12.1, pp. 42–55.

Josberger, Edward G. and Mognard, Nelly M. (2002). "A passive microwave snow depth algorithm with a proxy for snow metamorphism". In: *Hydrological Processes* 16.8, pp. 1557–1568.

Keegan, K., Albert, M R, and Baker, Ian (2014). "The impact of ice layers on gas transport through firn". English. In: *The Cryosphere Discussions* 8.1, pp. 1095–1110. ISSN: 1994-0440.

Kelly, R E J and Chang, A T C (2003). "Development of a passive microwave global snow depth retrieval algorithm for Special Sensor Microwave Imager (SSM/I) and Advanced Microwave Scanning Radiometer-EOS (AMSR-E) data". In: *Radio Science* 38.4, p. 8076.

Kelly, R E J, Chang, Alfred T. A.T., Tsang, Leung, and Foster, James L. J.L. (2003). "A prototype AMSR-E global snow area and snow depth algorithm". In: *IEEE Transactions on Geoscience and Remote Sensing* 41.2, pp. 230–242.

King, Joshua, Kelly, Richard, Kasurak, Andrew, Duguay, Claude, Gunn, Grant, Rutter, Nick, Watts, Tom, and Derksen, Chris (2014). "Spatiotemporal influence of tundra snow properties on Ku-band (17.2 GHz) backscatter". In: *Journal of Glaciology* 14J020.

Koenig, Lora S. and Forster, Richard R. (2004). "Evaluation of passive microwave snow water equivalent algorithms in the depth hoar-dominated snowpack of the Kuparuk River Watershed, Alaska, USA". In: *Remote Sensing of Environment* 93.4, pp. 511–527.

Langlois, Alexandre, Royer, Alain, and Goïta, Kalifa (2010). "Analysis of simulated and spaceborne passive microwave brightness temperatures using in situ measurements of snow and vegetation properties". In: *Canadian Journal of Remote Sensing* 36.1, pp. 135–148.

Langlois, Alexandre, Royer, Alain, Derksen, Chris, Montpetit, B, Dupont, Florent, and Goïta, Kalifa (2012). "Coupling of the snow thermodynamic model SNOWPACK with the Microwave Emission Model for Layered Snowpacks (MEMLS) for subarctic and arctic snow water equivalent retrievals". In: *Water Resources Research*, pp. 819–821.

Lemmetyinen, Juha, Pulliainen, Jouni, Rees, Andrew, Kontu, Anna, and Derksen, Chris (2010). "Multiple-Layer Adaptation of HUT Snow Emission Model: Comparison With Experimental Data". In: *IEEE Transactions on Geoscience and Remote Sensing* 48.7, pp. 2781–2794.

Li, Dongyue, Durand, Michael, and Margulis, Steven A. (2012). "Potential for hydrologic characterization of deep mountain snowpack via passive microwave remote sensing in the Kern River basin, Sierra Nevada, USA". In: *Remote Sensing of Environment* 125, pp. 34–48.

Liston, Glen E. and Hiemstra, Christopher A. (2011). "The Changing Cryosphere: Pan-Arctic Snow Trends (1979 - 2009)". In: *Journal of Climate* 24.21, pp. 5691–5712.

Loranty, Michael M, Berner, Logan T, Goetz, Scott J, Jin, Yufang, and Randerson, James T (2014). "Vegetation controls on northern high latitude snow-albedo feedback: observations and CMIP5 model simulations." In: *Global Change Biology* 20.2, pp. 594–606.

Marsh, P (1984). "Wetting front advance and freezing of meltwater within a snow cover: 1. Observations in the Canadian Arctic". In: *Water Resources Research* 20.12, pp. 1853–1864.

Marsh, P, Bartlett, Paul, MacKay, M., Pohl, S, and Lantz, T (2010). "Snowmelt energetics at a shrub tundra site in the western Canadian Arctic". In: *Hydrological Processes* 24, pp. 3603–3620.

Marshall, Hans-Peter Peter and Koh, Gary (2008). "FMCW radars for snow research". In: *Cold Regions Science and Technology* 52.2, pp. 118–131.

Marzeion, Ben, Cogley, J Graham, Richter, Kristin, and Parkes, David (2014). "Glaciers. Attribution of global glacier mass loss to anthropogenic and natural causes." In: *Science* 345.6199, pp. 919–21.

Matzl, Margret and Schneebeli, Martin (2006). "Measuring specific surface area of snow by near-infrared photography". In: *Journal of Glaciology* 52.179, pp. 558–564.

Mätzler, C (1994). "Passive microwave signatures of landscapes in winter". In: *Meteorology and Atmospheric Physics* 260, pp. 241–260.

Matzler, C and Wiesmann, A (1999). "Extension of the microwave emission model of layered snowpacks to coarse-grained snow". In: *Remote sensing of environment* 325.April, pp. 317–325.

Mätzler, Christian (1996). "Microwave Permittivity of Dry Snow". In: *IEEE Transactions on Geoscience and Remote Sensing* 34.2, pp. 573–581.

Minsasny, B. and McBratney, A. B. (2005). "The Matérn function as general model for soil variograms". In: *Geoderma* 3-4, pp. 192–207.

Montpetit, B, Royer, Alain, Roy, Alexandre, Langlois, Alexandre, and Derksen, Chris (2012). "Snow Microwave Emission Modeling of Ice Lenses Within a Snowpack Using the Microwave Emission Model for Layered Snowpacks". In: *IEEE Transactions on Geoscience and Remote Sensing* 51.9, pp. 4705 –4717.

Moritz, Richard E, Bitz, Cecilia M, and Steig, Eric J (2002). "Dynamics of recent climate change in the Arctic." In: *Science* 297.5586, pp. 1497–502.

Nghiem, S. V., Hall, D. K., Mote, T. L., Tedesco, M., Albert, M R, Keegan, K., Shuman, C. A., DiGirolamo, N. E., and Neumann, G. (2012). "The extreme melt across the Greenland ice sheet in 2012". In: *Geophysical Research Letters* 39.20.

Painter, Thomas H., Rittger, Karl, McKenzie, Ceretha, Slaughter, Peter, Davis, Robert E., and Dozier, Jeff (2009). "Retrieval of subpixel snow covered area, grain size, and albedo from MODIS". In: *Remote Sensing of Environment* 113.4, pp. 868–879.

Pfeffer, W T and Humphrey, N F (1996). "Determination of timing and location of water movement and ice-layer formation by temperature measurements in sub-freezing snow". In: *Journal of Glaciology* 42.141, pp. 292–304.

Picard, Ghislain, Brucker, Ludovic, Roy, Alexandre, Dupont, Florent, Fily, M, Royer, Alain, and Harlow, C (2013). "Simulation of the microwave emission of multi-layered snowpacks using the Dense Media Radiative transfer theory: the DMRT-ML model". In: *Geoscientific Model Development* 6.4, pp. 1061–1078.

Pielmeier, Christine and Schneebeli, Martin (2003). "Developments in the stratigraphy of snow". In: *Surveys in Geophysics* 24.5-6, pp. 389–416.

Pithan, Felix and Mauritsen, Thorsten (2014). "Arctic amplification dominated by temperature feedbacks in contemporary climate models". In: *Nature Geoscience* 7.3, pp. 181–184.

Pomeroy, J. W. and Gray, D. M. (1995). *Snow Cover Accumulation, Relocation and Management*. 7th ed. Saskatoon: Envirnoment Canada - Inland Waters Directorate.

Pulliainen, Jouni and Hallikainen, Martti (2001). "Retrieval of regional snow water equivalent from space-borne passive microwave observations". In: *Remote Sensing of Environment* 75, pp. 76–85.

Putkonen, J and Roe, G (2003). "Rain-on-snow events impact soil temperatures and affect ungulate survival". In: *Geophysical Research Letters* 30.4, p. 37.

Rees, Andrew, Lemmetyinen, Juha, Derksen, Chris, Pulliainen, Jouni, and English, M (2010). "Observed and modelled effects of ice lens formation on passive microwave brightness temperatures over snow covered tundra". In: *Remote Sensing of Environment* 114.1, pp. 116–126.

Rees, Andrew, English, M, Derksen, Chris, Toose, Peter, and Silis, Arvids (2013). "Observations of late winter Canadian tundra snow cover properties". In: *Hydrological Processes.*

Rees, W. Gareth (2006). *Remote Sensing of Snow and Ice.* 1st. Vol. 100. Martinec 1977. Taylor & Francis Group, LLC, pp. 7 –38.

Reichle, Rolf H. (2008). "Data assimilation methods in the Earth sciences". In: *Advances in Water Resources* 31, pp. 1411–1418.

Robinson, David A., Dewey, Kenneth F., and Heim, Richard R. (1993). "Global Snow Cover Monitoring: An Update". In: *Bulletin of the American Meteorological Society* 74.9, pp. 1689–1696.

Rott, H and Mätzler, C (1987). "Possibilities and limits of synthetic aperture radar for snow and glacier surveying". In: *Annals of Glaciology*, pp. 195–199.

Roy, Alexandre, Picard, Ghislain, Royer, Alain, Montpetit, Benoit, Dupont, Florent, Langlois, Alexandre, Derksen, Chris, and Champollion, Nicolas (2013). "Brightness temperature simulations of the Canadian seasonal snowpack driven

by measurements of the snow specific surface area". In: *IEEE Transactions on Geoscience and Remote Sensing* 51.9, pp. 4692 –4704.

Rutter, N, Sandells, M J, Derksen, Chris, Toose, Peter, Royer, Alain, Montpetit, B, Langlois, Alexandre, Lemmetyinen, Juha, and Pulliainen, Jouni (2014). "Snow stratigraphic heterogeneity within ground, based passive microwave radiometer footprints: Implications for emission modeling". In: *Journal of Geophysical Research: Earth Surface*, pp. 550–565.

Screen, James A and Simmonds, Ian (2010). "The central role of diminishing sea ice in recent Arctic temperature amplification." In: *Nature* 464.7293, pp. 1334–7.

Serreze, M.C., Holland, Mm, and Stroeve, J.C. (2007). "Perspectives on the Arctic's shrinking sea-ice cover". In: *Science* 315.2007, pp. 1533–1536.

Solheim, Fredrick Stuart (1993). "Use of Pointed Water Vapor Radiometer Observations to Improve Vertical GPS Surveying Accuracy." PhD thesis. University of Boulder at Colorado.

Staelin, D H, Rosenkranz, P W, Barath, F T, Johnston, E J, and Waters, J W (1977). "Microwave spectroscopic imagery of the Earth." In: *Science* 197.4307, pp. 991–3.

Stewart, Iris T. (2009). "Changes in snowpack and snowmelt runoff for key mountain regions". In: *Hydrological Processes* 23.1, pp. 78–94.

Stogryn, Alex (1986). "A Study of the Microwave Brightness Temperature of Snow from the Point of View of Strong Fluctuation Theory". In: *IEEE Transactions on Geoscience and Remote Sensing* GE-24.2, pp. 220–231.

Sturm, Matthew and Benson, Carl (2004). "Scales of spatial heterogeneity for perennial and seasonal snow layers". In: *Annals of Glaciology* 38, pp. 253–260.

Sturm, Matthew, Grenfell, Thomas C., and Perovich, Donald K. (1993). "Passive microwave measurements of tundra and taiga snow covers in Alaska, U.S.A." en. In: *Annals of Glaciology* 17, pp. 125–130.

Sturm, Matthew, Holmgren, Jon, and Liston, Glen E (1995). "A Seasonal Snow Cover Classification-System for Local to Global Applications". In: *Journal of Climate* 8.5, pp. 1261–1283.

Sturm, Matthew, Douglas, Tom, Racine, Charles, and Liston, Glen E. (2005). *Changing snow and shrub conditions affect albedo with global implications.*

Tait, A B (1998). "Estimation of snow water equivalent using passive microwave radiation data". In: *Remote Sensing of Environment* 64.3, pp. 286–291.

Takala, Matias, Luojus, Kari, Pulliainen, Jouni, Derksen, Chris, Lemmetyinen, Juha, Kärnä, J-P, Koskinen, J T, and Bojkov, Bojan (2011). "Estimating northern hemisphere snow water equivalent for climate research through assimilation of space-borne radiometer data and ground-based measurements". In: *Remote Sensing of Environment* 115.12, pp. 3517–3529.

Tape, Kenneth D, Sturm, Matthew, and Racine, Charles H (2006). "The evidence for shrub expansion in Northern Alaska and the Pan-Arctic". In: *Global Change Biology* 12, pp. 686–702.

Tape, Kenneth D, Rutter, Nick, and Marshall, Hans-Peter (2010). "Recording microscale variations in snowpack layering using near-infrared photography". In: *Journal of Glaciology* 56.195, pp. 75–80.

Tedesco, Marco and Kim, Edward J. (2006). "Intercomparison of Electromagnetic Models for Passive Microwave Remote Sensing of Snow". In: *IEEE Transactions on Geoscience and Remote Sensing* 44.10, pp. 2654–2666.

Troy, Tara J., Sheffield, Justin, and Wood, Eric F. (2012). "The role of winter precipitation and temperature on northern Eurasian streamflow trends". In: *Journal of Geophysical Research* 117.D5, p. D05131.

Tse, K K, Tsang, L, Chan, C H, Ding, K H, and Leung, K W (2007). "Multiple scattering of waves by dense random distributions of sticky particles for applications in microwave scattering by terrestrial snow". In: *Radio Science* 42.5.

Turner, J and Overland, J (2009). "Contrasting climate change in the two polar regions". In: *Polar Research* 28, pp. 146–164.

Ulaby, F T, Moore, R K, and Fung, A K (1981). *Microwave remote sensing: Active and passive. Volume 1 - Microwave remote sensing fundamentals and radiometry.* Vol. 1. Longman Higher Education, p. 456.

Ulaby, F T, Moore, R K, and Fung, A K (1986). *Microwave remote sensing: Active and passive. Volume 3 - From theory to applications.* Vol. 3, p. 1120.

Vander Jagt, Benjamin J., Durand, Michael T., Margulis, Steven A, Kim, Edward J, and Molotch, Noah P. (2013). "The effect of spatial variability on the sensitivity of passive microwave measurements to snow water equivalent". In: *Remote Sensing of Environment* 136, pp. 163–179.

Wackernagel, H. (1995). *Multivariate Geostatistics*. Springer.

Walker, Anne E. and Silis, Arvids (2002). "Snow-cover variations over the Mackenzie River basin, Canada, derived from SSM/I passive-microwave satellite data". In: *Annals of Glaciology* 34.1, pp. 8–14.

Wiesmann, A and Mätzler, C (1999). "Microwave emission model of layered snowpacks". In: *Remote Sensing of Environment* 70.3, pp. 307–316.

Woo, M. (1997). *A Guide for Ground Based Measurement of the Arctic Snow Cover*. Tech. rep. Queen's Printer for Canada: Ottawa: Meteorological Service of Canada, Climate Research Branch.

Zhang, L, Shi, Jiancheng, Zhang, Zhongjun, and Zhao, Kaiguang (2003). "The estimation of dielectric constant of frozen soil-water mixture at microwave bands". In: *Geoscience and Remote Sensing Symposium, 2003. IGARSS '03. Proceedings*, pp. 2903–2905.

Zhang, Tingjun (2005). "Influence of the seasonal snow cover on the ground thermal regime: an overview". In: *Reviews of Geophysics* 43.RG4002.